Targeting Low Vapour Pressure Compounds In Gas-phase Electron Diffraction

Julien T. Schirlin

A thesis presented for the degree of
Doctor of Philosophy
In the College of Science and Engineering
University of Edinburgh, 2004

Acknowledgements

I would like to thank my supervisor David, for being there when stuck, giving great guidance and especially for providing a team of excellent postdoctoral fellows, a team always ready to go the extra mile. I would like to thank Heather for introducing me to the gas-phase electron diffraction apparatus' most intimate parts, and the considerable help during experiment time. Without her and now Kostya, I would never have been able to collect so much experimental data.

Thanks go to Sarah for kindly correcting my English and general layout before every poster, oral presentation and this thesis. Thanks go to Kostya for the multiple helpful conversations through the years. I would like to thank Andy for providing incredible programming support and for giving birth to the ed@ed program.

Thanks go to Martin, Thomas, Derek, Maria, Iain, Lorna and all the post docs for providing so many laughs at my expense and a fun environment. You all made my stay in Scotland so much smoother.

Thanks go as well to the technical staff, Mr. Stuart Johnstone, Mr. Stuart Mains and Donald Palin, who listened to my crazy ideas and allowed some of the designs to see daylight.

I am grateful for all the support received from my friends in France, especially from Béné, during these three years.

I'd finally like to thank my parents and my brother for giving me great support along the years.

Abstract

A limiting factor in using gas electron diffraction (GED) for structure determination, the volatility of samples, is addressed in Chapters 2 & 3, by the adoption of a new nozzle design and by the development of a heated sample reservoir. The use of a slit nozzle has extended application of GED to compounds with vapour pressures or vaporisation rates that were previously inadequate. The slit shape of the new nozzle permits operation at a lower vapour pressure by increasing the diffraction area. A heated reservoir has been successfully developed for compounds with equilibrium vapour pressures adequate for the GED technology, but with vaporisation rates incompatible with maintaining the necessary vapour pressure for the duration of the experiment.

In addition to the work on the development of improved sampling techniques, investigations on the structures of carbaboranes and sulfur-containing heterocycles are reported. GED investigation of 2-chloro- and 2-bromothiophene and *ab initio* calculations revealed no significant deformation of the ring from C_{2v} symmetry. Further halogen substitution, investigated via *ab initio* calculations, gave similar results. Analysis of GED data collected for 2,5-dichlorothiophene and 3,4-dichloro-1,2,5-thiadiazole are reported (Chapter 5), together with an extensive series of *ab initio* calculations on these molecules and 2,5-difluoro- and 3,4-dichlorothiophene. These have allowed accurate gas-phase molecular structures to be assigned to 2,5-dichlorothiophene and 3,4-dichloro-1,2,5-thidiazole. The structures are compared to those of their parent compounds to assess the effects of halogen substitutions.

Structure determination by both *ab initio* calculations and electron diffraction has been carried out for two mono-substituted 1,12-carbaboranes, 1-ethynyl- and 1-trimethylsilylethynyl-*para*-carbaboranes. Investigation of the effects of substitutions

at the *para* positions via *ab initio* calculations has revealed that the cages are susceptible to change only if electron-donating groups are attached to one or both poles of the cage.

Abbreviations and acronyms

B3	electron exchange functional, Becke 3 parameters
B3LYP	B3 electron exchange functional and the LYP correlation functional
CI	Configuration Interaction
CISD	Configuration Interaction Single and Double excitations
CV	conventional nozzle
DFT	Density Functional Theory
DYNAMITE	DYNAMic Interaction of Theory and Experiment
e.s.d.	estimated standard deviation
GED	Gas-Phase Electron Diffraction
GGA	Generalized Gradient Approximation
GTO	Gaussian Type Orbitals
HF	Hartree-Fock
LCAO	Linear Combination of Atomic Orbitals
LDSA	Local Spin Density Approximation
LYP	correlation functional developed by Lee, Yang and Parr
MBPT	Many Body Perturbation Theory
MIC	Molecular Intensity Curve
MO	Molecular Orbital
MP2	Second order Møller-Plesset
MW	Microwave spectroscopy
R_D	goodness of fit diagonal
RDC	Radial Distribution Curve
r_e	equilibrium distance between the positions of atomic nuclei corresponding to the minimum of the potential energy
R_G	goodness of fit general (taking into account correlations)
r_{h1}	distance between average nuclear positions in the thermal equilibrium at temperature T (curvilinear correction)
RMS	Root Mean Square
S	"true" slit nozzle

SARACEN	Structure Analysis Restrained by *Ab initio* Calculation for Electron diffractioN
SE	simulated slit nozzle even type flow
SG	simulated slit nozzle gaussian type flow
STO	Slater Type Orbitals

Contents

CONTENT OF THE ATTACHED CD

Chapter 1

Introduction

1.1 General introduction

Nearly three-quarters of a century ago, Gas-Phase Electron Diffraction (GED) began through the pioneering work of Mark and Wierl,[1] giving the first reported gas-phase structure of carbon tetrachloride in 1930. Since then, GED has remained the most valuable technique for the collection of structural information in the gas phase. The second technique available for accurate experimental structure determination of gaseous molecules, rotational spectroscopy, is restricted to small molecules. The numerous isotopic substitutions required to extract any structural information from rotational constants determined via microwave spectroscopy for some of the molecules in the following work make it impractical at best. Even though isotopic substitution is not needed for electron diffraction studies, large structures are a challenge. Through the years our group has developed new techniques such as SARACEN[2] and DYNAMITE[3] to tackle bulky molecules. They use *ab initio* and molecular mechanics methods respectively, which enable the elucidation of crucial structural information from the experimental data. GED is effectively the sole structural technique in the gas phase allowing the theoretician to compare his/her results with experimentally determined structures of rather large molecules.

1.2 Background to gas-phase electron diffraction

1.2.1 Historical Fact

In order to understand the preponderant role of GED we shall first seek its origins. Before any technical instrument could be designed a good basis of theory had to be established. Louis De Broglie, having a bachelor's degree in the history of the Middle Ages and ancient writings, reoriented himself after listening to a memorable lecture given by the famous philosopher and mathematician Henri Poincaré. Magnetised by the concept of classical mechanics initiated by Planck's concepts on the quantum of energy and in scientific method, he obtained a new degree in mathematics and started to work side by side with his brother, an expert in X-ray diffraction at the time. He was thus exposed to the relationships between photons,

electrons, and particles, and soon published an article about black-body radiation,[4] in which he stated that the "hypothesis of quanta of light [was] adopted". In this article the photons were treated as particles, "atoms of light" with mass $\frac{h\nu}{c^2}$ and momentum $\frac{h\nu}{c}$. It is at that point that he decided to define a theory that would unify the wave and particle descriptions of radiation. He took into account Thomas Young's discovery of interference phenomena and followed the admirable work of Augustin Fresnel, which ruled out the hypothesis of a granular structure of light to the profit of wave theory. In the middle of 1923, de Broglie generalised wave-particle duality to include material corpuscles, thinking of electrons in particular. Contrary to common knowledge, his discovery took place in 1923 and was published in three short articles that same year in *Comptes Rendus*[5] and one short note in *Nature*.[6] The famous formula which correlated a particle, in our case electrons, to a wave was first published in his thesis[7] as follows:

$$\lambda = \frac{h}{mv} \qquad \text{EQ 1.1}$$

where wavelength λ is related to Planck's constant h, v being the speed of the electron and m the mass of the electron.

It might have been because his brother Maurice reminded him of "the educational value of experimental sciences" and that "the theoretical constructions of science have no value unless they are supported by facts", that he suggested in 1923:

"A beam of electrons passing through a very small opening could present diffraction phenomena. This is perhaps the direction in which one may search for an experimental confirmation of our ideas."[5]

A few years later, in 1927, Germer and Davidson[8] showed that the phenomenon of electron diffraction by crystals actually exists and obeys exactly and quantitatively the laws of wave mechanics. These results were confirmed by Thomson,[9] in Aberdeen, who also recorded, but with fast electrons, that interference effects give

rise to maxima and minima in the intensities of the reflected electrons for aluminium foil.

The first gas-phase X-ray diffraction, carried out by Debye[10] in 1929, triggered the first gas-phase electron diffraction in less than a year by Mark and Wierl.[1] The advantage of this new technique was the enormous saving of time involved in obtaining data, only a few seconds are required for GED compared to 10 hours for X-ray.

At first the plates were read by an experienced eye using a visual method,[11] which consisted of measuring the diameters of rings of maximum and minimum intensity and comparing them with the corresponding values calculated from a model. A description of a typical model is given in section 1.2.5. The best fit by trial and error gave the geometrical structure. Soon applied with Fourier transform to give the radial distribution curve, it became the most powerful technique[12] for the determination of molecular structure in the gas phase. This technique was one of the bases of the theory of chemical bonding, along with molecular spectroscopy and X-ray crystallography.[13] In order to compensate for the atomic background, a rotating sector was introduced, in 1933, which would screen scattered electrons[14] and was applied by Finbak[15] and P.P. Debye.[16] This made quantitative elucidation of the intensity distribution possible. From 1950 onwards, it was used in combination with photometers which measured the optical density distribution of the pattern on the photographic plate. And nowadays, with the help of greater computer capability, *ab initio* calculations and least-squares fits generate more accurate structures than ever before.

1.2.2 The apparatus

The GED method of structure-determination is based on the phenomenon that a beam of fast electrons is scattered by the electric field gradient. In other words the molecular structure in GED is given by the position of the nuclei.

The GED instrument shown in **Figure 1.1** is equipped with all the typical features, an electron gun, a focusing system, a sample injection system and a detector. At

Edinburgh a triode generator is used to generate a monochromatic beam of electrons by boiling them off of a heated cathode (hot tungsten wire), a process known as thermionic emission. The electrons leave the cathode and are accelerated by the anode at a voltage of 40 kV, allowing a constant wavelength of about 0.06 Å. Each electron in the beam has a kinetic energy equal to the accelerating electric potential (V) times the electron charge.

When $eV << mc^2$

$$\mathrm{KE} = \frac{1}{2} m_e v^2 = eV \qquad \text{EQ 1.2}$$

$$\text{since } \lambda = \frac{h}{m_e v}$$

$$\text{therefore } \lambda = \frac{h}{\sqrt{2eVm_e}} \qquad \text{EQ 1.3}$$

In order to control the anode current, the cathode is surrounded by a metal shield called the cathode "can", or Wehnelt cylinder. A bias voltage holds the cathode can negative with respect to the cathode, thus moderating the current and collimating the beam. The beam is further shaped and focused by a set of apertures and electromagnetic lenses before entering the diffraction chamber where it interacts with the gaseous molecules streaming from a nozzle, with a backing pressure of about 10 torr. The molecules, at temperatures up to 230 °C in our apparatus, at least 1500°C elsewhere, are introduced perpendicular to the electron beam and condensed on the cold trap after diffraction if not pumped out of the diffraction chamber. The diffraction patterns are recorded on photographic plates or observed on a fluorescent screen with a CCD camera. The total electron scattering intensity decreases to the fourth power with respect to the scattering, so a rotating sector with opening compensating for the steeply falling background is placed in the path of the scattered electrons. It avoids saturation at the centre of the photographic plates or films, by decreasing the relative exposure time for smaller scattering angles, and allowing more electrons to hit the plates at their edges rather than at their centre.

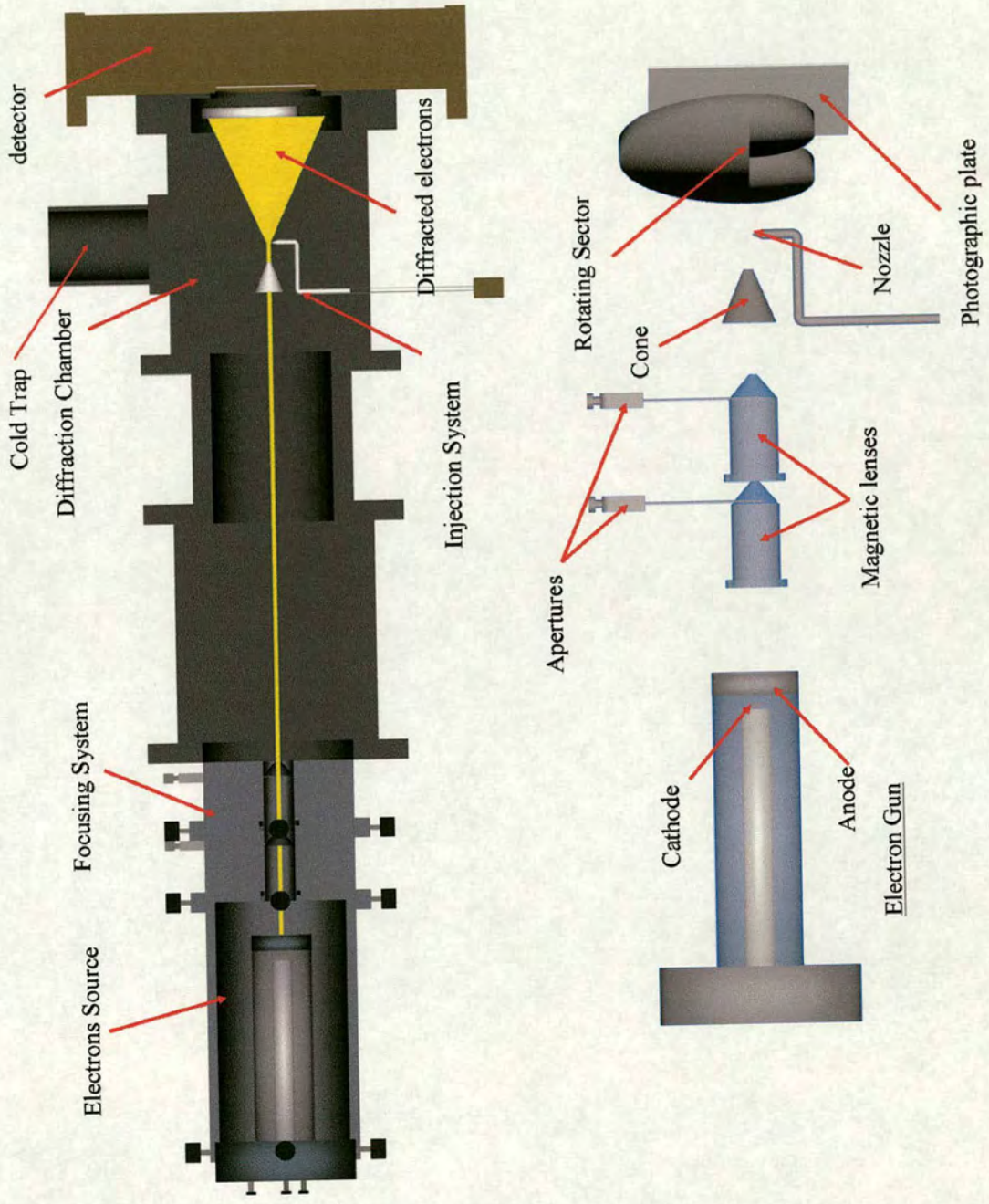

Figure 1.1: Edinburgh gas-phase electron diffraction set up

1.2.3 Theory of gas-phase electron diffraction

Because of their wave/particle duality, when the electrons are directed towards a molecule, every pair of atoms within the molecules acts like a pair of slits as in Young's experiment shown in **Figure 1.2**. An incident plane wave light source passing through two slits causes constructive and destructive interferences that will be recorded by a detector. As for light, during an experiment the electrons show constructive and destructive interferences. Since the gaseous molecules are randomly oriented in space the maxima and minima are observed as concentric rings (**Figure 1.3**).

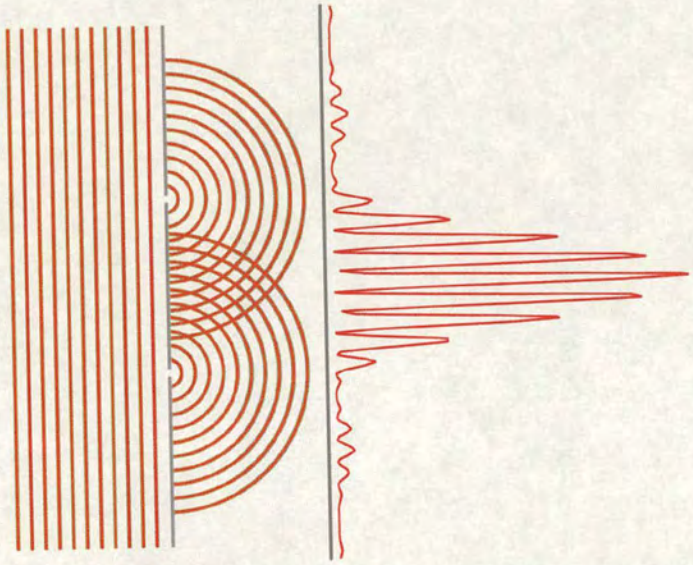

Figure 1.2: Young double slit experiment

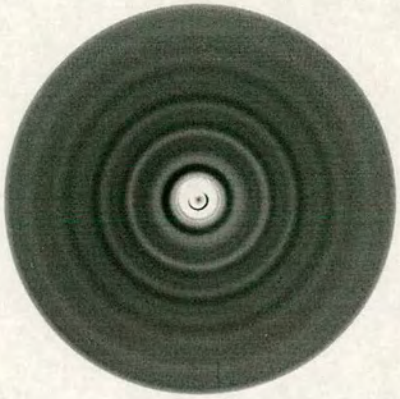

Figure 1.3: Typical diffraction pattern

From the collected diffraction pattern the scattering intensities are extracted as a function of scattering angle. For convenience, during data reduction and structure refinement a universal s variable is used. It is related to the scattering angle (θ) and proportional to the electron wavelength (λ) as follows:

$$s = \frac{4\pi}{\lambda} \sin\left(\frac{\theta}{2}\right) \quad \text{EQ 1.4}$$

From the total scattering intensity, $I_{tot}(s)$, which has previously been corrected for the flatness of the plate, blackness and the presence of the rotating sector, the atomic contribution, $I_{atom}(s)$, is subtracted along with the extraneous scattering, $I_{bgd}(s)$, giving the molecular intensity, $I_{mol}(s)$. (EQ 1.5). This step is referred to as data reduction.

$$I_{mol}(s) = I_{tot}(s) - I_{atom}(s) - I_{bgd}(s) \quad \text{EQ 1.5}$$

I_{atom} corresponds to the sum of all the atomic elastic scattering:

$$I_{\text{atom}}(s) = \sum_{i=1}^{N} |f_i(s)|^2 \qquad \text{EQ 1.6}$$

where N is the number of atoms in the molecule and $f_i(s)$ the scattering factor amplitude of the i^{th} atom such that:

$$f_i(s) = \frac{2\,(Z_i - F_i(s))}{a_0\, s^2} \qquad \text{EQ 1.7}$$

where a_0 is the Bohr radius, Z_i and $F_i(s)$ are the atomic numbers and the atomic scattering factors respectively. Glauber and Schomaker showed that when there is a mixture of heavy and light atoms a phase shift is observed.[18] This require the use of complex atomic scattering amplitudes (EQ 1.8) to compensate for the failure in the previous equation.

$$f_i(s) = |f_i(s)| \exp[i\eta_i(s)] \qquad \text{EQ 1.8}$$

$|f_i(s)|$ is the absolute value of the scattering amplitude and η_i is its phase for the i^{th} atoms.

Because in a GED experiment gaseous molecules are observed, I_{mol} has to include a term describing atomic motions. u^2_{ij} is the root-mean-square amplitude of vibration, and is defined as the root of the averaged squared difference between the equilibrium distance, $r_{e,ij}$ and the actual distance, $r_{a,ij}$ between atoms at any given time i and j.

$$u_{ij}^2 = \langle (r_{e,ij} - r_{a,ij})^2 \rangle \qquad \text{EQ 1.9}$$

The molecular scattering intensity therefore has the following form for $i \neq j$:

$$I_{\mathrm{mol}}(s) = \sum_{i=1}^{N} \sum_{j=1}^{N} \cos[\eta_i(s) - \eta_i(s)] \exp\left(-\frac{1}{2} u_{ij}^2 s^2\right) \frac{\sin[s(r_{ij} - k_{ij}s^2)]}{s r_{ij}}$$

EQ 1.10

r_{ij} is the effective average internuclear distance between a pair of atoms; k is a anharmonicity constant, which is related to the Morse anharmonic potential. Along with the RMS amplitudes of vibration these are the three terms that are extracted from a GED experiment.

$I_{\mathrm{bgd}}(s)$ comes from secondary diffracted electrons, aperture scattering, as well as inelastic contributions and the experimental environment, and is removed using a spline function. This function is defined so that any oscillating components correspond to a frequency smaller than that for the shortest distances within the molecule.

A radial distribution curve is used for a better illustration of the physical meaning of the $I_{\mathrm{mol}(s)}$ and is the result of a Fourier transform of the molecular scattering intensities. The center of each Gaussian peak on that plot marks a bonded or non-bonded distance, while the half height-width of the peak is proportional to the RMS amplitude of vibration of a pair of atoms. The relative peak areas in the radial distribution curve are given by:

$$\mathrm{Area} \propto \frac{n_{ij} Z_i Z_j}{r_{ij}} \quad \text{EQ 1.11}$$

where Z_i and Z_j are the atomic numbers of atoms i and j and n_{ij} is the number of times the same distance between two atoms, r_{ij}, occurs.

All these steps can be summarized by the following diagram:

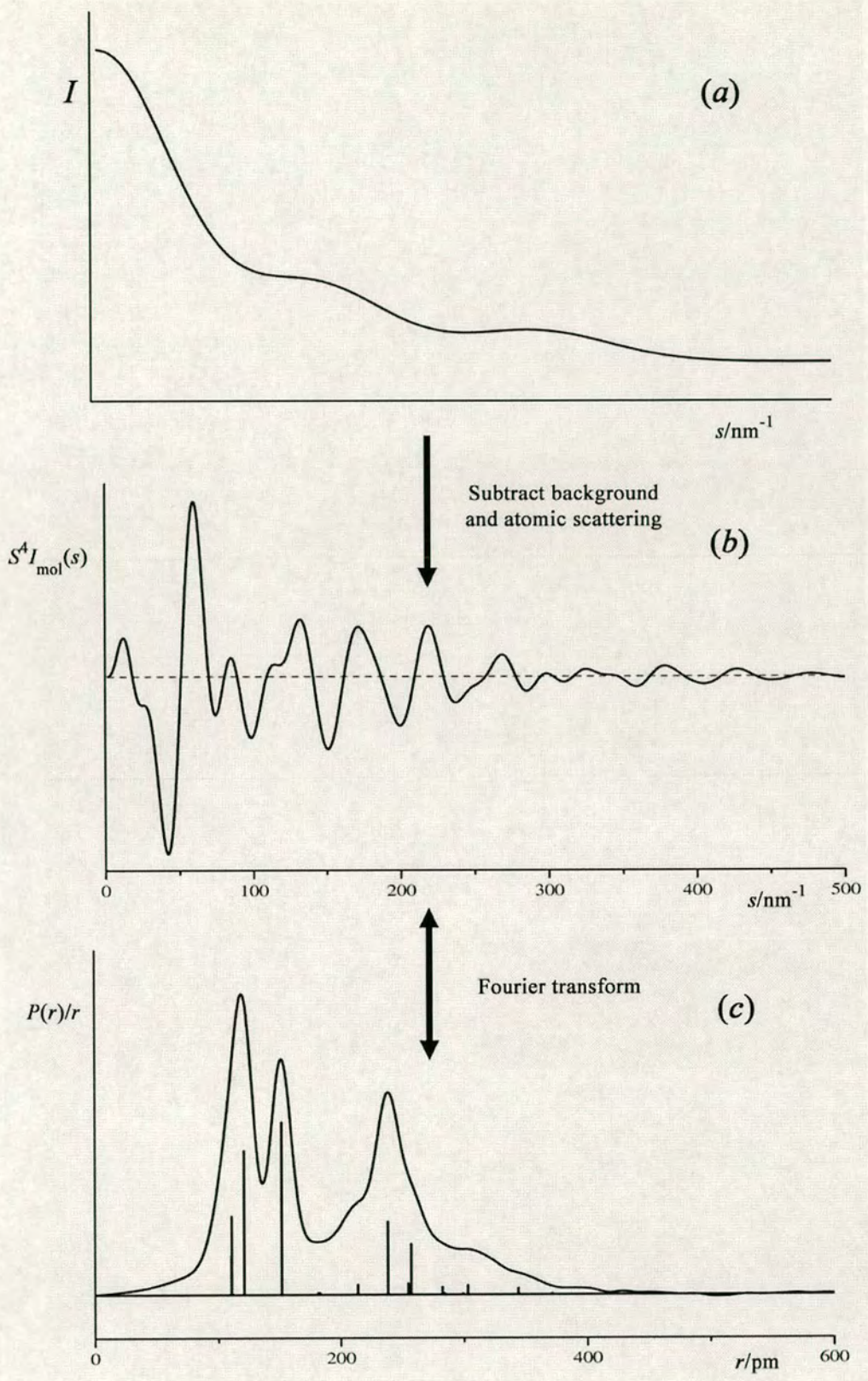

Figure 1.4: From raw data to radial distribution curve (a) Total intensity scattering Curve, (b) Molecular intensity scattering Curve (c) Radial Distribution Curve

1.2.4 Advantages and disadvantages of gas-phase electron diffraction

Being a gas-phase technique, electron diffraction can determine structure without any intermolecular interactions, allowing for comparison with the results of theoretical calculations. Thus the structure found in the vapour phase can be considered as determined solely by intramolecular forces. The determination of free structures pushes the establishment of bonding theories and the development of theoretical chemistry. In a more experimental sense it helps towards understanding the structure and reactivity correlation and can monitor vapour-phase reactions. This technique can provide information for comprehension of conformational properties of biologically active substances, as well as for solution of structural problems concerning semi-conductors and polymeric materials through understanding of a simplified model.

Gas-phase electron diffraction (GED) measures internuclear distances, whereas in X-ray diffraction the centres of electron density are measured. In GED, electrons are primarily scattered by the electric field gradient, ie. effectively by the nuclei, whereas X-rays are scattered by the electrons, which surround the atoms of the molecules. As a consequence, a higher level of accuracy is obtained for GED (±0.001 Å) as compared to X-ray crystallography (±0.003 Å). This also makes the exact positioning of hydrogen atom nuclei possible, whereas for X-ray diffraction this is not feasible. The strong interaction between the electron beam and the irradiated system gives more intense scattering and permits a shortening of the exposure times by a factor of between 1000 to 10000 in comparison to X-ray diffraction.

As stated previously, the area under each peak in the radial distribution is directly proportional to the atomic numbers of the atoms contributing to that peak in a given molecule. Therefore distinguishing two distances with atoms of similar atomic numbers is problematic, as can be illustrated with perchloryl fluoride in **Figure 1.5**. In this case the O···O and F···O distances overlap and as a consequence it is difficult to assign the true distances under the non-bonded peak. To solve this problem, the Structure Analysis Restrained by Ab initio calculation (SARACEN[1]) method was

developed by the Edinburgh group. It allows flexible restraints derived from *ab initio* calculations to be applied, allowing two distances lying under the same peak to be refined to reasonable values. If no restraints were adopted it is more likely that the refinement would result in unrealistic values for O···O and F···O. If parameters were constrained at *ab initio* values, it would mean that the calculated parameters were assumed to be correct, which would lead to unrealistically low estimated standard deviations for correlated parameters and may ultimately lead to a false structure .

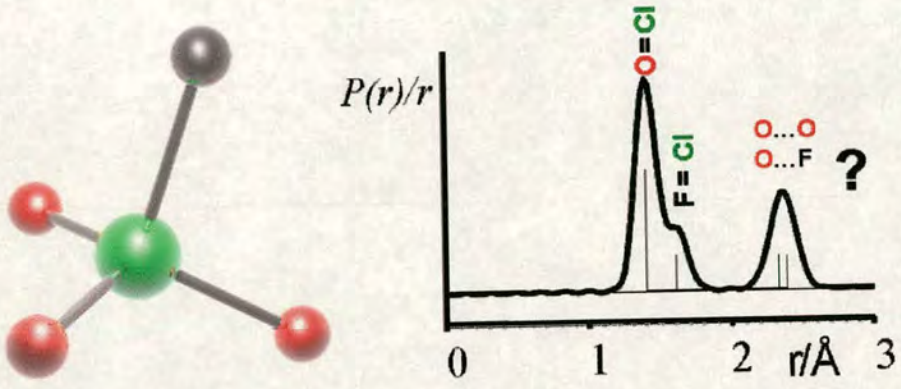

Figure 1.5: Structure and radial distribution curve for perchloro-fluoride[19]

Similarly, the possibility of locating the positions of light atoms when there are similar distances involving much heavier atoms is limited. Once again a new technique developed by the group was recently developed to target bulky molecules. In these molecules individual light atoms have little to do with the entire picture but together they do influence the overall scattering. The DYNAMic Interaction of Theory and Experiment (DYNAMITE[3]) method is applied during the standard refinement method. During every cycle of refinement the heavy atom positions are allowed to refine freely and then the positions of the light atoms are determined by molecular mechanics.

In the early fifties, some spectroscopists thought that the structures determined by GED were systematically biased and inaccurate. Yonez Morino decided, while performing the refinement, to take into account that a molecule, especially in the gas

phase, is a dynamic system, vibrating about its equilibrium structure. In GED we measure the means of interatomic distances in vibrational states in thermal equilibrium. In a floppy molecule such as the triatomic molecule (**Figure 1.6**), each electron sees only one instantaneous configuration. As illustrated, molecules spend most of their time in a bent form, and so the average distance between non-bonded atoms appears shorter than it is in reality. Shrinkage corrections are calculated and extracted from the theoretical force field by a program developed by Sipachev.[20] There are a number of types of shrinkage corrections. Refinement using the first approximation (rectilinear correction), gives distances referred to as r_{h0}. In this work, only r_{h1} structures are determined, using the second order approximation (curvilinear correction), as shown in **Figure 1.6**.

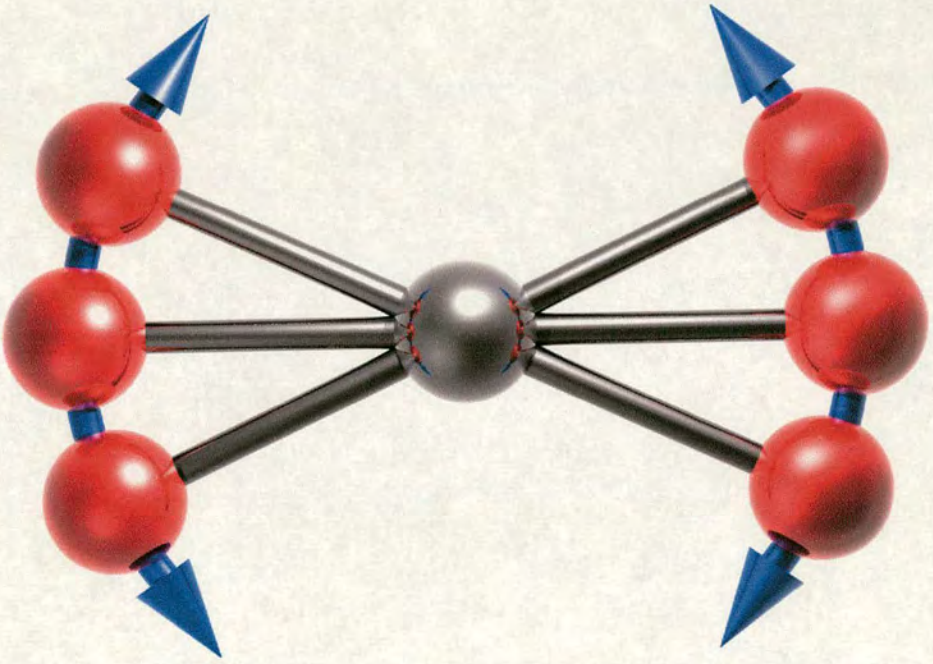

Figure 1.6: Vibration Schematic of Triatomic Molecule.

1.2.5 Refinement procedure

The diffraction patterns recorded on photographic plates or films are first converted to mathematical values. This step was carried out at the Institute of Astronomy in Cambridge,[17] where the plates were scanned by a PDS densitometer. At this stage home-designed software assigns each recorded intensity to its scattering angle, determined as a function of the nozzle-to-camera distance and of the centre of the symmetric pattern. All of these steps are now carried out by our group at the University of Edinburgh.

For each compound, scattering intensities are collected at two different camera/nozzle distances, long and short or middle. Benzene intensities are recorded for each run. The average C-C bond length (along with the C-H bond length) from the aromatic ring serves as a reference and allows the true distance camera/nozzle as well as the wavelength of electrons to be deduced.[21]

Before refinement, a mathematical model of the molecule under investigation is built with sets of parameters, which correspond usually to bonded distances and related bond angles. This starting geometry is in general mapped on an *ab-initio* calculated structure. The RMS amplitudes of vibration are also extracted from calculations. Recently a new program with a visual interface, ed@ed,[22] based on ed96[23] previously released by the group, performs the data reduction and structure refinement. Once data reduction has been carried out, parameters defined in the mathematical model as well as the RMS amplitudes of vibration of the molecules are adjusted until the best agreement between the theoretical model and experimental scattering intensities is obtained. This is carried out by a non-linear least-squares analysis procedure. A residual factor, R_G, gives the goodness of fit between the model and the experimental result. This value, along with the estimated standard deviation (e.s.d.) calculated for each parameter in the mathematical model, determines the level of confidence in the experimental structure. The smaller the e.s.ds and the residual factor are, the better it is. Graphically, curves showing the difference between the model and experimental data, below the radial distribution and molecular intensity curves, facilitate the

determination of the source of the errors. A crucial advantage of this new code is that all changes at every step of refinement can be followed on the same screen.

Data from various sources (coupling constants from NMR spectroscopy, rotational constants from microwave spectroscopy) can be used to aid the refinement by providing the bases for flexible restraints.

1.3 *Ab initio* calculations

1.3.1 Introduction

In order to understand the methods used in this project it is imperative to explain the meaning of *ab initio*. *Ab initio* is Latin for "from the beginning", which implies that only first principles are used, requiring only physical constants. *Ab initio* is viewed as the opposite of empirical calculations, which rely entirely on experimental parameters. However the method can rely upon experimental calibration to some degree! Once solved, the Schrödinger equation leads to a predicted geometry as well as physical properties. Thus from this strictly quantum theoretical method, reaction mechanisms can be predicted as well as vibrations. With the electronic analysis a better understanding of bonding properties can be obtained. Many spectroscopic properties can be calculated quantitatively and qualitatively by quantum mechanics calculations.

It all started with the work by Max Planck, at the beginning of the 20^{th} century, postulating that the energy of electromagnetic radiation comes in discrete packets, quanta, and cannot be varied arbitrarily, so that oscillators are excited only if they acquire an energy of at least $h\nu$. This idea along with the wave/particle duality of the electrons as seen previously triggered a new era of quantum mechanics. In 1926, Erwin Schrödinger pioneered the wave mechanics interpretations of this new discipline by publishing the now ubiquitous Schrödinger equation (EQ 1.12), where the system behaviour is described in terms of the time-dependent wave function (Ψ).

$$H\Psi = i\hbar\frac{\partial\Psi}{\partial t} \quad \text{EQ 1.12}$$

In chemistry, the time-independent Schrödinger equation (EQ 1.13) is often used.

$$E\Psi = H\Psi \quad \text{EQ 1.13}$$

where: E= the total molecular energy

Ψ = the total wave function

H = the Hamiltonian operator

1.3.2 Simplification of the Hamiltonian operator

From the Schrödinger equation (EQ 1.13) the Hamiltonian operator contains the kinetic energy (T) as well as the potential energy (V), which includes the dynamics of all electrons and nuclei in a molecule. Therefore the Hamiltonian contains the following terms:

$$H = T_e + T_n + V_{ne} + V_{ee} + V_{nn} \quad \text{EQ 1.14}$$

where: T_e is the kinetic energy of the electron

T_n is the kinetic energy of nuclei

V_{ne} is the potential energy of the coulomb attraction between electrons and nuclei

V_{ee} is the potential energy of electronic repulsion

V_{nn} is the potential energy of nuclear repulsion

Since the masses of the nuclei are much greater than the masses of the electrons, their velocities are much smaller. Therefore the Born-Oppenheimer approximation, which assumes that the nuclei are fixed, eliminating thus their kinetic energy and making the repulsion potential energy constant, can be applied. The total wavefunction can be split into two parts, one describing the electronic wavefunction

for a fixed nuclear geometry, and the other describing the nuclear wavefunction. The electronic wavefunction depends only on the positions of the nuclei. Hence during calculations only the nuclei positions are varied, while a solution for the electronic Schrödinger equation is found. From these multiple derivations a potential energy surface for polyatomic system is obtained. From this surface the different geometries of the molecule, corresponding to transition states and local minima, can be attributed. Although this approximation has an error of less than 0.1% in the energy determination, it is important to note that for the systems studied in the following work, it will give rise to non-adiabatic interactions for some calculations carried out for excited states.

Even after the Born-Oppenheimer approximation, the solution to the electronic Schrödinger equation can be found only for a simple one-electron system such as H_2^+. Because electrons react to the presence of one another, another assumption has to be made, which sees the dynamic potential energy of repulsion replaced by the Hartree Fock potential (HF),. This assumes that each electron is moving in a uniform field generated by the presence of the other electrons, so that the potential energy of electron repulsion is constant. This assumption gives rise to a reasonably accurate geometry, which accounts for almost all of the energy of the molecule. Unfortunately this method is not sufficient. Indeed, it assumes that there is the same probability of finding electrons at the same place in space as to be spread out throughout the molecule. This is obviously wrong since we know that electrons repel each other. Some complementary assumption can be made such that once one electron position is defined the other will be placed in another region. The self-consistent field method uses the Pauli Principle and assigns each electron a spin. Each orbital for a closed shell system will be composed of two electrons with different spins. Therefore the Hartree-Fock wave function does include some correlation of the motions of electrons with the same spin.

1.3.3 Electron correlation methods

Although, as previously seen, the Hartree Fock method often supplies a reliable geometry, its absolute energy is generally not reliable. This is essentially the consequence of the fact that it describes the behaviour of an electron in the net field of all other electrons, and not individually. Electrons must move to avoid each other, i.e. their motions must be correlated. The difference between Hartree Fock for a given basis set and the exact non-relativistic energy corresponds to the correlation energy, generally around 1% of the total Hartree Fock energy. Three methods for calculating correlation energy are generally used in *ab initio* molecular orbital (MO): configuration interaction (CI), many-body perturbation theory (MBPT), and coupled cluster. In the following work only the first two methods have been used and are summarised below.

In the CI method, electron correlation is introduced by exciting the electrons; these electrons are excited from occupied to unoccupied virtual orbital to produce different electron configurations. The CI wave function can be summarized as follows:

$$\Psi = c_0\Phi_0 + \sum_S c_S\Phi_S + \sum_D c_D\Phi_D + \sum_T c_T\Phi_T + \ldots \qquad \text{EQ 1.15}$$

where the first term, $c_0\Phi_0$, is the Hartree Fock solution, and S, D, T, are single, double and triple configuration interaction terms respectively, which correspond to single, double and triple excitation. Although it is required to perform Full CI for "true" energy, these calculations are rarely carried out for more than diatomic systems. To reduce computing cost configuration interaction singles and doubles can be performed routinely (CISD). These are routinely carried out for reasonably large molecules and basis functions. This truncated methodology, unlike full CI, is not size consistent, and so the accuracy in energy correlation is dependent on the number of electrons. Whereas for a 20–electron molecule CISD returns 82-90% correlation energy this drops to 55-67% for 100-electron molecules.

In the following work, the electron correlation is added using the many-body perturbation theory formulation of Møller and Plesset. This method will not try to truncate the "true" wave function as for CISD, but instead attempts to treat it as a sum, the second term being a perturbation of the first term (the HF wavefunction). The total Hamiltonian operator, H_λ, is written as the sum of a 'zero-order', unperturbed, Hamiltonian, H_0, the Hartree Fock wavefunction, and a perturbation λV such as:

$$H_\lambda = H_0 + \lambda V \qquad \text{EQ 1.16}$$

where

$$\lambda V = \lambda(H - H_0) \qquad \text{EQ 1.17}$$

where H is the "true" Hamiltonian and λ is a dimensionless parameter.

The ground state wave function Ψ_λ and energy E_λ for a system described by the Hamiltonian H_λ are expanded as a Taylor series of λ as:

$$\Psi_\lambda = \Psi^{(0)} + \lambda\Psi^{(1)} + \lambda\Psi^{(2)} + \ldots \qquad \text{EQ 1.18}$$

$$E_\lambda = E^{(0)} + \lambda E^{(1)} + \lambda E^{(2)} + \ldots \qquad \text{EQ 1.19}$$

The different orders of the Møller-Plesset perturbation theory are obtained by truncating the above to various orders. Truncating at first order Møller-Plesset expansion series (MP1) simply gives the Hartree-Fock energy. The second order (MP2) method is one of the most commonly used methods of including correlation. MP2 can recover a large fraction of the correlation in energy when the Hartree-Fock wavefunction provides a good initial description. An oscillation in energy and structural prediction is noticed in going from second order to third and higher orders. The MP3 method usually provides little improvement over the MP2 method with respect to molecular properties. For this reason it is rarely employed. Some MP4

calculations are used in this work, although they are only carried out at single, double and quadruple excitation MP4(SDQ).

1.3.4 Density Functional Theory

Many body perturbation theory and configuration interaction are, as seen before, computationally expensive, and hence there is a need to include electron correlation by other less expensive means. This was achieved by the introduction of density functional theory (DFT) in the mid sixties, following the theory of Hohenberg and Kohn in 1964. This theory states that for all ground state properties, independent of the system, the total energy of polyatomic systems is a function of the electronic density ($E(\rho)$). The total energy consists of contributions from the kinetic energy $E_{KE}(\rho)$, the electron-electron Coulombic energy $E_H(\rho)$, a term describing the electron nuclear interaction, $E_C(\rho)$, and $E_{XC}(\rho)$, which contains the exchange and correlation contributions such as:

$$E(\rho)= E_{KE}(\rho) + E_C(\rho) + E_H(\rho) + E_{XC}(\rho) \qquad \text{EQ 1.20}$$

Since so far there is no energy functional that can derive the energy of a system from solely its electronic density ρ, other assumptions had to be made. The first method, Local Spin Density Approximation (LDSA), treats the density locally as a uniform electron gas. Unfortunately at best it underestimates the exchange energy by 10%, resulting in overestimation of bond strengths. The Generalized Gradient Approximation (GGA) methods, by means of making the exchange and correlation energy dependent on both the electron density and its derivative, create a non-uniform "electron gas". The purist would use the algorithm developed by Perdew and Wang PW91[24] or the one developed by Lee, Yang and Parr (LYP[25,26]). Most functionals are still under development. Nowadays the pure DFT methods are more and more replaced by hybrid DFT. In this work the B3 electron exchange functional and the LYP correlation functional (B3LYP[27]) will be used. It has to be emphasized that this last method is generally not considered to be purely *ab initio* since it is empirically weighted for a specific series of compounds.

1.3.5 The origin of the basis set: simplifying Ψ

The wave function in the Schrödinger time-dependent equation gives the probability density of nuclei as well as the electrons. Due to the fact that the Born-Oppenheimer approximation assumed the nuclei to be fixed, in molecular orbital theory the wave function is described by one-electron functions, so-called orbitals. Quantum calculations for molecules are carried out using a localized description at the atomic level. In 1951 Roothaan proposed expanding the spatial molecular orbitals as a linear combination of atomic orbitals (LCAO), later replaced by the term "basis functions", which describes the molecular orbital as:

$$\Psi_i = \sum_{\mu=1}^{n} C_{\mu i}\phi_\mu \qquad \text{EQ 1.21}$$

where Ψ_i is the i^{th} molecular orbital, $C_{\mu i}$ are the coefficients of the linear combination known as the molecular orbital expansion coefficients for orbital i, ϕ_μ is the μ^{th} atomic orbital, and n is the number of the atomic orbital. The description of Ψ_i is improved by increasing the number of basis functions used. The combination of all basis functions describing the set of atomic orbital per nuclei is referred to as a basis set.

There are two types of basis function, commonly used in electronic structure calculations and centred on the nuclei: the Slater Type Orbitals (STO) and Gaussian Type Orbitals (GTO).

STO were the first basis functions used due to their similarity to the atomic orbital of the hydrogen. They are described by the following functional in spherical coordinates:

$$\phi_{\zeta,n,l,m}(r,\theta,\varphi) = Nr^{n-1} e^{-\zeta r} Y_{lm}(\theta,\varphi) \qquad \text{EQ 1.22}$$

where N is a normalization constant, ζ is the orbital exponent, $Y_{lm}(\theta,\varphi)$ is the angular momentum part, which describes the shape of the function. The n, l and m are the principal, angular momentum, and magnetic quantum number. Linear combinations of STO lead to rapid convergence for the atomic description, but unfortunately, for 3 and 4-centre two-electron integrals, they are unsuitable for fast calculations, and are too difficult to solve analytically. They do not have closed forms.

It is for computational efficiency that Samuel Francis Boys decided in 1950 to replace the STO by the GTO. The GTO can be expressed as functions of cartesian and polar coordinates:

$$\phi_{\alpha,a,b,c}(x,y,z) = Nx^a y^b z^c e^{-\alpha r^2} \qquad \text{EQ 1.23}$$

$$\phi_{\alpha,n,l,m}(r,\theta,\varphi) = Nr^{(2n-2-l)} e^{-\alpha r^2} Y_{lm}(\theta,\varphi) \qquad \text{EQ 1.24}$$

where α is the Gaussian exponent, which alters the width of the Gaussian function and a, b and c are integers that determine the type of GTO. As shown in **Table 1.1,** whereas in polar coordinates there are 5 components in order to describe the 5 linearly independent and orthogonal d-type orbitals, in Cartesian coordinates there are six such components. However, since $\mathbf{r^2=x^2+y^2+z^2}$, from the Cartesian representation we have 5 d-type functions and one extra s-type function as:

$$3d_x^2 + 3d_y^2 + 3d_z^2 = N(x^2 + y^2 + z^2) e^{-\alpha r^2} = Nr^2 e^{-\alpha r^2} = 3s$$

Table 1.1: Some orbital descriptions in polar coordinates

exponents	a	b	c	orbital type
0	0	0	0	1s
1	1	0	0	$2p_x$
1	0	1	0	$2p_y$
1	0	0	1	$2p_z$
2	2	0	0	$3d_{xx}$
2	1	1	0	$3d_{xy}$
2	0	2	0	$3d_{yy}$
2	0	1	1	$3d_{yz}$
2	0	0	2	$3d_{zz}$
2	1	0	1	$3d_{xz}$

GTO having been developed to cut the computing cost, has some flaws as shown. The dependent r^2 in GTO (solely r in STO) contributes to the erroneous description near the nucleus, giving a zero slope at the nucleus whereas a cusp is present in the STO description, as shown in **Figure 1.7** (a). For large r the Gaussian function dies too fast with respect to the true radial wave function, which STO mimics accurately.

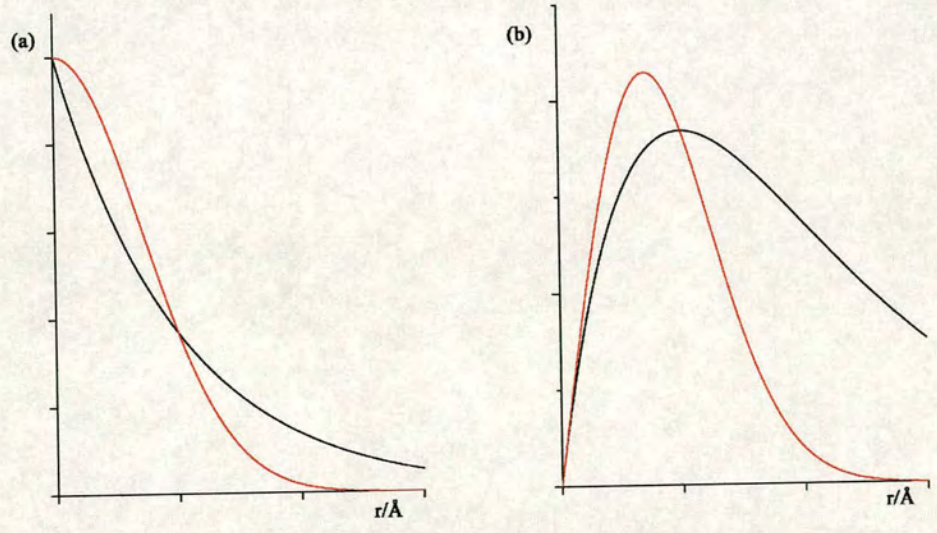

Figure 1.7. STO (black curve) vs. GTO (red curve) representing:
1s radial wavefunction (a) and 2p radial wavefunction (b)

To minimize the underestimation of the long-range overlap between atoms in a polyatomic system, combinations of Gaussian functions are used. Even though more primitive functions are needed for similar results than with STO, the basis function of GTO is still less computationally demanding.

As seen previously the Gaussian expansion contains two parameters, the coefficient and exponent, which in an ideal case would be allowed to vary during the calculation. For computing efficiency and in this work, some primitive Gaussians will be substituted by basis sets, which consist of the relevant exponents and coefficients of Gaussians to represent molecular orbitals, made of contracted Gaussian functions for which the coefficients and exponents are predetermined and remain constant.

The most popular families of basis sets and the ones generally applied in this work are those of Pople and Dunning. The minimal basis set, in other words, the smallest possible set, contains only one function per occupied atomic orbital in the ground state. The most common of these are the STO-*n*G, where *n* corresponds to the number of primitive contractions. These sets are obtained by least-squares fit of combinations of *n* Gaussian functions to a STO (with ζ=1). Since at least three Gaussian functions are understood to represent reasonably well each Slater type orbital, STO-*3*G is the most common minimal basis set used. These single ζ basis sets, have major drawbacks since they use the same number of functions to describe the atoms at the beginning and at the end of the period. Only being described by one Gaussian for each orbital for which the exponents are constrained, the atomic orbitals are not allowed to "adapt" to the molecular environment, which results in erroneous structures.

Doubling the number of functions to describe each orbital allows one set to be closer to the nucleus, with larger exponents, and the other set to be looser, with smaller exponents. These double-ζ basis sets would therefore allow flexibility in describing the electron cloud. Increasing further the number of functions representing each

orbital (triple, quadruple ζ etc...) will not necessarily improve the model but definitely will increase the computing cost dramatically.

Since the minimal basis sets STO-3G do not describe non-spherical electron distributions in molecules and since the core orbitals unlike the valence orbitals do not affect chemical properties of molecules, split valence basis sets were developed. This type of basis set (in Pople notation) have the form *n-ij*G and *n-ikj*G where *n* is the number of primitives for the inner shells, *ij* and *ikj* are the number of primitive contractions in the valence shell, *i* the inner, *k* the middle and *j* the outer part of the valence orbitals. *ij* and *ikj* correspond to double ζ and triple ζ respectively. In the Dunning notation the split valence is denoted by the use of the letter V. DZV represents the basis set with only one contraction for inner orbitals, and two contractions for valence orbitals.

Because calculations are performed solely with regard to the atoms, the molecular structure of hydrogen gas derived using solely 1s GTO gives rise to an erroneous structure as shown in **Figure 1.8**. The flexibility of the basis set is increased by adding a basis function of higher angular momentum quantum number denoted by "*" or "(d,p)" in Pople notation and "p" in Dunning. This enables displacements of the electronic charge away from the nuclear centres, allowing a correct description of the molecular orbitals. For anions, for very electronegative atoms or those with lone pairs of electrons, the orbitals need more space, allowing the electrons to be pulled further away from the nucleus. The diffuse functions denoted "+" and "aug" in Pople and Dunning notation have for this purpose functions with very small exponents added to the basis set.

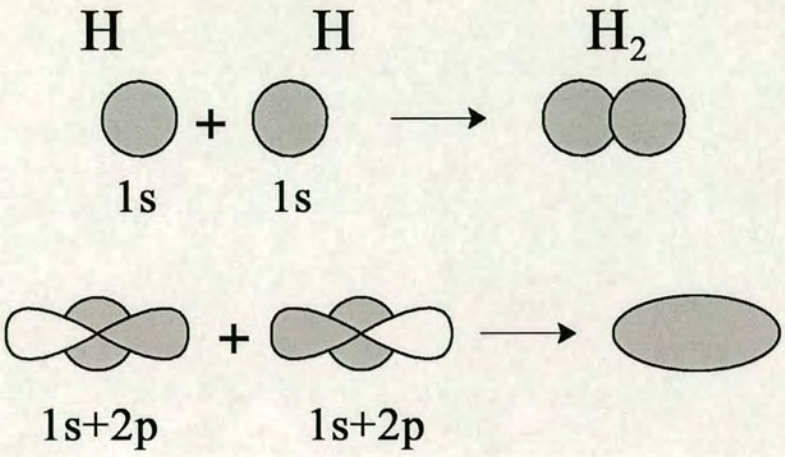

Figure 1.8: Effect of adding a polarization function for a better mathematical description of Hydrogen gas

Table 1.2: Example of 6-311++G(d,p) basis set with hydrofluoric acid

Atoms	core orbitals	part of the valence orbitals			diffuse	polarization	total	
		inner	middle	outer			primitives	contracted
H		3s	1s	1s	1s	1p	6s1p	4s1p
F	6s	3s3p	1s1p	1s1p	1s1p	1d	12s6p1d	5s4p1d

This work used the correlation-consistent (*cc*) basis function to allow better extrapolation of the basis set limit. In fact, the basis sets are designed so that functions that contribute similar amounts of correlation energy are included at the same stage, so that, in order to go from cc-pVDZ to cc-pVTZ, 1d and 1f extra functions are needed for second row atoms. These are built up shell by shell.

In conclusion the larger the basis set the more accurate, in principle, the calculations but also the more computationally expensive these are. Where the Dunning correlation-consistent basis sets are specifically designed for use with conventional correlation methods such as MP2, the Pople basis sets are the most widely used and have been found to have a robust accuracy independent of the method. The quality of the computational results depends on the description used for the molecule.

1.4 **Conclusions**

Ab initio calculations have to find a solution to the Schrödinger equation, but since it is impossible to solve the equation analytically for polyelectronic systems, previously mentioned methodologies make assumptions allowing an approximation more or less close to the true solution, as seen in **Figure 1.9**.

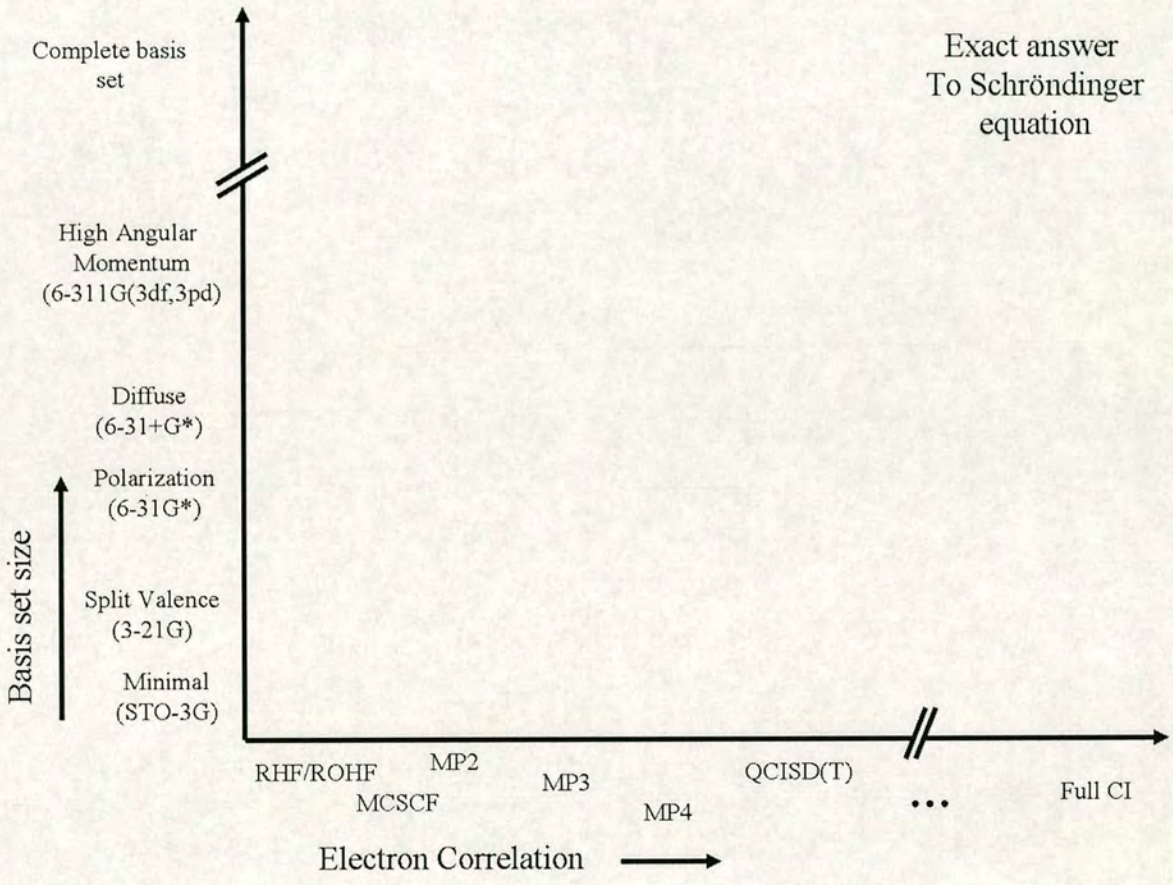

Figure 1.9 Finding the solution to the Schrödinger equation

For all *ab initio* methods there are 4 sources of error arising from: the Born-Oppenheimer and adiabatic approximations, the use of incomplete basis sets, the incomplete allowance for correlation and omission of relativistic effects. Since HF does not include enough repulsion nor enough interaction, the covalent bond is often too short whereas the electrostatic interactions are too long. MP2 often overestimates the effect of electron correlation, resulting in too large bond lengths. Being widely

used, its weaknesses are well documented. It has a speed advantage over all other MP methods and is much faster then CI. The main weakness of Hybrid DFT is the poor description of the van der Waals type interaction resulting in the overestimation of bond strengths. Overall for electron-correlation calculations, the errors coming from the truncation of the basis set are larger than the errors arising from the truncation of the electron treatment. Therefore a full basis paired with MP2 will perform better than full CI with a poorly defined basis set.

1.5 References

1 H. Mark and R. Wierl, *Phys. Z.*, 1930, **60**, 741.

2 A. J. Blake, P. T. Brain, H. McNab, J. Miller, C. A. Morrison, S. Parsons, D. W. H. Rankin, H. E. Robertson and B. A. Smart, *J. Phys. Chem.*, 1996, **100**, 12280; P. T. Brain, C. A. Morrison, S. Parsons and D. W. H. Rankin, *J. Chem. Soc., Dalton Trans.*, 1996, 4589; N. W. Mitzel and D. W. H. Rankin, *J. Chem. Soc., Dalton Trans.*, 2003, 3650.

3 S. L. Hinchley, M. F. Haddow and D. W. H. Rankin, *Dalton Trans.*, 2004, 384.

4 Louis de Broglie. *Compt. Rendus*, 1922b, **175,** 811.

5 Louis de Broglie. *Compt. Rendus*, , 1923a, **177,** 507, 548, 630.

6 Louis de Broglie. *Nature*, 1923b, **112,** 540.

7 Louis de Broglie. Thèse de doctorat, Masson, Paris; *Ann. De Physique,* 1925, **3,** 22.

8 Clinton J. Davinson, Lester H. Germer. *Phys. Rev.*, 1927, **30,** 705

9 George P. Thomson. *Nature*, 1927, **120,** 802.

10 P. P. Debye, *Physik. Z.*, 1929, **30,** 84.

11 R. Wierl, *Physik. Z.*, 1930, **31,** 1028; *Ann. Physik*, 1931, **8,** 521.

12 L. Pauling and L. O. Brockway, *J. Am. Chem. Soc.*, 1935, **57**, 2684.

13 L. Pauling, *The Nature of Chemical Bond Ithaca*, New York: Cornell University Press.

14 F. Trendelenburg, *Naturwissenschaften*, 1933, **21**, 173.

15 Chr. Finbak, *Avh. Norsk.Vidensk. Akad. Olso*, 1937, **13**.

16 P. P. Debye, *Physik Z.*, 1939, **40**, 66; **40**, 404.

17 J. R. Lewis, P. T. Brain and D. W. H. Rankin, *Spectrum*, 1997, **15**, 7.

18 V. Schomaker, R. Glauber, *Nature*, 1952, **170**, 4320; R. Glauber, V. Schomaker, *Phys. Rev.*, 1953, **89**, 667.

19 S. L. Hinchley, University of Edinburgh, PhD Thesis, 2000.

20 Shrink, V.A. Sipachev, *J. Mol. Struct.* (Theochem), **121**, 143, 1985; V.A. Sipachev, "Vibrational Effects in Diffraction and Microwave Experiments: A Start on the Problem", Advances in Molecular Structure Research, I. Hargittai and M. Hargittai (Eds.); V.A. Sipachev,

"Anharmonic Corrections to Structural Experiment Data", *Struct. Chem.*, **2/3** 167, 2000; V.A. Sipachev, "Local Centrifugal Distortions Caused by Internal Motions of Molecules", *J. Mol. Struct.*, **567-568**, 67, 2001. M. Iwasaki and K. Hedberg, *J. Chem. Phys.*, **36,** 2961, 1962.

21 J. R. Lewis, R. J. Mawhorter, S. L. Hinchley, D. W. H. Rankin, *manuscript in preparation.*

22 S. L. Hinchley, H. E. Robertson, K. B. Borisenko, A. R. Turner, B. F. Johnston, D. W. H. Rankin, M. Ahmadian, J. N. Jones, A. H. Cowley, *Dalton Trans.* 2004, 2469.

23 S. Cradock, J. Koprowski and D. W. H. Rankin, *J. Mol. Struct.*, 1981,**77**, 113.

24 J. P. Perdew and W. Yang, *Phys. Rev. B*, 1992, **45**, 13244.

25 C. Lee, W. Yang and R.G. Parr, *Phys. Rev. B*, 1992, **37**, 785.

26 B. Miehlich, A. Savin, H. Stoll and H. Preuss, *Chem. Phys. Lett.*, 1989,**157**, 200.

27 A. D. Becke, *J. Chem. Phys.*, 1993, **98**, 5648.

Chapter 2

New Nozzle Design:
The Slit Nozzle

2.1 **Introduction**

SARACEN[1] and DYNAMITE[2] are new methodologies developed by the Edinburgh gas-phase structure group to tackle the structure determination of bulkier asymmetric molecules. Unfortunately many larger molecules have vapor pressures inadequate for the gas-phase experiment conditions. Therefore our current work aims to provide new ways to overcome both the kinetic and thermodynamic challenges of the problem by the adoption of a new nozzle design and by the use of a reservoir (see chapter 3).

The new nozzle will extend the capabilities of gas electron diffraction to compounds with lower vapour pressures or with vaporisation rates that are not adequate for the existing GED experimental conditions. The shape of the new nozzle would allow it to operate at lower vapour pressures by increasing the diffraction area. The best design we have investigated is the slit type. This design allows the electron beam diameter to be kept small, permitting the gas to emerge from a slit running parallel to the beam. The diffraction zone would thus be elongated, while maintaining the normal diameter. A 0.5 cm long slit nozzle has been investigated, enhancing the molecular flow rate by a factor of 5.5. The major inconvenience of such a design is the potential increase in background scattering generated by electrons diffracted outside the area of the nozzle or, especially, secondary diffracted electrons and more importantly the scattering pattern becomes more diffuse. The tip would thus not be one single point any more but a series of points, causing more uncertainty. A clear advantage is that exposure times will be kept similar to those of the normal nozzle, used with more volatile compounds, and, as a consequence, the reduction of the scattering during the experiment due to lack of sample and falling background, will be less of a problem.

Initially some description of the techniques that already exist will be given. Examples will include new nozzle designs which have been tried in the past but have failed. The manufacturing and the technical descriptions will then be given prior to an extensive simulation of data potentially generated by the type of nozzle chosen,

via the use of a simple program which will be described. Data for standard compounds including benzene, carbon dioxide and acetone were later collected and compared to their respective simulations.

2.2 **What is available?**

Eighty years ago, the first gaseous experiments were aimed at molecules that had an acceptable vapour pressure at room temperature. But soon this became a limiting factor and therefore a specialised field of research was created: high temperature electron diffraction. At first the nozzle system was used to regulate the flow of the sample for the highly volatile compounds.[3] Later on, new systems were developed, aimed at high temperature, and the designs of these new nozzles were diverse. Initially, they were all created to study alkali halides and other halide-substituted molecules for which a sufficiently high pressure could only be obtained for temperatures near 1400°C. Although most of these studies were carried out at these temperatures in the seventies with early investigations in the sixties,[4] in the nineties fullerene was the starting point for the launch of new high temperature nozzles. Heating at these high temperatures is already a challenge by itself, but in electron diffraction experiments, the creation of an electromagnetic field has to be avoided while the high temperature molecular beam crosses the path of the electron beam.[5] To reach such high temperatures two main designs are used: radiation and electron bombardment nozzles.[4,5] The first system developed consists of using radiation emitted by tungsten wires to heat the sample chamber. These wires have to be shaped a certain way to avoid any electromagnetic disturbance since, for most of these systems, the nozzle and sample chamber are close to one another as shown in **Figure 2.1**. With this type of design, temperatures up to a maximum of 800°C could be reached.[4]

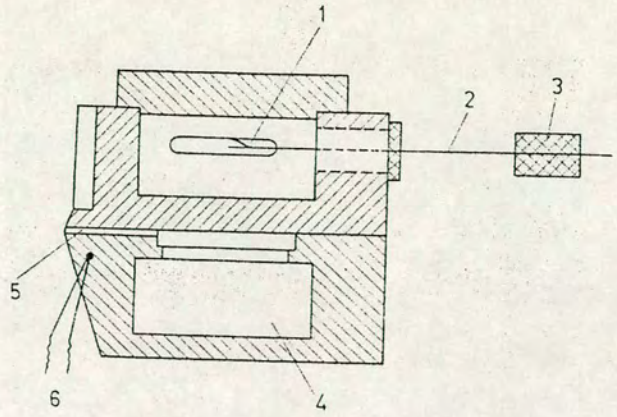

Figure 2.1: Cross section of the radiation nozzle system. (1) filament, (2) supporting rod, (3) ceramic supporter, (4) sample container, (5) nozzle capillary, (6) thermocouple.[5,6]

At Moscow State University the electron bombardment apparatus was developed allowing experiments to be carried out at temperatures of up to 2500°C. Fast electrons, generated by the heated filament, are aimed at the sample container. It is upon deceleration of the electrons hitting the sample chamber that the energy is released and used to heat the sample. A typical design of this kind can be seen in **Figure 2.2**. For the example shown, the sample container is placed inside the apparatus to shorten the path along which the vapour must be maintained at the preset temperature and to decrease the difficulty of insulating the diffraction chamber body.

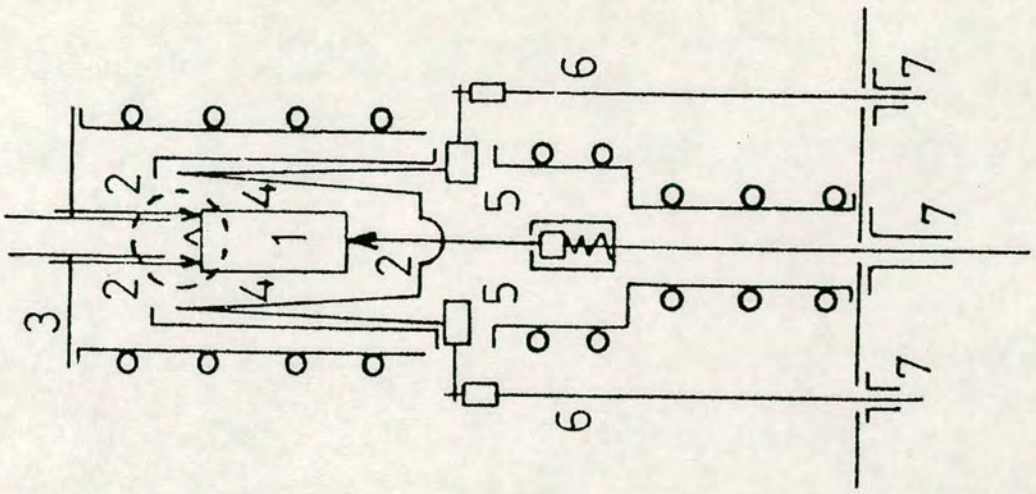

Figure 2.2: Electron bombardment nozzle design in Moscow State University. (1) sample container, (2) supporting pivots, (3) cover, (4) filaments, (5) insulators, (6) current –conducting rods, (7) vacuum-seals.[5]

In Edinburgh, the compounds are studied at intermediate temperatures. The nozzle can be heated up to 230°C. Its design differs a lot from the commonly used nozzle. The sample source lies outside the diffraction chamber. The nozzle is heated up by a flow of hot air provided by a flameless torch. Although the torch could provide hot air up to 1000°C the seal used in the nozzle has a much lower temperature limit. The sample is heated outside the diffracting chamber with the use of electric tape. The differential in temperature, increasing from the sample to the tip of the nozzle, allows the gaseous molecule to be driven forward and avoid any condensation, before crossing the path of the electron beam. The Edinburgh nozzle is shown in **Figure 2.3**.

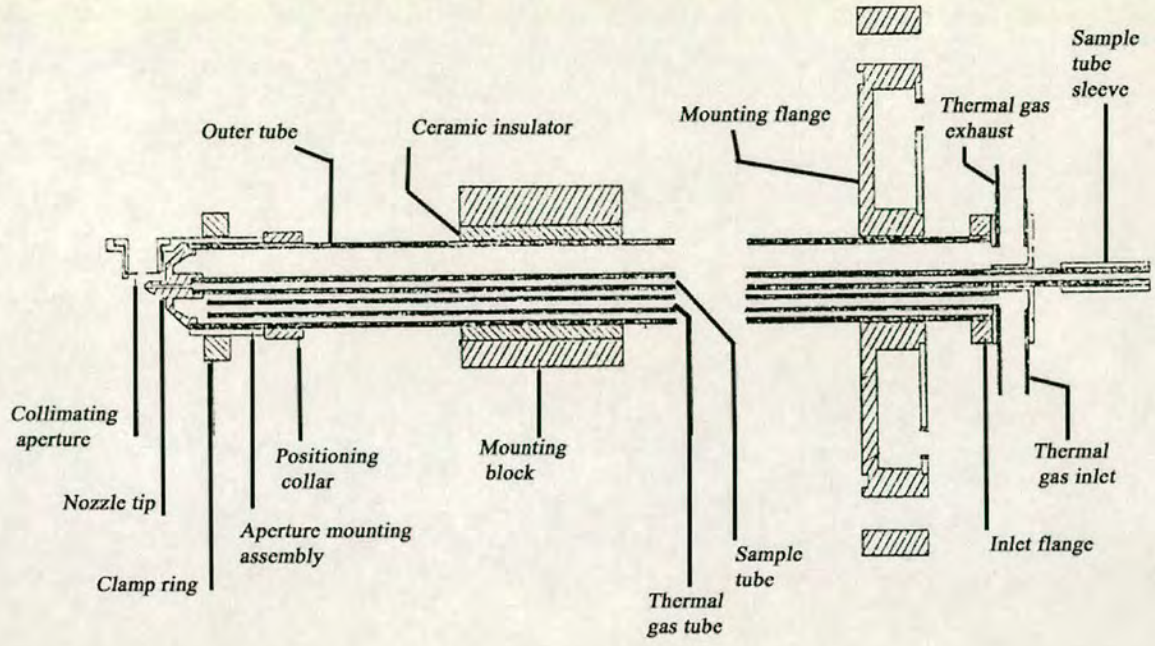

Figure 2.3: Schematic cross section of high-temperature nozzle at the University of Edinburgh.

In the fifties, Simon Bauer investigated new designs for nozzles.[7] Two assumptions made in electron diffraction are that the samples are diffracted from one single point and that no multiple scattering takes place. The latter assumption is more or less met by the use of a cold trap (to catch the free gaseous molecules immediately after entrance to the diffraction chamber, which reduces the number of free molecules outside the area above the tip of the nozzle). On the other hand, the first assumption is never true due to the physical properties of the gas flow, which will be discussed later.

The hypothesis made by Professor Bauer can be summarized by Equations 1 and 2, which are related to **Figure 2.4**. He stated that the useful diffraction E_p over time is the principal diffraction pattern, diffraction of the main beam over the nozzle, while the gas existing throughout the diffraction chamber gives rise to many overlapping patterns, contributing to the background.[7] Therefore the useful diffraction can be expressed by the following equation:

$$E_p(t) = \frac{Q_{nozzle}}{Q_{nozzle} + Q_{camera}} \qquad \text{EQ 2.1}$$

where Q_{nozzle} is the primary beam diffracted just above the nozzle tip area averaged over time t, whereas Q_{camera} includes the rest of the diffracted electrons, also averaged over time. With the help of **Figure 2.4** this equation takes the form:

$$E_p(t) = \frac{C_1 + C_3}{C_1 + C_2 + C_3 + C_4} \qquad \text{EQ 2.2}$$

where C_n are the relative contributions of n primary, secondary etc. diffracted beams in **Figure 2.4**.

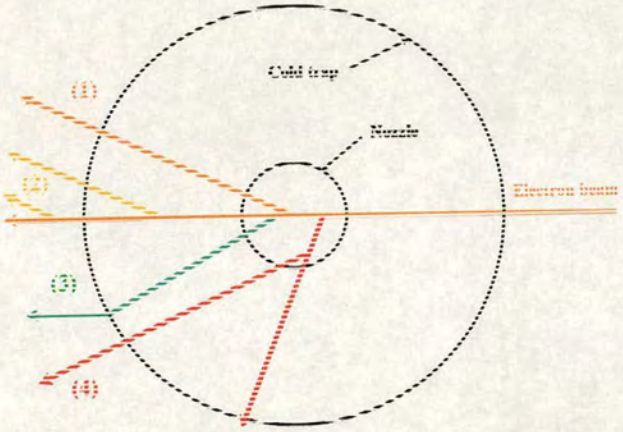

Figure 2.4: "Useful Diffraction" E_p: (1) primary diffracted beam, (2) primary diffracted beam outside nozzle, (3) secondary diffracted beam outside the nozzle, (4) secondary diffracted beam.

It is important for the new nozzle design not to increase the contributions of 2 and 3. The primary diffracted beam, outside the nozzle area (2 in **Figure 2.4**), should be eliminated by the use of an efficient cooling system. Tests in the lab have been run to check that, when the main beam is not going over the nozzle while gaseous molecules enter the chamber, little or no diffraction is collected on the photographic films. Hence, in the Edinburgh apparatus case, the cooling system and vacuum

system work well and avoid any extraneous diffraction outside the area of the nozzle. A high efficiency $E_p(t)$ is therefore expected.

The main part of this work was to design a new nozzle tip that would increase the contact of the molecular beam with the electron beam. In Norway, an annular nozzle was tested as shown in **Figure 2.5**, the gaseous molecules come out from the entire ring while the electron beam passes through the ring. This will increase the contact volume for the molecular and electron beams. Based on unpublished work[8] on the new design approach, it can be concluded that the obtained results were unsatisfactory. Looking more closely at the diagram it can be seen that the gaseous molecules coming out of the nozzle are constrained, so that their only way out is through the electron beam, increasing extraneous diffraction outside the area that is within the nozzle. Using this design, molecules are more likely to collide with one another while crossing the electron beam since they are coming out from opposite sides.

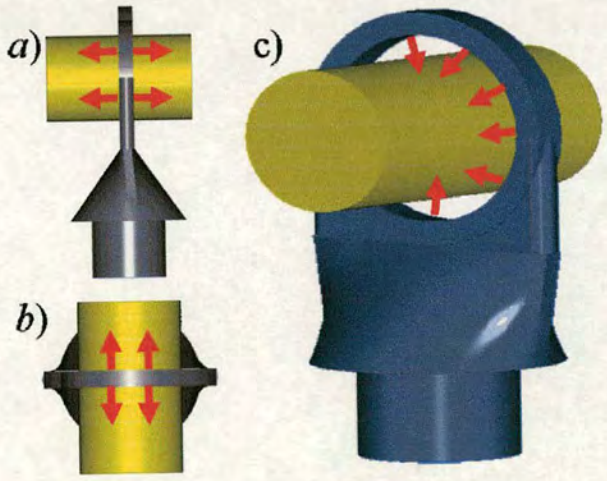

Figure 2.5: Norwegian annular nozzle: *a*) side view *b*) top view c) isomeric view. (red arrows show the flow of gaseous molecules coming out of the annular nozzle)

At the time of the selection, the chosen slit nozzle shape had not been previously published, implying that the slit form was original. However, it was brought to our attention at a conference that a similar design was tried and failed in the late sixties.[9]

As shown in **Figure 2.6**, to eliminate distortion caused by the rectangular shape of the nozzle, Professor Heinz Oberhammer decided to utilize a two-lens system which focuses each point along the length of the nozzle to the same point of the second focal plane of the apparatus. This system would allow the collection of short and long data by changing the nozzle image plane with the convergence of the lens. Since the work has never been published, no conclusion can be drawn as far as results are concerned, but it seems likely that success was not achieved. It must be emphasized that an attempt was being made to correct for an effect before knowing if it even existed. A simpler approach would have been to collect data and then deconvolute rather than trying to deconvolute prior to collection. The earlier method might have increased the amount of erroneous information, and hence the loss of any useful information and publishable work. Our strategy, consisting of collecting data prior to any deconvolution, will prove to be the better solution. If any unforeseen problems arise after data collection, *a posteriori* corrections will be made.

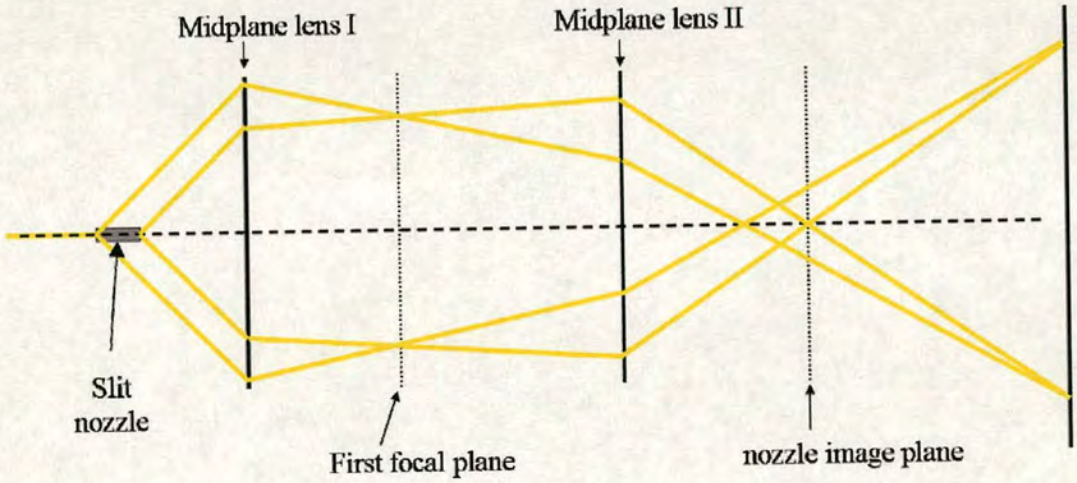

Figure 2.6: Principle of previous attempt using the slit nozzle reported to have taken place in 1961.

2.3 Nozzle design

Before describing the new design adopted for the tip of the nozzle, an introduction to the conventional nozzle should be made. The conventional nozzle (**Figure 2.7**) has

an opening of 0.5 mm in diameter and is 9 mm in height. It is manufactured from aluminium. The nozzle is placed perpendicular to the electron beam. With this type of design, it is assumed that the diffraction is occurring at a single point just above the nozzle opening. The 500 μm diameter is sufficiently small to have a negligible broadening effect on the data.

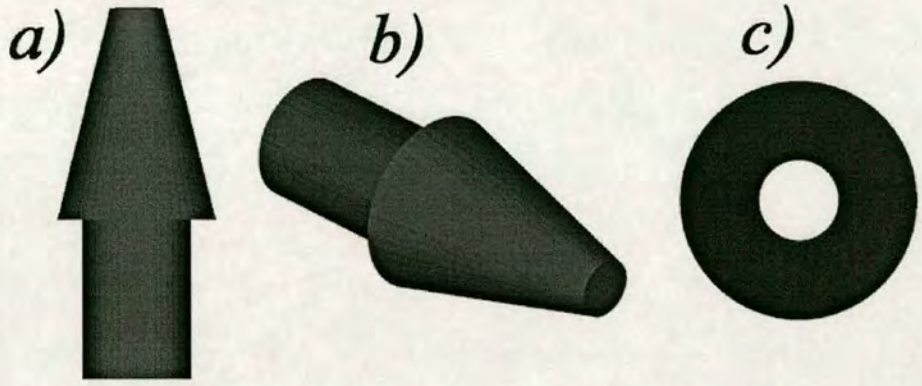

Figure 2.7: Conventional nozzle: a) side view, b) isomeric view, c) top view.

In the fifties, Prof. Simon Bauer commented on the adoption of the slit nozzle that would run perpendicular to the electron beam, stating that it "will not be satisfactory in this respect because the issuing gas stream is then poorly collimated".[7] Although this may have been true for the Norwegian design, in the chosen design for this work the slit will be running parallel to the electron beam as shown in **Figure 2.8**, and so the suggested problem might not arise. This is confirmed by the finding of Yonezo Morino in 1965 that in the case of a symmetrical nozzle, the "conventional nozzle", the gas distribution has its centre exactly over the nozzle and fades away symmetrically from the centre in all directions. Morino found that the gas flows faster in the central part than in the outer part of the nozzle and also that the mean free path in the nozzle is estimated to be 0.03 mm, which is much smaller than the diameter of the nozzle (0.55 mm).[10] Since the slit nozzle is symmetrical along the electron beam, a similar behaviour could be expected in the distribution of the gaseous molecule. Therefore we should expect a Gaussian distribution function along the slit.

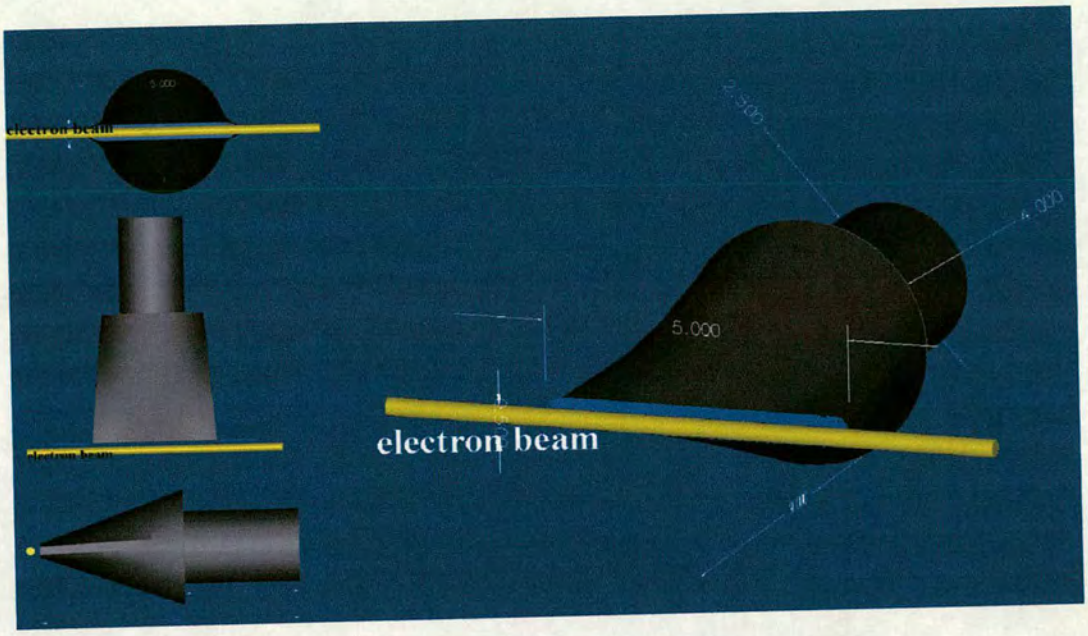

Figure 2.8: The new slit nozzle.

The new nozzle will have a slit length of 5 mm that will be, as stated previously, parallel and will keep the width of the conventional nozzle (0.5 mm) as seen in **Figure 2.8**. It will therefore behave, in theory, similarly to the standard nozzle. The shape of the new nozzle allows the user to operate at a lower vapour pressure by increasing the diffraction volume. It allows the electron beam diameter to be kept small, while the diffraction zone is elongated. Theoretically ten times more electrons should be diffracted while using the slit nozzle versus the conventional nozzle. It is an imperative in the manufacturing of the new nozzle that a smooth transition is obtained between the cylindrical part of the nozzle and the slit itself.

The Edinburgh workshop produced a prototype nozzle in stainless steel, **Figure 2.9**, based on a technical drawing. It has been noted that because of technical difficulty, the nozzle ended up being higher than the conventional nozzle. However, since it was designed for a room temperature experiment, the risk of the gaseous molecules condensing inside the nozzle is zero.

Figure 2.9: prototype slit nozzle.

The purpose of this work was to tackle molecules with vapour pressures that are borderline with respect to the limit of the Edinburgh apparatus. A smaller version of the prototype had to be made with exactly the same dimensions as the conventional nozzle with the exception of the size of the opening. Therefore the height of the nozzle that was adapted for high temperature experiments is 9 mm. In this case the high temperature versions were made of aluminium by the workshop. The nozzle has to be placed with great care inside the GED apparatus, and the position of the slit is executed with reference to part of the apparatus, to ensure that the slit is parallel to the electron beam.

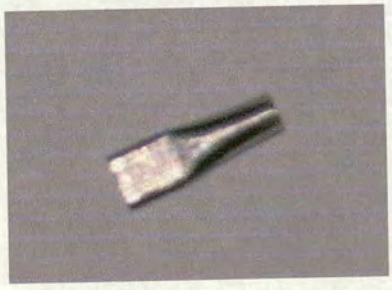

Figure 2.10: High temperature slit nozzle

A non-conventional method was used to produce these nozzles. It would have been ideal to electroform this nozzle, due to its small size. The process of electroforming begins with a piece of aluminium or stainless steel stock or bar. The internal geometry of the electroform is machined into the aluminium or stainless steel. This produces the mandrel. The mandrel dimensions for our nozzle can be found in

Appendix C on the CD. Then comes electrodeposition onto the mandrel to build a precise wall thickness of nickel, copper, gold, silver, or some combination thereof. Finally the mandrel is dissolved in caustic solution leaving behind the completed electroform. The advantages of such a technique are numerous: accuracy, reproducibility and strength. Unfortunately, as with every great finding, it has a tremendous drawback which is its expense.

From the metals available for electroforming, the best compromise would be the use of copper which demonstrates hard strength. Because of its reactivity with potential gaseous compound it would have to be plated with gold. Although gold is non-reactive and non-magnetic the fact that it is extremely soft would make it unsuitable for manipulation of the nozzle. Therefore building it out of gold only is not practical.

The ideal metals that can be chosen for nozzle design for the GED apparatus are heavy metals such as iridium and platinum for their non-reactivity with extraneous species, non-magnetic properties and their capacity of absorption of electrons. They all can sustain high temperature. As for molybdenum, most of these metals are hard and cannot be easily manufactured into specific shapes. In addition, no electrodeposition techniques exist for these heavy metals either.

2.4 **Theoretical simulation**

2.4.1 Program description

Prior to the collection of experimental data there was a need to simulate the diffraction parameters that would be expected from the slit nozzle. The simulation was performed using true experimental data, in order to see how the new nozzles would affect the structure determination if it were carried out without using the new deconvolution program. The Edinburgh calibration data, benzene (in this case at room temperature), were used to achieve this goal. The program made the simple assumption that the gas flows evenly from the entire slit. Thus the new nozzle can be thought of as a set of nozzles placed next to each other. The program averages out

the intensities from the entire set of pseudo nozzles and projects them as if they were coming from one point, situated at half the length of the new nozzle. By doing so we expect the shape of the molecular intensity curve to be similar to that from the single-point nozzle. In fact the data collected at the shortest distance from the camera would give rise to intensity proportionally smaller than those observed for the longer distance.

The electron beam is diffracted by gaseous molecules and the intensities are directly linked to a specific angle of diffraction. Since $s = \frac{4\pi}{\lambda} * \sin\left(\frac{\theta}{2}\right)$, where λ is the electron wavelength, it is understood that for each s value there is a specific intensity, which is independent of the nozzle-to-camera distance. Because each nozzle subdivision will give rise to the same intensities at a defined angle, the total intensity averaged at a point in the middle of the slit nozzle would not be the average of all these intensities, but the sum of the intensities extrapolated at that point.

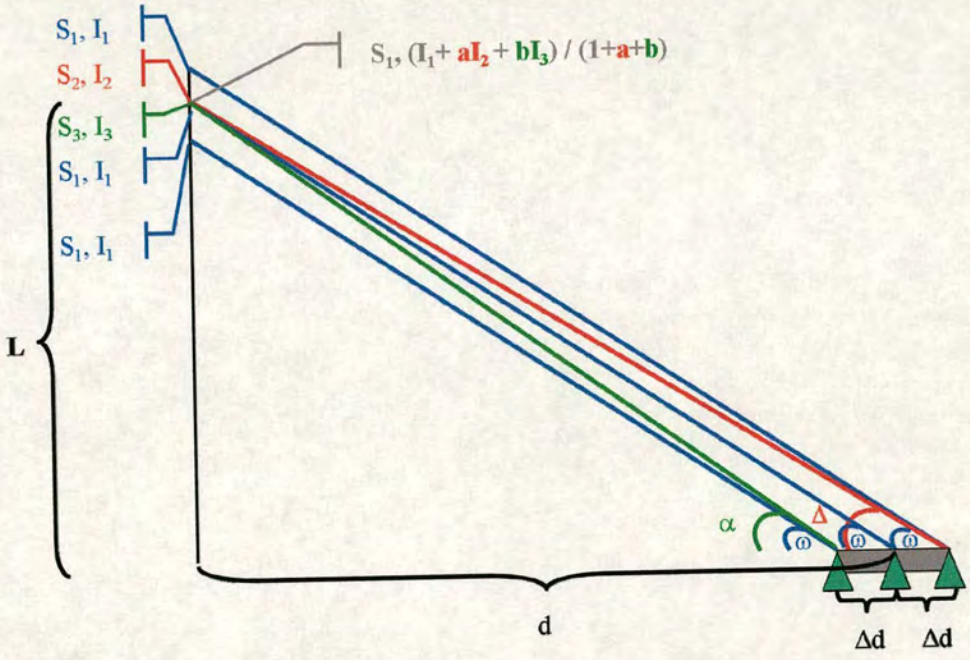

Figure 2.11: Slit nozzle split into three nozzles [each Greek letter refers to the angle of the same colour triangle]

Assuming that the slit nozzle is split into three independent nozzles, one at the distance d from the photographic plate and the other two at equidistant Δd to the middle nozzle, as shown in **Figure 2.11**, the overall intensities will be averaged at distance d. All three nozzles at s_1, have the same scattering intensity I_1, because they have the same diffraction angle ω. This information is taken from our experimental molecular intensity curves. Since these curves are plots of $s^4I(s)$, there is a need to retrieve the real intensity $I(s)$ by simply dividing the experimental data by s^4.

For simplification purposes, the experiment will be projected into a simple right angled triangle. S will be converted into L values, which are the distances from the centre of the photographic film to the regions of intensity. The experimental data used for simulations are the data collected for the nozzle at distance d. The conversion is done mathematically as follows:

Since:

$$s_1 = \frac{4\pi}{\lambda} * \sin\left(\frac{\omega}{2}\right) \qquad \text{EQ 2.3}$$

and

$$\tan\omega = \left(\frac{L}{d}\right) \qquad \text{EQ 2.4}$$

by solving for L after solving EQ 2.4 for ω and substituting in EQ 2.3, EQ 2.5 results.

$$L = d\left(\tan 2\left(\sin^{-1}\left(\frac{s_1\lambda}{4\pi}\right)\right)\right) \qquad \text{EQ 2.5}$$

Then we can determine s_2 and s_3 as follows:

$$s_2 = \frac{4\pi}{\lambda} \sin\left(\frac{\tan^{-1}\left(\frac{L}{d+\Delta d}\right)}{2}\right) \qquad \text{EQ 2.6}$$

$$s_3 = \frac{4\pi}{\lambda} \sin\left(\frac{\tan^{-1}\left(\frac{L}{d-\Delta d}\right)}{2}\right) \quad \text{EQ 2.7}$$

The intensity observed for the middle nozzle with its respective s value allows interpolation of the intensity at s_2 from other known points and, using a cubic spline function, results in intensity I_2. A similar step is taken for the contribution from the closest pseudonozzle giving intensity I_3. Therefore the total scattered intensity average contributed from the three nozzles is:

$$I_{tot}(s_1) = \frac{I_1 + aI_2 + bI_3}{1 + a + b} \quad \text{EQ 2.8}$$

The coefficients a and b allow us to study different behaviours of the gaseous flow that might have arisen from the slit nozzle. If all coefficients are equal to one it would mean that an even gas flow is coming from the slit nozzle. Then there would be as much probability of finding a gaseous molecule at the beginning of the nozzle as throughout the rest of the length of the nozzle. If a and b are equal to one another but not equal to 1, a Gaussian gas flow would be expected. Variation of the values of a and b allow the change of the symmetric flow of the Gaussian function at the tip of the nozzle, therefore changing the centre of the highest gas density.

In practice the program uses the same steps for all the pseudonozzles that comprise the new nozzle and for all the diffracted angles for which experimental data on a normal nozzle were collected. Thus the program for even gas flow can be summarised for each s value read from the middle nozzle, when their respective intensities, contributed from all the other nozzles at a specific s value, is:

$$I_{tot}(s) = \int \sum_{dmin}^{dmax} \frac{I(s_d(d,s))}{n} ds \quad \text{EQ 2.9}$$

where d is the distance of each pseudonozzle from the photographic plate and n is the number of pseudonozzles taken into account. The value of n should tend towards infinity, but since the normal nozzle length is of the order of 500 μm, for a nozzle of 5 mm in length, only 10 pseudonozzles are needed to get a similar definition to that of the conventional nozzle. However, in order to avoid any potential overestimation or underestimation in intensity changes, 1000 pseudonozzles were used for all simulations. The full FORTRAN code can be found in Appendix C on the CD.

2.4.2 Expectations from the slit nozzle

The intensities collected from the slit nozzle are expected to produce blurred data with respect to the diffraction from a single point nozzle, the conventional nozzle. In **Figure 2.12**, the effect on the raw intensity collected on a photographic film of increasing the nozzle size is emphasized. The data are exaggerated, and are not representative of either true data or simulation results with a reasonable size nozzle. However, it shows how the data could be blurred with the use of the slit nozzle. The single-point nozzle intensity is the black curve. All the other curves represent the increase of the size of the nozzle and consequently of the zone of diffraction. Gradually from the green to the red curve the variation of amplitudes of vibration is diminished and would eventually result in a straight line if a large enough nozzle had been used.

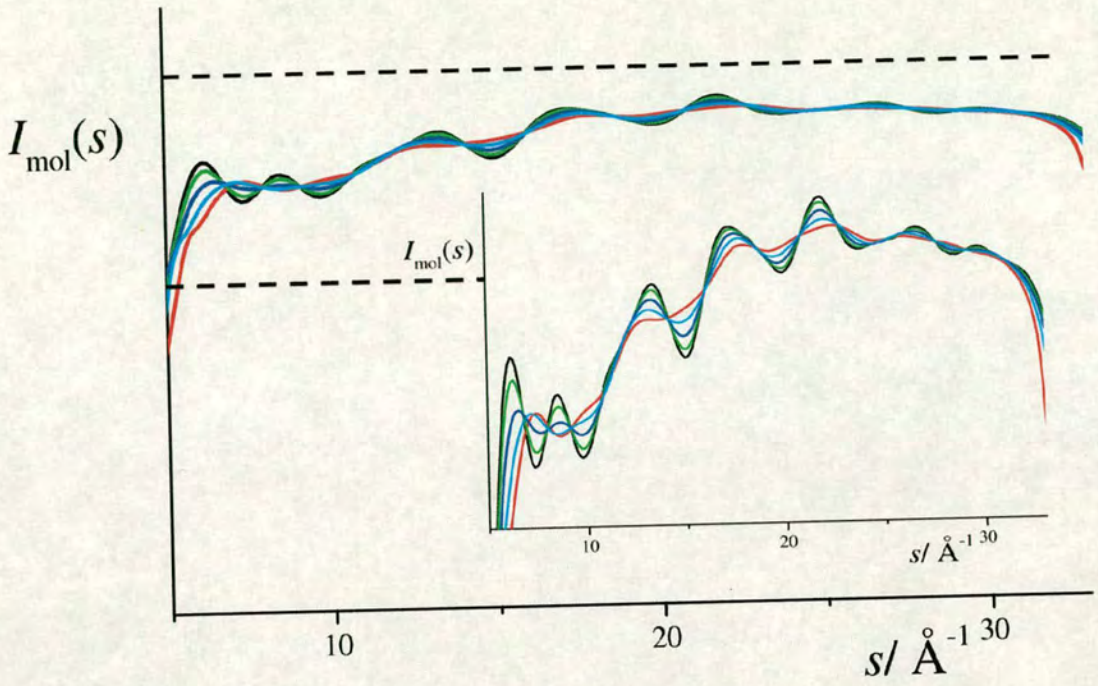

Figure 2.12: Exaggerated effect of the slit nozzles on raw intensity data.

The trend in **Figure 2.12** is directly linked to the behaviour of the amplitudes of vibration as shown in **Figure 2.13**. This picture is also exaggerated to show the potential problem of using a slit nozzle. The longer the slit of the nozzle, the smaller the variations of the curve in **Figure 2.12** and the faster the curve becomes a straight line. This is translated in **Figure 2.13** as a faster loss of information. The light blue curve, representing the longest nozzle, has lost all peaks past s equal to 250 nm^{-1}. This loss of variation increases the amplitude of vibration. Therefore if any parameter changes should be observed while using the slit nozzle, they would be for the amplitudes. The following extensive simulation studies should help us determine if our expectations turn out to be true.

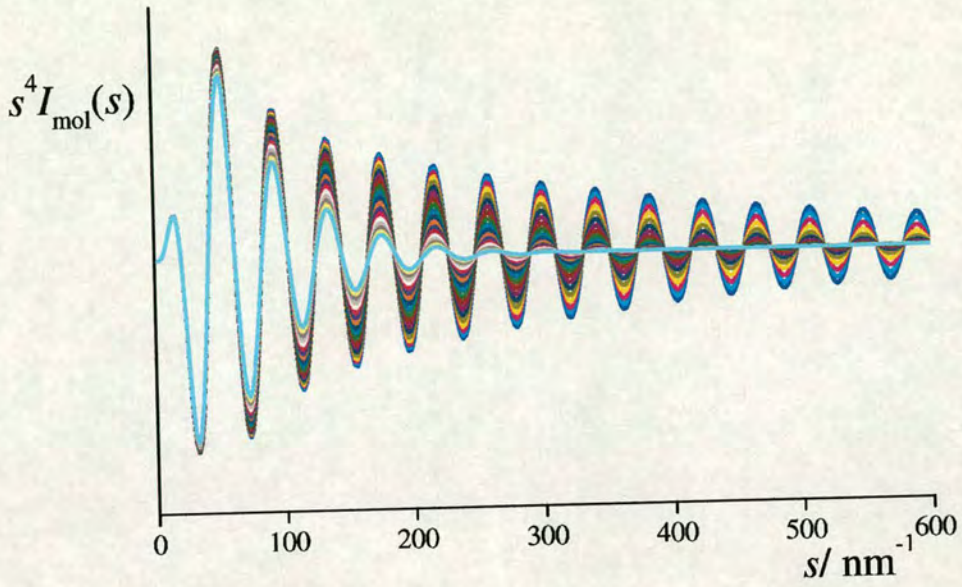

Figure 2.13: Effect of the amplitudes of vibration (u-values) on the intensity curve for a diatomic species.

2.4.3 Benzene simulation results

Some of the simulations carried out with benzene as a reference compound will be presented. The studies were performed by varying the size of the nozzle and the gas flow output and monitoring the effect on the C-C bond distance and the main RMS amplitudes of vibration involved in the description of the aromatic ring. For full and extensive results see appendix C on the CD. No restraints were used during any of the refinements, and in total more than a 100 sets of simulated data were used for the analysis of the potential behaviour of the adoption of the new nozzle. All effects that would be deduced from this study would only be as a function of the nozzle size and gas flow output. Nine nozzles of different sizes were simulated, ranging from the conventional nozzle size, 0.5 mm, to a 10 mm slit. In addition to the variation in size, the gas output flow was varied. Some examples of output flow can be seen in **Figure 2.14**. An even gas flow output is represented by the purple function in **Figure 2.14**, allowing the same probability of finding a gaseous molecule at every point along the nozzle. All other curves are Gaussian functions with different exponents, which, in **Figure 2.14,** are all centred in the middle of the nozzle length. Examples where the

highest probability of finding gaseous molecules were shifted off the centre of the nozzle were also investigated.

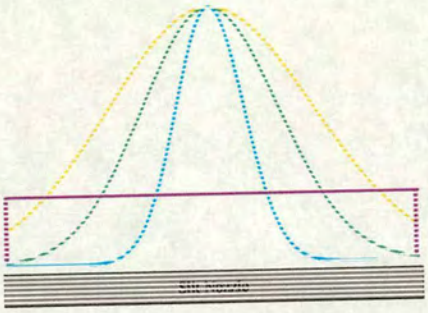

Figure 2.14: Different gas outputs used for the forecast of the diffraction coming from the slit nozzle.

Figure 2.15 shows highlights of the simulation of benzene, with the changes in the C-C distances with respect to gas flow and size of the nozzle. The rest of the results can be found in Appendix C on the CD. Variations of amplitudes of vibration are shown graphically in **Figure 2.16,** and tabulated results can be found in appendix C, in combination with larger graphical representations of the amplitude variations. The amplitudes going in ascending order in **Figure 2.156** (*a*) are C-C, C…C_p, C-H, C…H_o and in (b) C..C_m, C…H_p, C…H_m. In both graphs the standard deviation errors are represented by the vertical error bars.

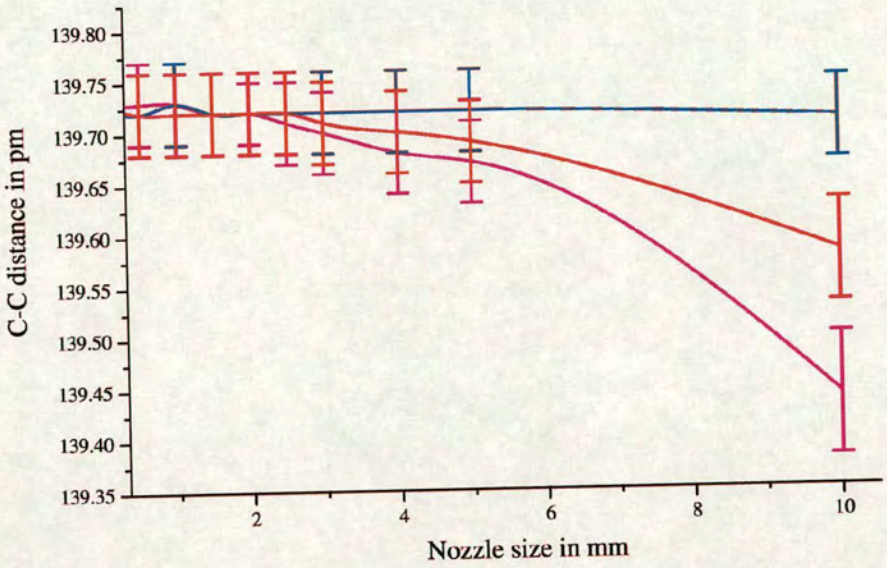

Figure 2.15: C-C distances in benzene as a function of the size of the slit with variation of the gas output. Even gas distribution, Gaussian gas distribution with small coefficient, Gaussian gas distribution with larger coefficient.

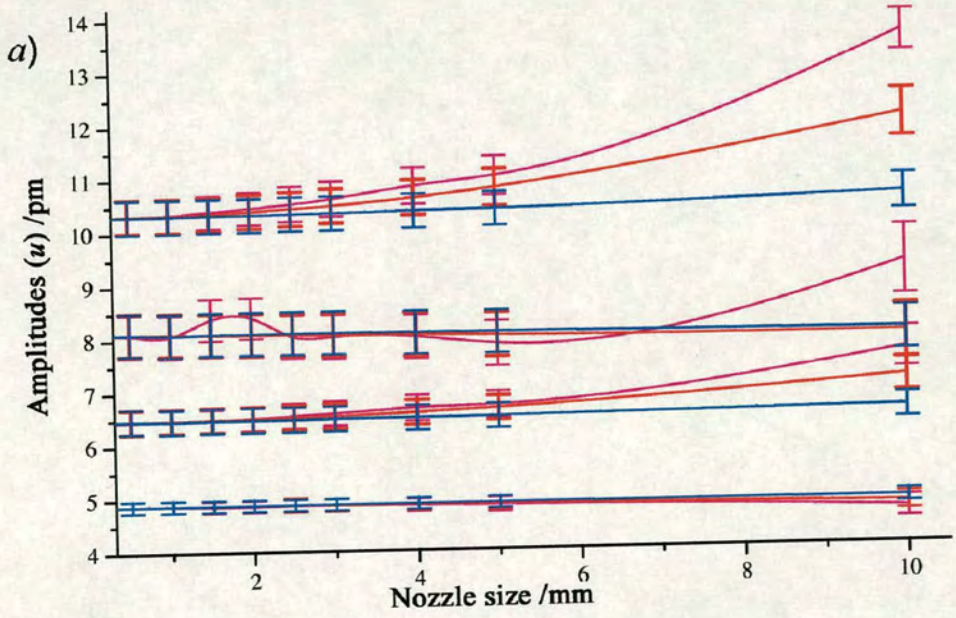

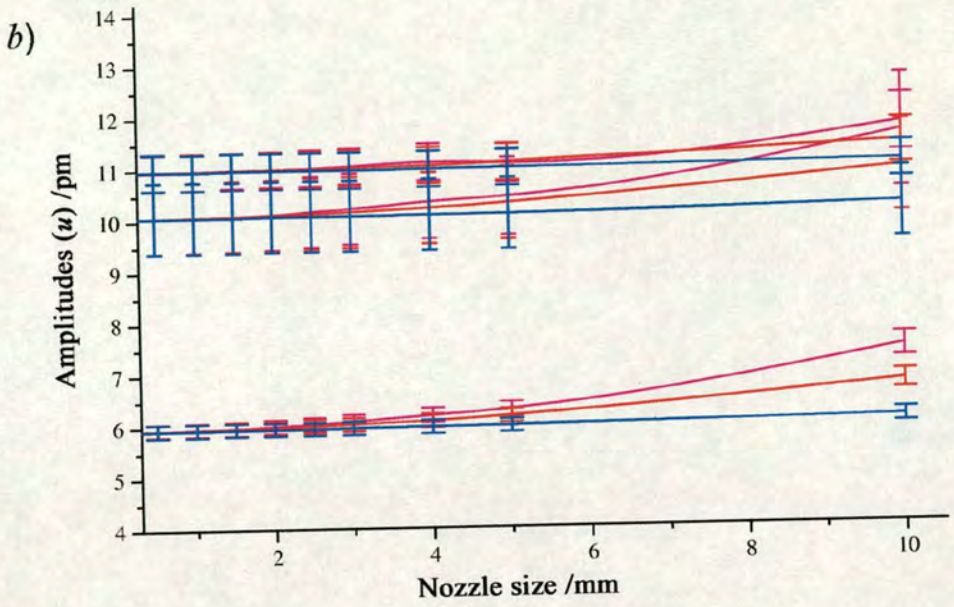

Figure 2.16: *u* amplitude variations in benzene as a function of the size of the slit with respect to change in the gas flow output. Even gas distribution, Gaussian gas distribution with small coefficient, Gaussian gas distribution with larger coefficient. Amplitude definitions can be found in the text, and in appendix C on the CD.

Analysis of the picture involving the C-C distance in benzene shows no changes with respect to the e.s.d. with a slit nozzle up to 5 mm in length. This is independent of the gas distribution. Past this critical length, the C-C bond distance appears to shrink by 0.3 pm with an even gas flow distribution. When assuming a Gaussian gas distribution with a small coefficient (see the yellow curve in **Figure 2.14)**, the aromatic carbon bond distance decreases by 0.15 pm for a nozzle length of 1 cm. For a Gaussian function with a high coefficient (see the blue curve in **Figure 2.14**) the bond length is not affected by the size of the nozzle. This behaviour is due to the fact that the Gaussian function used to represent the probability of gaseous molecules diffracting electrons from the main beam effectively diminishes the size of the nozzle in use. Therefore the area of contact of the gaseous stream and the main electron beam for the blue curve in **Figure 2.15** is smaller than for the magenta curve.

The results for the changes of amplitudes of vibration show that the trend is independent of the gas distribution used. In fact, all amplitudes increase more or less uniformly with respect to increase of the nozzle size. The amplitudes that increase the most are the larger ones which indicates that their definition is lost more quickly than for the smaller ones. Amplitudes are unchanged within one e.s.d up to a length of 3 mm. Past this critical slit length, only the C-C amplitude (the smallest one) does not vary whilst the others follow the predicted trend. The biggest increases are noticed once again when an even distribution is assumed above the nozzle, whereas for the gas output function following the profile of the blue curve in **Figure 2.14** no changes are observed whatever the size of the slit in use.

Therefore our prediction was correct. The amplitudes augment upon increase of the size of the nozzle. However, this effect is extremely dependent on the gas flow profile arising from the slit nozzle. If the gas distribution above the nozzle was revealed to be in the form of a Gaussian function with a small coefficient, the need for a deconvolution program would be obsolete. On the other hand if the behaviour is even throughout the nozzle or close to it, it would be imperative that data, after collection, be deconvoluted with respect to the gaseous output. A gas distribution following the symmetrical Gaussian functions is expected since the inside of the nozzle is perfectly symmetrical, and confirmed by previous studies.

2.5 Experimental results

2.5.1 Conventional vs. slit nozzle

As the extensive simulation carried out showed consistency and conformed to our expectation, true experimental data needed to be collected. Prior to investigation of known molecules using the slit nozzle, the thermodynamic advantage of the adoption of such a nozzle had to be investigated. To have accurate and meaningful comparisons between the conventional and slit nozzle designs, they had to be run under strictly controlled conditions. Therefore a T-shape extension of the room-

temperature nozzle, which allowed both nozzle designs to be in the diffracted chamber at the same time, **Figure 2.17**, was needed.

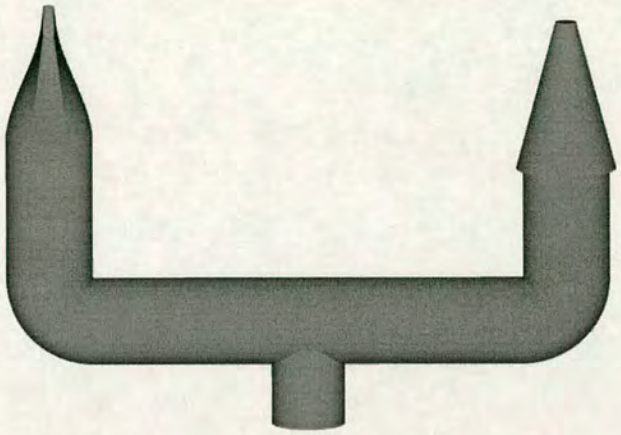

Figure 2.17: Twin nozzle assembly with both slit (left) and conventional (right) nozzles.

The experiment was carried out using benzene at room temperature (24°C). The difference of flux of diffracted electrons was monitored on an electrometer. Both nozzles, placed on the T-shaped splitter, release gaseous molecules inside the diffraction chamber, but only one is placed in contact with the electron beam at any one time. Although the flow was predicted to increase 10-fold under ideal conditions, it was found to be five and a half times greater using the slit nozzle than with the conventional nozzle. At 1°C, the slit nozzle permits a similar number of gaseous benzene molecules to diffract electrons as when the conventional nozzle is in use at room temperature. Therefore the adoption of such design fulfilled its thermodynamic role by allowing experiments to be carried out at a temperature 20°C lower than would have been necessary using conventional nozzles.

2.5.2 Gas-phase electron diffraction structure, experimental

Three simple molecules were studied using the slit nozzle: benzene, carbon dioxide and acetone. They are all compared to their structures obtained with the conventional nozzle. Benzene (99.7%), acetone (99.5%) and carbon dioxide (dry ice), were obtained from Aldrich. The samples were used without any further purification.

GED data for the three simple molecules were collected at two different camera distances using the Edinburgh apparatus. The data were recorded photographically on Kodak Electron Image films. Two plates from each distance were studied for benzene with both the conventional and slit nozzles, while three plates at short and two at long distances were collected for carbon dioxide for both nozzles. Finally two at short and three at long, two at long and three at short distances, respectively, for the conventional and slit nozzle for acetone were recorded. The electron-scattering patterns were converted into digital form using an Epson Expression 1600 Pro flatbed scanner with a scanning program as described elsewhere.[11] Electron wavelengths were determined from the scattering pattern of benzene vapour recorded immediately after each sample molecule run. The weighting points for the off-diagonal weight matrices, correlation parameters, and scale factors for the two camera distances are given in **Table 2.1**, **Table 2.2** and **Table 2.3**. The data reduction and analysis were performed using the standard program *ed@ed*, [12] employing the scattering factors of Ross *et al.*[13]

One, two and seven geometric parameters were used to describe the structures of benzene, carbon dioxide and acetone, respectively, following the numbering schemes in **Figure 2.18**, for the refinement procedure. All parameters are self explanatory assuming the appropriate symmetry of each structure (**Table 2.4**, **Table 2.5** and **Table 2.6**).

Except for benzene, for which the r_a structure was refined, the starting parameters for the r_{h1} refinements were taken from the theoretical geometry optimised at the MP2/6-311G(d,p). For both compounds theoretical Cartesian force fields were obtained at MP2/6-311G(d,p) and converted into force fields described by sets of symmetry coordinates using the program SHRINK.[14]

Table 2.1: GED data analysis parameters for benzene with both conventional nozzle and slit nozzle.

	Conventional nozzle		Slit nozzle	
camera distance/mm	285.72	128.37	2857.72	128.14
T_{sample}/K	293	293	293	293
T_{nozzle}/K	293	293	293	293
Δs /nm^{-1}	2	4	2	4
s_{min}/nm^{-1}	20	60	20	60
sw_1/nm^{-1}	40	80	40	80
sw_2/nm^{-1}	110	256	110	256
s_{max}/nm^{-1}	128	300	128	300
correlation parameter	0.4842	0.4087	0.4807	0.4422
scale factor, k_a	0.796(6)	0.580(9)	0.810(4)	0.607(9)
electron wavelength /pm	6.02	6.02	6.02	6.02
a	1	2	1	2

Table 2.2: GED data analysis parameters for carbon dioxide with both conventional nozzle and slit nozzle.

	Conventional nozzle		Slit nozzle	
camera distance/mm	285.72	128.37	285.97	128.20
T_{sample}/K	53	73	53	73
T_{nozzle}/K	293	293	293	293
Δs /nm^{-1}	2	4	2	4
s_{min}/nm^{-1}	20	60	20	60
sw_1/nm^{-1}	40	80	40	80
sw_2/nm^{-1}	110	256	118	256
s_{max}/nm^{-1}	128	300	138	300
correlation parameter	0.4959	0.4266	0.4916	0.3947
scale factor, k_a	0.800(12)	0.599(13)	0.814(10)	0.788(11)
electron wavelength /pm	6.02	6.02	6.02	6.02
a	1	2	1	2

Table 2.3: GED data analysis parameters for acetone with both conventional nozzle and slit nozzle.

	Conventional nozzle		Slit nozzle	
camera distance/mm	285.89	128.33	285.72	128.72
T_{sample}/K	170	170	170	170
T_{nozzle}/K	293	293	293	293
Δs /nm^{-1}	2	4	2	4
s_{min}/nm^{-1}	20	72	20	72
sw_1/nm^{-1}	40	92	40	92
sw_2/nm^{-1}	118	276	118	284
s_{max}/nm^{-1}	138	320	138	320
correlation parameter	0.4645	0.2194	0.406	0.1866
scale factor, k_a	0.7105(8)	0.598(17)	0.787(4)	0.640(14)
electron wavelength /pm	6.02	6.02	6.02	6.02
a	1	2	1	2

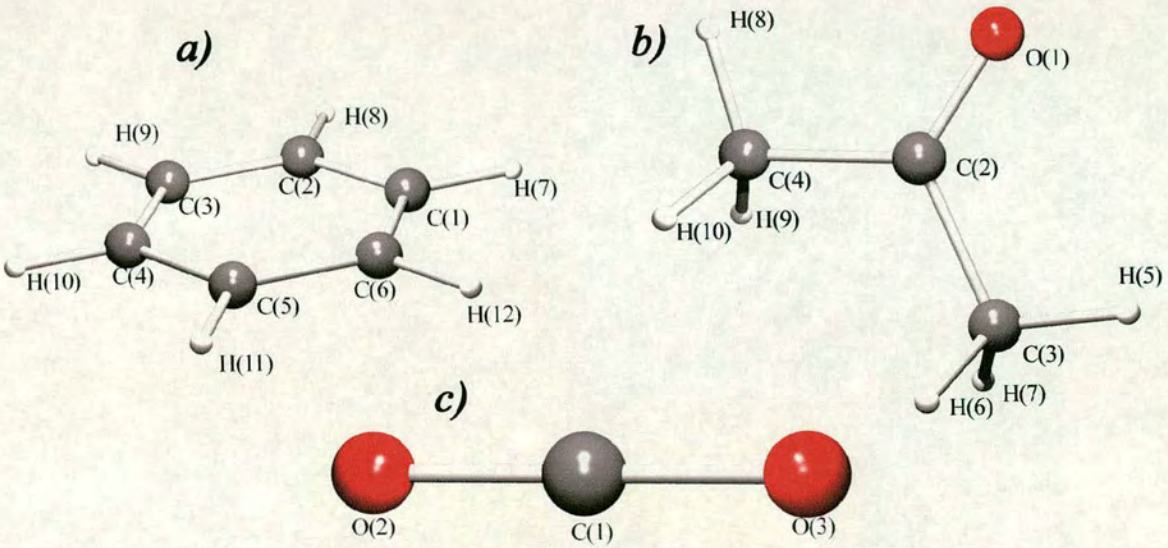

Figure 2.18: Molecular frameworks for (*a*) benzene, (*b*) acetone and (*c*) carbon dioxide.

2.6 **Results**

The models used for the GED refinements of benzene, carbon dioxide and acetone were based upon the geometries obtained from the optimised *ab initio* calculations. Four different refinements were carried out for each of the three molecules, one each for the conventional nozzle (CV), the simulated slit nozzle gaussian type flow (SG), the simulated slit nozzle even type flow (SE) and finally the "true" slit nozzle (S). The least-squares refinements of the structure of benzene resulted in R_G factors of 0.055 (R_D = 0.032) [CV], 0.055 (R_D = 0.032) [SG], 0.055 (R_D = 0.032) [SE] and 0.051 (R_D = 0.030) [S], with optimized parameters and amplitudes of vibration listed in **Table 2.4**. The least-squares refinements of the structure of carbon dioxide resulted in R_G factors of 0.102 (R_D = 0.058) [CV], 0.104 (R_D = 0.062) [SG], 0.099 (R_D = 0.057) [SE] and 0.073 (R_D = 0.041) [S], with optimized parameters and amplitudes of vibration listed in **Table 2.5**. The least-squares refinements of the structure of acetone resulted in R_G factors of 0.061 (R_D = 0.036) [CV], 0.043 (R_D = 0.031) [SG], 0.050 (R_D = 0.037) [SE] and 0.045 (R_D = 0.027) [S], with optimized parameters and amplitudes of vibration listed in **Table 2.6**. For full lists of the final bond distances, amplitudes of vibration and correlation matrices, see appendix C on the CD. The success of the final refinements can be assessed on the basis of the molecular scattering curves, **Figure 2.19**, **Figure 2.21** and **Figure 2.23**, and radial distribution curves **Figure 2.20**, **Figure 2.22** and **Figure 2.24,** for benzene, carbon dioxide and acetone respectively. For all these graphical representations, CV, SG, SE and S are the green, red, magenta and black curves, respectively.

Table 2.4: Geometrical parameters[a] and amplitudes of vibration (u/pm) obtained in the GED refinements for benzene.

	Benzene	Conventional nozzle	Simulated slit nozzle gaussian type flow	Simulated slit nozzle even type flow	slit nozzle
	Parameter	r_a	r_a	r_a	r_a
p_1	rC-C	139.69(4)	139.68(4)	139.61(4)	139.64(4)
	atom pair	Amplitude	Amplitude	Amplitude	Amplitude
u_1	C(1) - C(2)	4.5(1)	4.5(1)	4.7(1)	4.2(1)
u_2	C(1) - H(7)	8.9(4)	8.9(4)	9.1(5)	9.1(5)
u_3	C(1) ... C(3)	6.2(1)	6.3(1)	6.7(1)	5.8(1)
u_4	C(1) ... C(4)	7.0(3)	7.1(3)	7.7(3)	6.3(2)
u_5	C(1) ... H(8)	10.9(4)	10.9(4)	11.3(4)	11.1(4)
u_6	C(1) ... H(9)	10.6(4)	10.7(4)	11.1(4)	10.8(4)
u_7	C(1) ... H(10)	10.3(8)	10.5(8)	11.2(8)	10.3(8)

[a] distances in pm

Table 2.5: Geometrical parameters[a] and amplitudes of vibration (u/pm) obtained in the GED refinements for carbon dioxide.

	Carbon dioxide	Conventional nozzle	Simulated slit nozzle gaussian type flow	Simulated slit nozzle even type flow	Slit nozzle
	Parameter	r_{h1}	r_{h1}	r_{h1}	r_{h1}
p_1	rC(1)O	116.56(7)	116.41(7)	116.54(7)	116.38(5)
p_2	∠O(3)C(1)O(2)	180.00(8)	180.00(8)	180.00(8)	180.00(7)
	atom pair	Amplitude	Amplitude	Amplitude	Amplitude
u_1	C(1) - O(2)	3.6(2)	3.6(2)	3.8(2)	3.5(1)
u_2	O(2) ... O(3)	5.3(3)	5.3(3)	6.0(3)	5.3(2)

[a] distances in pm, angles in °

Table 2.6: Geometrical parameters[a] and amplitudes of vibration (u/pm) obtained in the GED refinements for acetone.

	Acetone	Conventional nozzle	Simulated slit nozzle gaussian type flow	Simulated slit nozzle even type flow	Slit nozzle
	Parameter	r_{h1}	r_{h1}	r_{h1}	r_{h1}
p_1	rO(1)C(2)	122.7(2)	121.1(2)	120.7(2)	121.0(1)
p_2	rC(2)C(3)	151.32(9)	151.55(10)	151.54(10)	151.44(7)
p_3	rC(3)H(6)	112.5(2)	111.4(2)	110.4(3)	111.1(2)
p_5	∠O(1)C(2)C(3)	121.3(1)	121.7(2)	122.0(3)	121.78(9)
p_6	∠C(2)C(3)H(5)	107.6(17)	108.1(13)	106.2(13)	108.5(10)
p_7	∠C(2)C(3)H(6)	109.1(8)	108.7(7)	108.9(6)	108.2(5)
p_8	∠H(5)C(3)H(6)	110.1(10)	110.2(10)	109.9(9)	110.4(9)
	atom pair	Amplitude	Amplitude	Amplitude	Amplitude
u_1	O(1) - C(2)	3.0(4)	4.1(2)	4.4(2)	4.0(2)
u_2	C(2) - C(3)	4.9(2)	4.7(2)	4.7(2)	5.1(1)
u_3	C(3) - H(5)	5.5(4)	8.9(4)	10.7(4)	8.6(3)
u_5	O(1) ... C(3)	5.6(2)	5.8(2)	6.3(3)	6.1(1)
u_7	O(1) ... H(5)	18.0(66)	13.5(52)	13.8(91)	16.3(22)
u_{11}	O(1) ... H(9)	17.7(11)	17.9(11)	17.7(14)	18.2(8)
u_{17}	C(2) ... H(9)	11.2(5)	9.5(5)	9.8(8)	10.3(3)
u_{19}	C(3) ... C(4)	6.4(5)	7.3(9)	7.2(12)	6.7(4)
u_{21}	C(3) ... H(9)	21.3(49)	21.4(41)	18.4(40)	27.6(30)

[a] distances in pm, angles in °

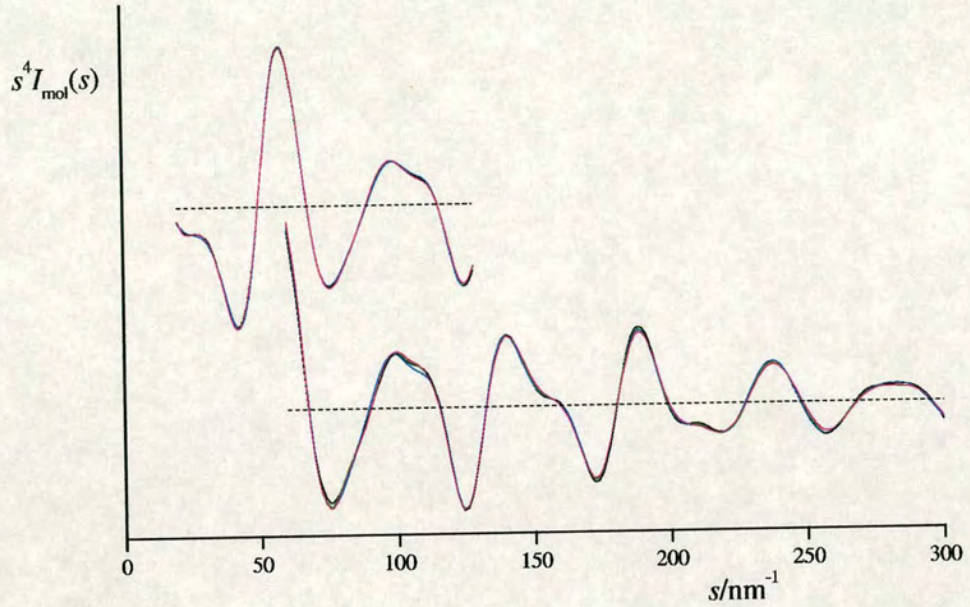

Figure 2.19: Experimental and final weighted difference (experimental - theoretical) molecular scattering intensities for benzene. (SE, CV, SG, S)

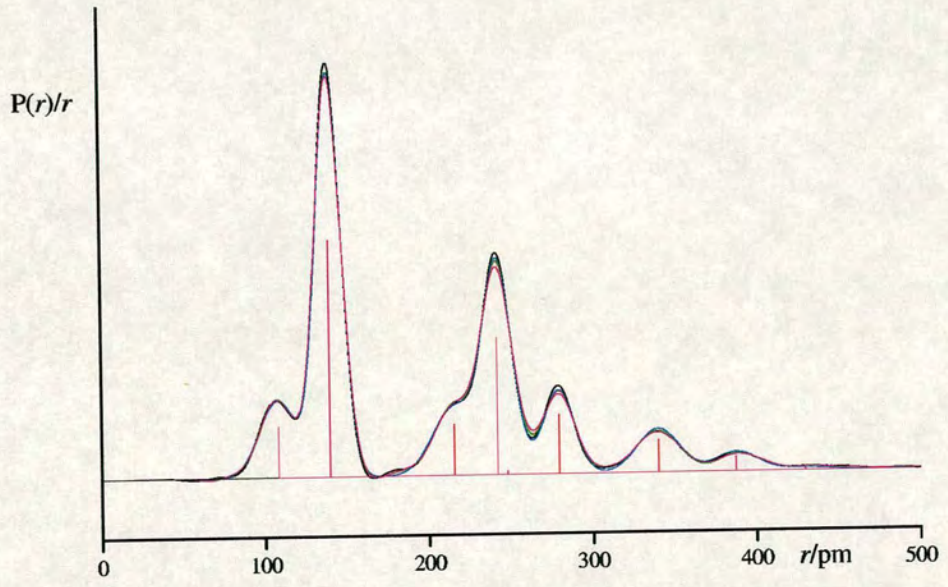

Figure 2.20: Experimental and difference (experimental – theoretical) radial distribution curves, $P(r)/r$, for benzene. Before Fourier inversion, the data were multiplied by $s.\exp(-0.00002s^2)/(Z_C\text{-}f_C)(Z_C\text{-}f_C)$. (SE, CV, SG, S)

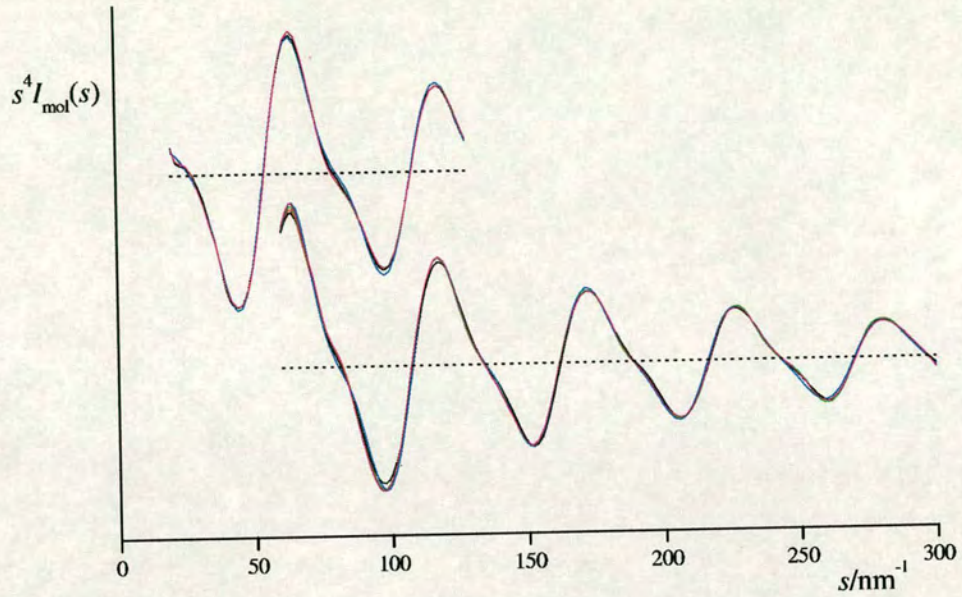

Figure 2.21: Experimental and final weighted difference (experimental - theoretical) molecular scattering intensities for carbon dioxide. (SE, CV, SG, S)

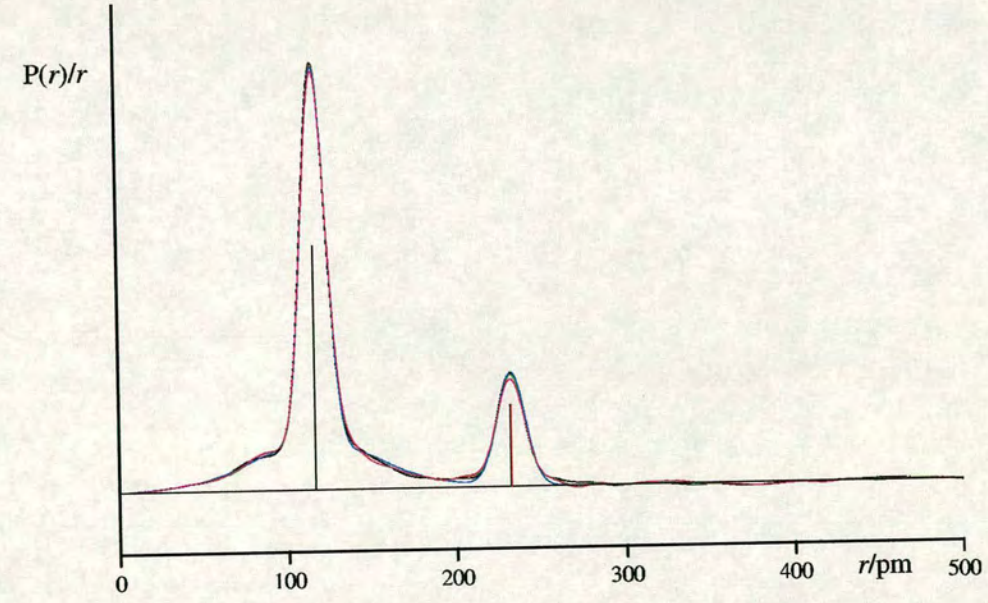

Figure 2.22: Experimental and difference (experimental – theoretical) radial distribution curves, $P(r)/r$, for carbon dioxide. Before Fourier inversion, the data were multiplied by $s.\exp(-0.00002s^2)/(Z_C\text{-}f_C)(Z_O\text{-}f_O)$. (SE, CV, SG, S)

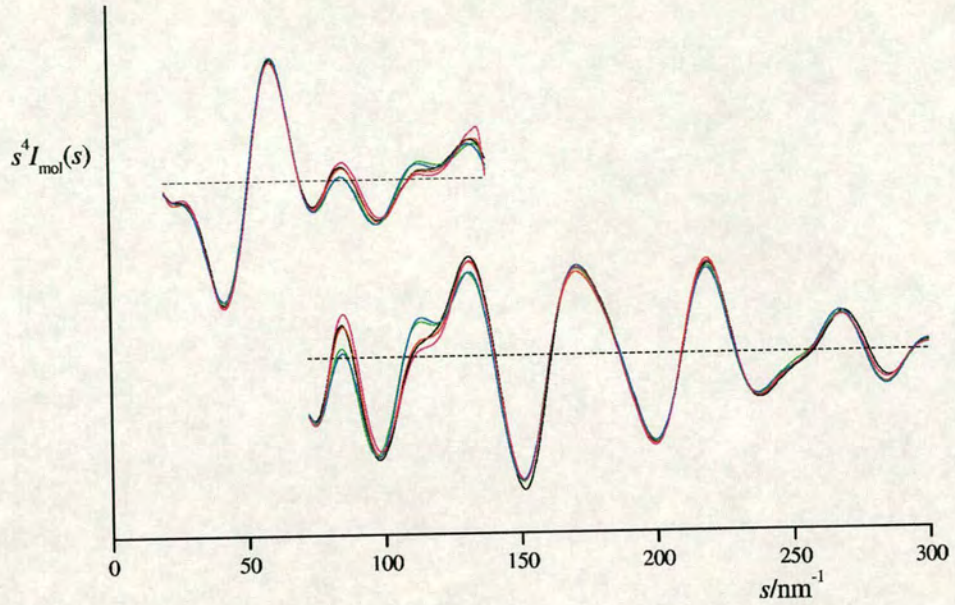

Figure 2.23: Experimental and final weighted difference (experimental - theoretical) molecular scattering intensities for acetone. (SE, CV, SG, S)

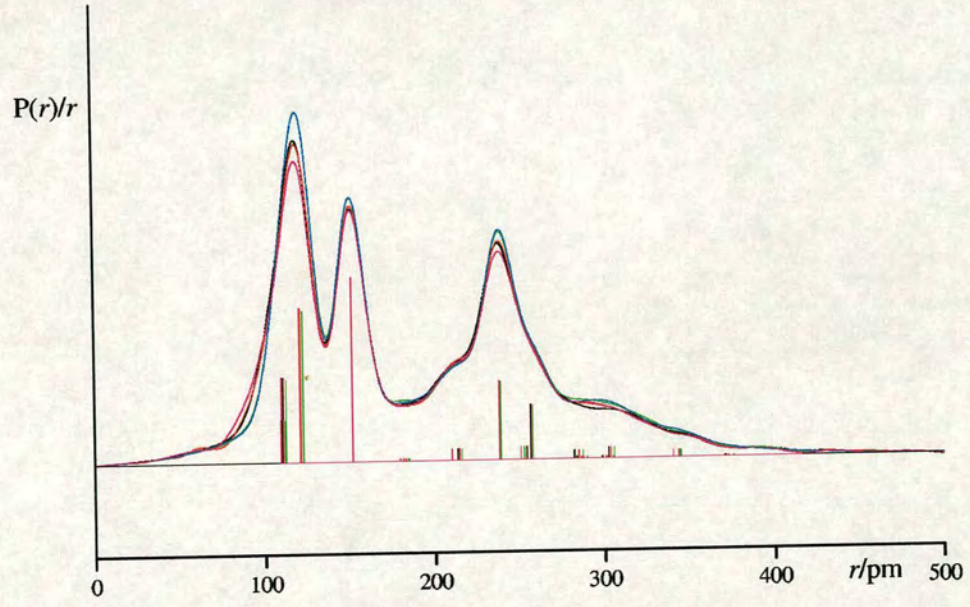

Figure 2.24: Experimental and difference (experimental – theoretical) radial distribution curves, $P(r)/r$, for acetone. Before Fourier inversion, the data were multiplied by $s.\exp(-0.00002s^2)/(Z_C\text{-}f_C)(Z_O\text{-}f_O)$. (SE, CV, SG, S)

2.7 Discussion

The nozzle simulations were carried out assuming a slit nozzle of 5 mm in length, by the methodology described previously. The results of two types of gas distributions, the even and Gaussian gas output flows, are presented.

Looking at the differences in amplitudes and parameters with respect to the nozzle used, for bezene no major differences are observed. The C-C parameter is unchanged within one e.s.d, except in the case of SE, for which the aromatic carbon bond has shrunk by two e.s.ds.. Even though the predicted trend (the increase of amplitude with use of a slit nozzle) is observable the changes are all within one e.s.d..

In the case of carbon dioxide, the C=O distance does shrink by 0.18 pm from CV to S. This effect is well reproduced by SG. The amplitudes, however, are unchanged going from CV to S via SG. As expected, SE has slightly bigger amplitudes, characterised by O(2)…O(3), which is two e.s.ds. greater.

For acetone, p_1 shows the biggest difference observed so far between CV and S, as C=O is 1.7 pm longer using the conventional nozzle. It is important to note that it is the only parameter that shows a difference of more than one e.s.d. with respect to all other nozzles. The structure of acetone published in the seventies by Iijima Takao revealed a C=O distance of 121.0(4) pm. As a consequence, it can be hypothesized that this bond distance for CV introduces an amplitude that would be slightly erroneous. This could be explained by the very small amplitude associated with that distance. All other amplitudes show the previously observed and expected trends.

Multiple Gaussian coefficients were used for SG before choosing the one in use for direct comparison to the "true" slit nozzle in this section. The different refinement structures with other coefficients were all compared to the one produced by the slit nozzle. For all three small molecules the best agreement was achieved with the one describing SG. The perfect agreement is confirmed graphically through the published radial distribution and molecular intensity curves for all three molecules. For most

curves differentiation is rather challenging to do visually. In the radial distribution curves for benzene and carbon dioxide (**Figure 2.20** and **Figure 2.22**) the highest peaks are always those drawn in black and red, which implies that the amplitudes are the smallest for SG and S. The strong agreement between SG and S is emphasized in the acetone curves. In fact, the curves representing SG and S are almost indistinguishable in both **Figure 2.23** and **Figure 2.24**, whereas CV and SE can be distinguished. The highest difference between all the curves is observable at s 120 nm^{-1} in **Figure 2.23**. While the CV curve shows a hump within this region, it has diminished for both SG and S, and is almost non-existent in SE.

There is a major difference between the two nozzles that became obvious once the first experiment was carried out. This difference is due to the geometry of the slit nozzle. As can be seen in **Figure 2.25**, the films collected at short distances show a lighter region at the bottom of the photographic films, unlike those obtained when the conventional nozzle is used. The explanation for this difference is shown by **Figure 2.26**. Large angle diffracted electrons, which would have been observed on the photographic plate for the conventional nozzle, will be blocked by the nozzle. For every refinement this zone was subtracted as differences in structure were observed when the entire plate was used. Therefore in the future the average of data information would have to be carried out for short camera distance films without this region of the films. This loss is insignificant, since thousand of points are still available to determine the average structure.If the slit nozzle was shaped to avoid the obstruction of the diffracted electrons, it would affect the gas flow and consequently the prediction of the gas distribution would be really difficult. Therefore any structural information extraction would be challenging. The advantage of the slit nozzle is its symmetry, which reduces the number of variables to be taken into account while refining a structure.

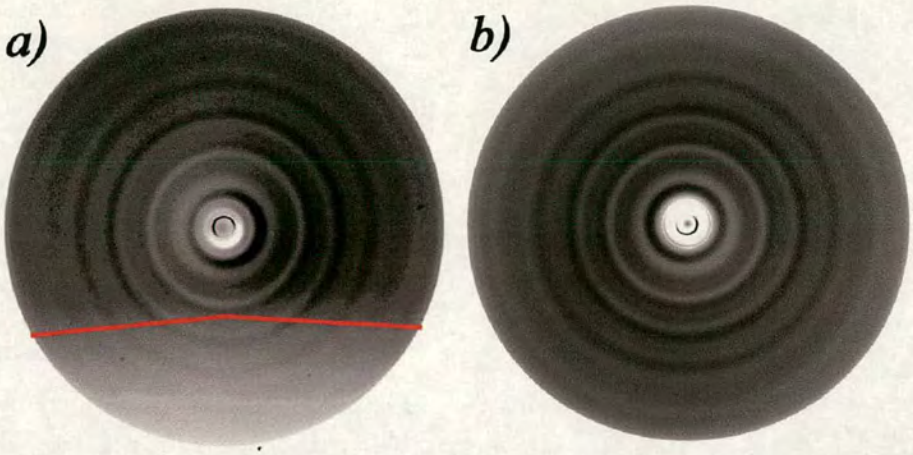

Figure 2.25: Effect on the photographic plates *a*) slit nozzle, b) conventional nozzle.

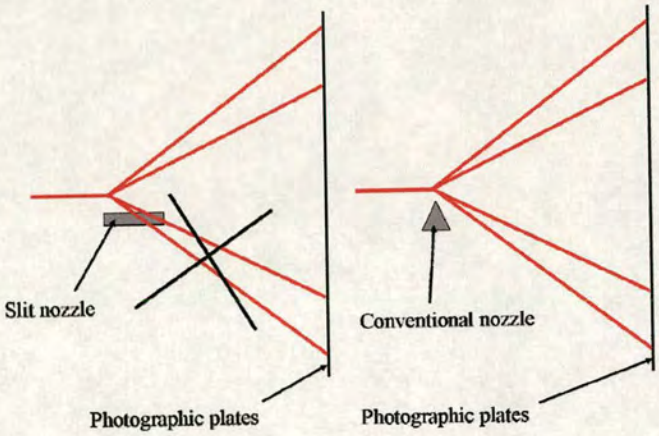

Figure 2.26: Explanation for the presence of a shadow when the slit nozzle is in used at short distances.

The conclusion that can be drawn from the investigation of the three molecules is that, although there are changes observed, these are not significant enough to affect the results dramatically and result in erroneous refined structures. However, the code developed to simulate the electrons being diffracted by gaseous molecules from the slit nozzle can be included in the refinement program. Then the refinement will be carried out assuming the geometry of the nozzle being used, and so the theoretical method will be able to compensate for the small deviations. The use of the code is recommended for the study of floppy molecules, which have low frequency

vibrational modes of less than 100 cm^{-1}. It is better to use raw data from the slit nozzle and adapt the refinement method to the new shape of the nozzle, than to deconvolute the experimental data prior to refinement. In fact, in this last case random noise would be propagated as true structural information and therefore we are more likely to get erroneous structures.

The slit nozzle codes have also been adapted for the study of nozzles with circular openings, and therefore larger orifices could be used and their behaviour predicted. This code can be found in appendix C on the CD. As seen in **Figure 2.27**, the conventional nozzle is split in many "single-point nozzles" as the slit nozzle was. The lozenges delimit the circle while the crosses, which are evenly spaced in the plane of the circle, facilitate the integration of the contribution of each sample point on the circular plane of a round orifice-nozzle.

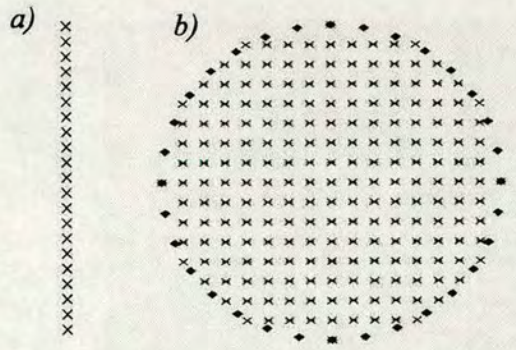

Figure 2.27: Composition of the slit nozzle (a) and conventional nozzle (b) in use in simulation code.

The use of a slit nozzle has successfully helped refine the structure while increasing the contact between the gaseous molecules and the electron beam. The thermodynamic advantage has also been demonstrated by the fact that a good vapour pressure can be expected at a temperature 20°C lower than with the conventional nozzle.

2.8 **References**

1 A. J. Blake, P. T. Brain, H. McNab, J. Miller, C. A. Morrison, S. Parsons, D. W. H. Rankin, H. E. Robertson, B. A. Smart, *J. Phys. Chem.*, 1996, **100**, 12280; P. T. Brain, C. A. Morrison, S. Parsons, D. W. H. Rankin, *J. Chem. Soc., Dalton Trans.*, 1996, 4589; N. W. Mitzel, D. W. H. Rankin, *J. Chem. Soc., Dalton Trans.*, 2003, 3650.

2 S. L. Hinchley, M. F. Haddow, D. W. H. Rankin, *Dalton Trans.*, 2004, 384.

3 I. Hargittai, J. Tremmel, M. Kolonits, *Hung. Sci. Instrum.*, 1980, **50**, 31.

4 S. H. Bauer, T. Ino, R. F. Porter, *J. Chem. Phys.*, 1960, **33**, 685.

5 J. Tremmel, I. Hargittai, *Hung. Sci. Instrum.*, 1980, **50**, 43.

6 I. Hargittai, J. Tremmel, G. Schultz, *J. Mol. Struct.*, 1975, **26**, 116.

7 R. B. Harvey, F. A. Keidel, S. H. Bauer, *J. Appl. Phys.*, 1950, **21**, 860.

8 A. Haaland, *personal communication.*

9 H. Oberhammer, *personal communication.*

10 Y. Morino, Y. Murata, *Bull. Chem. Soc. Jpn.*, 1965, **38**, 114.

11 J. R. Lewis, R. J. Mawhorter, S. L. Hinchley, D. W. H. Rankin, *manuscript in preparation.*

12 S. L. Hinchley, H. E. Robertson, K. B. Borisenko, A. R. Turner, B. F. Johnston, D. W. H. Rankin, M. Ahmadian, J. N. Jones, A. H. Cowley, *Dalton Trans.*, 2004, 2469.

13 A. W. Ross, M. Fink, R. Hilderbrandt, *International Tables for Crystallography*; Wilson, A. J. C., Ed.; Kluwer Academic Publishers: Dordrecht, The Netherlands, 1992; Vol. C, 245.

14 V. A. Sipachev, *J. Mol. Struct.*, 1985, **121**, 143.

15 I. Takao, *Bull. Chem. Soc. Jpn.*, 1972, **45**, 3526.

Chapter 3

The reservoir

3.1 **Introduction**

As seen in the previous chapter, thanks to the development of the new refinement methodologies such as SARACEN[1] and more recently DYNAMITE,[2] the investigation of larger molecules is now feasible. The introduction of the slit nozzle revealed that collection of data for molecules with lower vapour pressure is feasible without any uncorrectable loss of information. However, some compounds present adequate vapour pressures but with vaporisation rates not sufficiently high for the experiment. Therefore addition of a reservoir will sustain an appropriate flow of gaseous molecules. This reservoir design, to be used with electron diffraction, has the potential to be applied to other gaseous spectroscopic methods such as microwave and photoelectron spectroscopies.

In many laboratories, regardless of the spectroscopic methods, the sample chambers have at most a volume of 2 cm^3 to contain the gaseous molecule at high temperature. Experience in electron diffraction and photoelectron spectroscopy has resulted in what has been accepted as a common design for a heating chamber when gaseous molecules are required. As seen in the previous chapter for the nozzle, the tip of the nozzle and the heating chamber have to be close to one another. In all cases the chamber is made of a stainless steel (or other alloy) block in which one or two solid rods (used as resistances) are enclaved. In Edinburgh, as stated in the previous chapter, the sample is heated outside by a stream of hot air and brought to the nozzle by a steady increase of temperature. The samples are set in a small glass vial, of 2 cm^3 volume, and heated by electric tapes, adapted to the shape of the container. It is this set-up that the reservoir was designed for.

3.2 **Reservoir description**

A volume of 500 ml was estimated to be sufficient to contain enough gaseous molecules for the exposure of one film during one GED experiment. This volume was chosen as a midpoint, but a larger flask could be designed and integrated into the

apparatus in the future. Two reservoir designs were chosen, with different purposes. The reservoir shown in **Figure 3.1 (*a*)** contains all the compound molecules to be analyzed from the very start of the experiment, with the solid or liquid sitting at the bottom of the flask. In contrast, the reservoir illustrated in **Figure 3.1 (*b*)** will be used as a holding chamber, collecting the gaseous molecules vaporized from a sample vessel attached to the bottom entrance, and maintaining them as such at an adequate temperature.

Figure 3.1: (*a*) Reservoir containing the compound from the beginning of the experiment, **(b)** reservoir used as an intermediate chamber.

Both reservoirs are made of Pyrex and have an internal volume of 500 ml, and the inner vessel is completely surrounded by an outer jacket as for water condensers. In our case, however, hot air circulates between the inner jacket and the outer jacket (the external membrane). The hot air is introduced by the use of a converted flameless torch, also referred to as an inline heater. To avoid loss of heat the reservoirs are coated with a 1 cm insulating *Superwool* Blanket. In order to protect against possible implosion and to provide rigidity for the entire system, a stainless steel shield is placed around the set up, as shown in **Figure 3.2**.

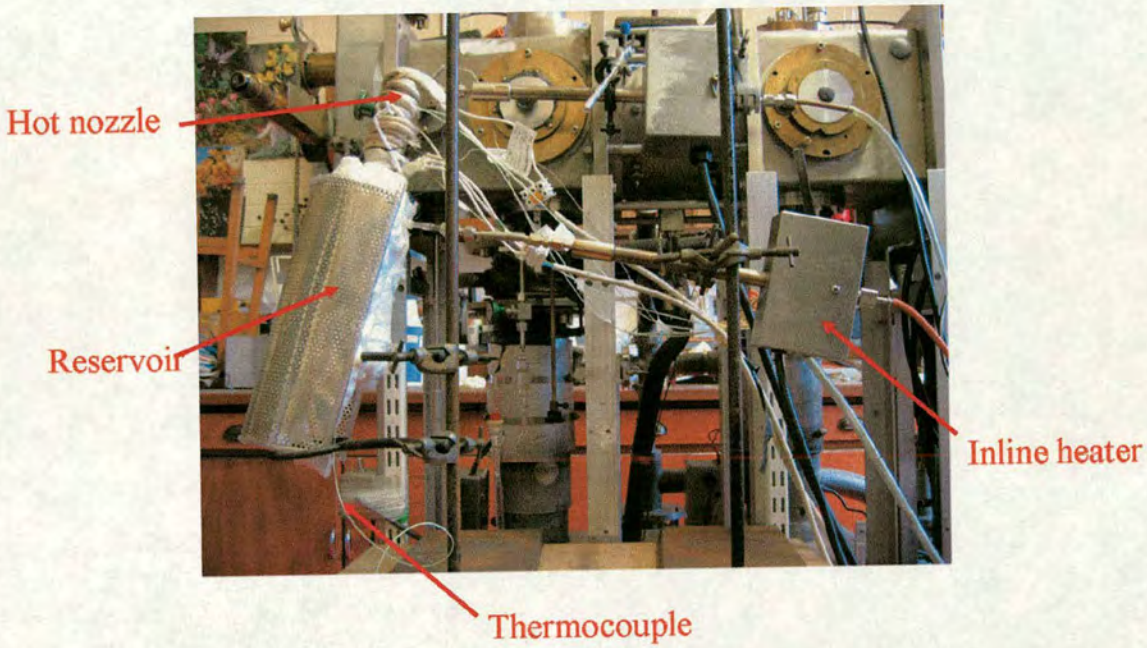

Figure 3.2: Reservoir set-up

The connection between the reservoir and the GED apparatus is made of a glass-to-metal seal, Covar/Pyrex, while the hot air inlet and outlet are glass. The inline heater is connected by a glass fitting mounted onto a stainless steel flexible bearing as seen in **Figure 3.3**, diminishing the physical constraints encountered in previous designs, for which the rigid connection between the flameless torch and the reservoir did not allow any degree of freedom. In previous designs, the reservoir was directly connected to the high temperature nozzle via the use of a "swagelock" seal, which

proved unsuitable. In fact the torque that was applied on the glass/metal seal to avoid any leak was too great and resulted in the breaking of many reservoirs through a straight cut just under the seal. Since the maximum temperature that could be reached by the high temperature nozzle in the present design is 200°C, the introduction of an intermediate non-metal seal connection from *Swagelock* was made. The *Ultra-Torr Vacuum* fitting is done via a finger-tight seal. The O-ring used is VITON made to handle temperatures up to 204°C. This connection of tube to tube is itself heated by a heating tape.

Figure 3.3: Flexible connection reservoir/inline heater

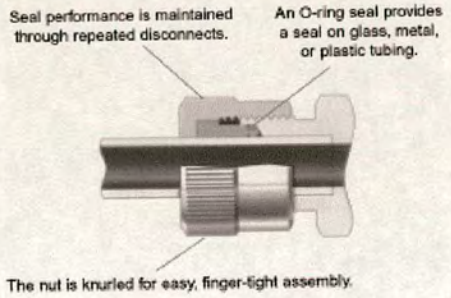

Figure 3.4: Ultra-Torr vacuum fitting[3]

The flameless torch consists of a serpenting heating element made of a ferrous alloy coil wound on a ceramic core, housed in a ceramic tube. The element is then secured into a stainless steel pipe. The chosen design of inline heater allows the heating of 150 psi of air up to 760°C. The backing pressure is supplied by an air compressor. The air flow is regulated just before introduction to the flameless torch by the use of a diffusion valve as seen in the set-up, **Figure 3.2**. To regulate the temperature, the inline heater is connected to a digital thermometer internally connected to an on-off controller as seen in **Figure 3.5**. The entire assembly was custom designed and built. The temperature is sampled continuously by the use of a "K" thermocouple placed at the air exit of the reservoir.

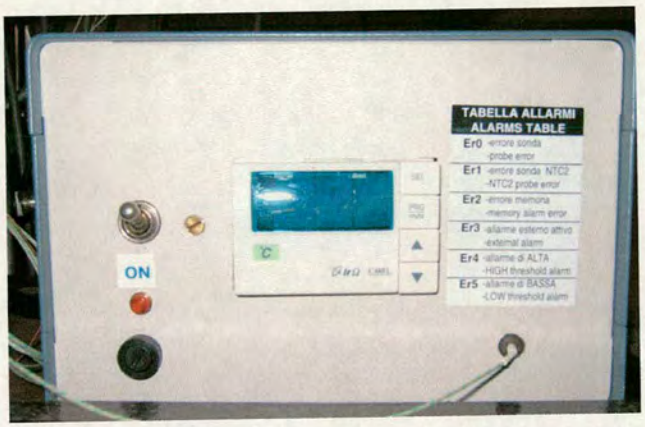

Figure 3.5: Thermometer/power-controller for inline heater

3.3 Experimental

The goal is to ensure a constant flow of gaseous molecules and not a burst of gas, as observed previously with the conventional heating system. To make sure the reservoir fulfilled this requirement, experiments were carried out with 1,2,4,5-tetrachlorobenzene. The total number of electrons diffracted by the gaseous molecules was monitored as a function of time of exposure, waiting time, and temperature at which it was carried out, for both the reservoir and the conventional system. The tetrachlorobenzene was chosen because of its vapour pressure. Previous electron diffraction experiments had revealed that a temperature of 160°C was sufficient to collect structural information for this aromatic tetra-halo-substituted ring.

The experimental set-up was identical to that used for the original collection of high temperature data, with the exception of the absence of photographic plates. We have measured the number of electrons being diffracted by the flow of gaseous molecules streaming out of the high temperature nozzle. It is referred to as the electron count. For both the conventional vessel and the new reservoir the temperature was varied and the time required building up backing pressure, the waiting time, which will be measured in minutes. The number of electrons being diffracted was monitored with

respect to time of exposure, started as soon as a beam of gas was crossing the path of the electron beam. The collected data are summarized in **Table 3.1** and **Table 3.2**. Trends shown by the data in these tables are represented graphically in **Figure 3.6** and **Figure 3.7**. Data were collected under otherwise identical conditions to a normal environment.

Table 3.1: Electron counts (in mV) using the conventional vaporization method for 1,2,4,5-tetrachlorobenzene at different temperatures and waiting times.

	Temperature in °C/ Waiting time in min								
	150			160			170		
T[a]	0	5	10	0	5	10	0	5	10
5	200	500	500	500	550	600	950	900	900
10	300	500	500	550	600	650	800	1000	900
15	400	500	500	400	500	600		800	850
20	400	500	500	400	400	550	700	750	700
25	400	450	450		350	500			
30	400	400	400	350		500	600	600	600
35	400	400	400		300	450			
40	400	400	400			450			

[a] exposure time in s

Table 3.2: Electron counts (in mV) using the reservoir to vaporise the 1,2,4,5-tetrachlorobenzene at different temperatures and waiting times.

	Temperature in °C/ Waiting time in min												
	140					150				160			
T[a]	0	2	5	10	20	0	2	5	10	0	2	5	10
5	150		250	400	460	350	600	650	800	650	830	1000	1200
10		150	320	450	560	400	720	820	850	850	850	1100	1180
15		120	280	520		490	750	850	850	800		1140	1150
20	150	200	300	500	490		690	790	790	710	820	1200	
25			320	480	560	450		750	850	690		1050	1200
30	220	160	310	390		530	650	820	820	700	900		1050
35				410	450	460	700	700	860		750	990	1090
40	170	220	360	360	500	500	690	730	820	650	690	900	1190
50										700	670	950	1300
60			260	350	420	390				650	700	800	1200
70				330	460	490				580			
80			220										
85				360									

[a] exposure time in s

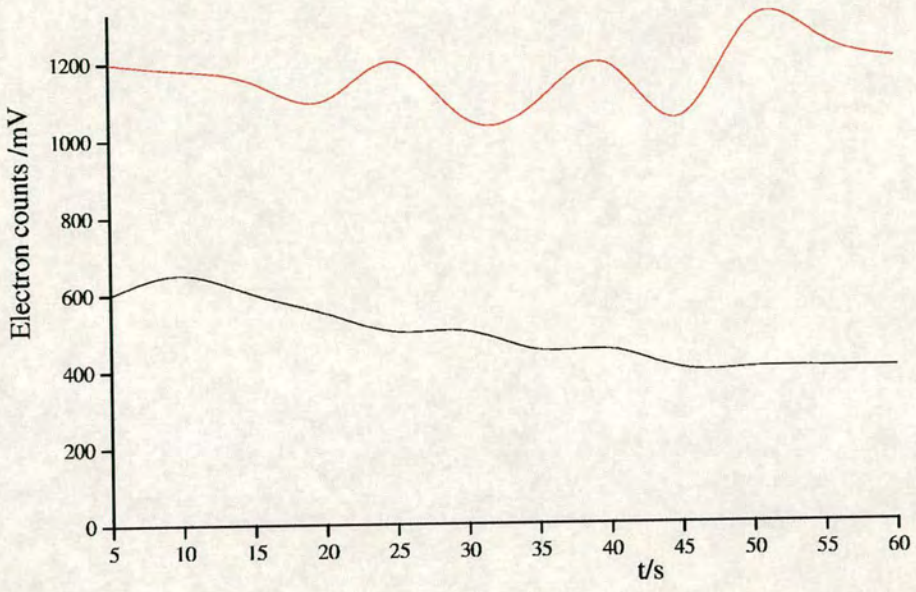

Figure 3.6: Electron count behaviour time exposure at constant temperature 160 °C with a waiting time of 10 min for both the reservoir (red) and the conventional chamber (black)

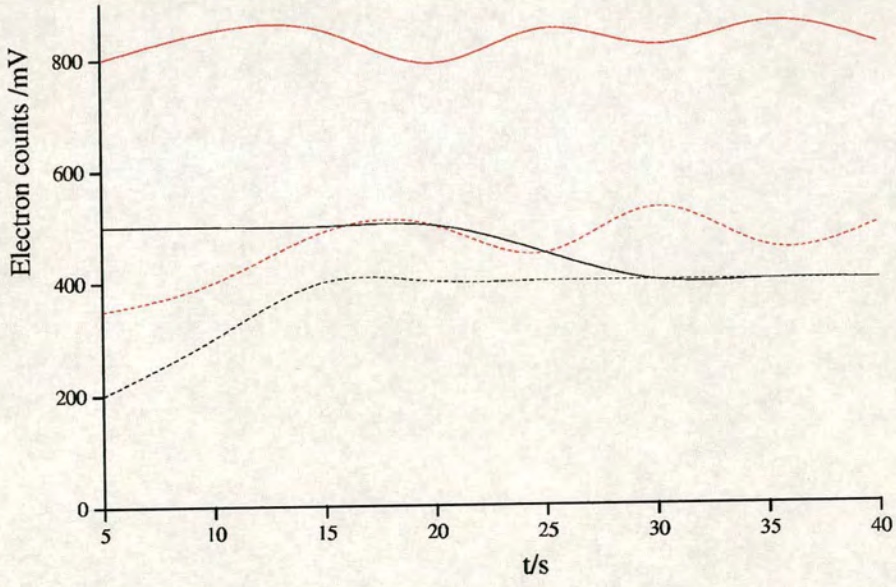

Figure 3.7: Electron count behaviour with respect to time exposure at constant temperature 150 °C, and sampling at two different times: no wait (dashed curve) and 10 minutes wait (continuous curve) for both the reservoir (red) and the conventional chamber (black).

The first collection of data at all temperatures was performed immediately after the temperature of the container had reached the preset temperature. The clock to measure the waiting time was always started as soon as the container was closed from the diffraction chamber. In both cases the experiment was started at the lowest temperature followed by an increase of 10 degrees after the waiting period was over. Roughly one gram of each compound was inserted in each container to ensure the supply would last the experiment. After each experiment we checked that some 1,2,4,5-tetrachlorobenzene was still present in the flask, to ensure that the readings were not influenced by lack of compound.

3.4 **Discussion**

Figure 3.6 shows that with increasing exposure time the number of electron counts decreased for the conventional system, while in the case of the new reservoir no such variation is observed. This is because in the conventional system the amount of gas continuously diminishes, to finally reach the limit characterized by the vaporization rate of 1,2,4,5-tetrachlorobenzene as seen in **Table 3.1,** for the waiting time 0 min at 150°C. This decrease is faster at the highest temperature, 170°C, and is independent of the time waited to build the backing pressure.

Under the same conditions it is clear that the new reservoir design brings more gaseous molecules in contact with the main electron beam, as seen in **Figure 3.6**. In this particular case twice as many electrons are diffracted by the molecules provided by the reservoir with respect to the standard vial. At the end of the exposure time (usually 45 seconds) the counts can be three times those obtained using the conventional method.

In **Figure 3.7** (dashed curves), the number of electrons being diffracted increases with time, when the reading was started as soon as both containers used had reached the set experimental temperature. This increase is simply due to the homogenisation of the temperature inside the container. This effect is only observed at a temperature

of 150°C. Therefore the vaporisation rate of 1,2,4,5-tetrachlorobenzene is of the order of seconds at this specific temperature whereas at temperatures above this critical point it is instantaneous. In addition the experiment revealed that within 15 seconds the maximum rate of vaporisation had been reached for both reservoir and normal vial.

In **Figure 3.7**, for both the conventional vial and new reservoir, we waited ten minutes to build up the backing pressure, which has the effect of increasing the number of electrons being diffracted. However, this effect is barely noticeable in the conventional chamber case, and after half a minute the build-up is drained out and the number of electrons being diffracted falls back to what it was without the wait of ten minutes.

The volume difference between the conventional chamber and the new reservoir has no effect on the maximum number of electrons being diffracted as highlighted by both tables, in the columns of 0 minutes wait. They both show similar behaviour. However, it is important to notice that the size of the new reservoir allows a backing pressure to be built up whereas this does not happen in the conventional set up, hence the decrease in electrons being diffracted.

Looking in more depth at **Table 3.1** it is observed that whatever the wait time is, the decrease in backing pressure is observed after 25 sec. It can be assumed that the speed at which the gaseous molecules leave the chamber is then greater than the vaporisation rate, irrespective of the temperature. For each temperature section it can be noticed that there is no difference in the counts of electrons being diffracted between no wait, a wait of five minutes and a wait of 10 minutes. This indicates that the gaseous molecules are saturated as soon as the temperature is reached inside the chamber, with the exception of the 150°C temperature, for the reason explained earlier.

Waiting ten minutes with the reservoir has the effect of doubling the counts of electrons being diffracted when compared to no wait, as shown in **Table 3.2**. The readings obtained 5 seconds after the opening of the chamber to the nozzle are steady for the full exposure of a single photographic film. The principal advantage of such a design is highlighted when the experiment is carried out at 140°C. From the readings observed, as soon as the chamber reaches that critical temperature, no electrons are being diffracted by a significant number of gaseous molecules. A wait of two minutes gives no significant change, but a five minute wait allows an initial exposure of gaseous molecules. When the wait is further increased to 10 minutes, the steady count of electrons is large enough for the exposure of a single photographic film.

The oscillating shape of the curves is due to the averaging of the count of electrons over the time of sampling and the imprecision of human sampling. Even though an exact reading was not achieved, the error in reading is only of the order of 25 counts. This experiment was not designed to give an actual count of electrons being diffracted but to get an overview of the differences between the two chambers.

A wait of ten minutes at 150°C with the reservoir gives the same count of diffracted electrons as with the conventional vial at 170°C. The electron count is however steady for the 50 seconds required for proper collection of structural information. All of these examples have shown that the use of the reservoir would allow not only the building of a strong and steady backing pressure but also the reduction of the temperature of the experiment by 20°C with respect to the normal set up. This will be particularly significant in the study of thermally unstable compounds.

A significant advantage of the new design is the avoidance of any local hot points, which are inevitable in all other chamber designs due their poor and/or uneven temperature conductance. With the current Pyrex design the hot air was monitored, with a maximum difference of 3°C between the bottom and the top of the inside reservoir, this difference being essentially due to the massive volume being heated. To avoid the hot and cold points observed in the current design, for conventional high temperature measurement, it was decided to use a smaller version of the

reservoir as shown in **Figure 3.8**. Because of its small size it can be directly connected to the nozzle without any intermediate modifications. The rest of the set-up is the same as used for the reservoir.

Figure 3.8: New ampoule based on reservoir design.

A manual for the use of the new reservoir and set-up can be found in appendix D.

3.5 **References**

1 A. J. Blake, P. T. Brain, H. McNab, J. Miller, C. A. Morrison, S. Parsons, D. W. H. Rankin, H. E. Robertson and B. A. Smart, *J. Phys. Chem.*, 1996, **100**, 12280; P. T. Brain, C. A. Morrison, S. Parsons and D. W. H. Rankin, *J. Chem. Soc., Dalton Trans.*, 1996, 4589; N. W. Mitzel and D. W. H. Rankin, *J. Chem. Soc., Dalton Trans.*, 2003, 3650.

2 S. L. Hinchley, M. F. Haddow and D. W. H. Rankin, *Dalton Trans.*, 2004, 384.

3 http://www.swagelock.com

Chapter 4

Molecular structures of 2-chloro- and 2-bromo-thiophene, by the combined analysis of gas-phase electron diffraction data, rotational constants and *ab initio* calculations.

4.1 **Introduction**

The purpose of this work was to provide structural information about two of the most common halogen derivatives of thiophene, 2-chloro and 2-bromo-thiophene. Whereas both were studied in the early seventies by gas-phase electron diffraction a disaccord was born on whether the core ring differs from the symmetry of the parent thiophene.[1,2] In the same period microwave spectroscopy analysis of 2-chlorothiophene was carried out with two isotopic species, but neither could confirm or deny the distortion of their rings with high confidence. For the following decades, only theoreticians were interested in the structure of the chloro-substituted derivative to highlight possible trends within the thiophene, furan and pyrole families.[3-5] At the beginning of the new millennium both species were studied by photoelectron spectroscopy,[6,7] and since there were still no X-ray crystallography structures available for either 2-chlorothiophene or 2-bromothiophene, GED data have been collected. 2-chlorothiophene GED data were paired with information originating from microwave spectroscopy as it had been previously carried out for thiophene.[13] Both structures used flexible restraints provided by *ab initio* calculations, using the Saracen method. Although only three structural refinements are present in this work, two for 2-chlorothiophene (one GED and one GED + MW), and one carried out for 2-bromothiophene, various models were tested. Only the ones showing the best agreement are discussed.

4.2 **Experimental**

4.2.1 Synthesis

Samples of 2-bromothiophene (98%) and 2-chlorothiophene (96%) were purchased from the Aldrich Chemical Co. and used without further purification.

4.2.2 Theoretical methods:

The *ab initio* calculations were performed using the Gaussian 98 program[7] to obtain initial predictions of geometric and vibrational parameters, and vibrational corrections for the rotational constants.

For both halogen-substituted thiophenes the same methodology and basis set were used. Geometry optimisation was carried out with planar (C_s) symmetry using the standard gradient techniques with HF/3-21G(d). Further calculations were carried out with basis sets ranging from 6-31G(d) to 6-311+G(d,p) at HF and MP2 levels of theory to investigate basis-set effects. To investigate the improvement of treatment of electron correlation calculations at 6-31G(d) basis set at MP4(SDQ) and CISD levels were included. As density functional theory seems to perform reasonably well for thiophene, the B3LYP method with all conventional basis sets from 6-31G(d) to 6-311+G(3df,3pd) was also used for both species. The atomic numbering for the bromo- and chloro- substituted thiophenes can be found in **Figure 4.1** and **Figure 4.2** respectively. Vibrational frequency calculations were carried out with the 6-31G(d) basis set at the HF and MP2 levels of theory as well as B3LYP, verifying that the C_s model represents a true minimum on the potential energy surface.

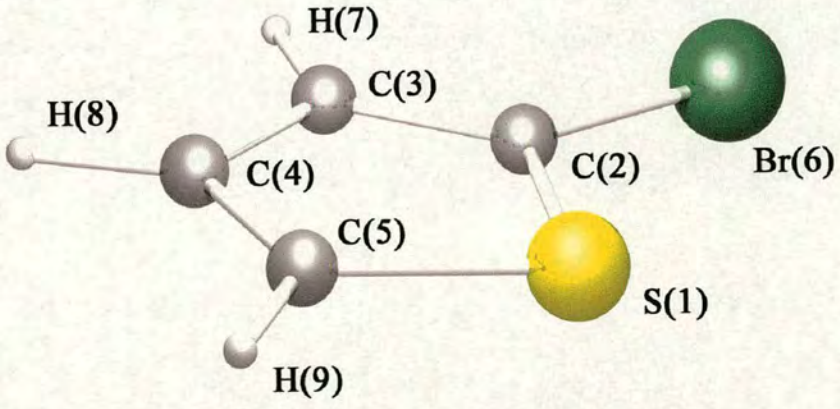

Figure 4.1: Molecular framework for 2-bromothiophene

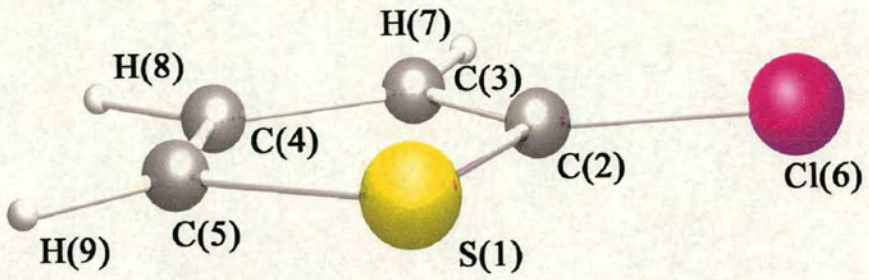

Figure 4.2: Molecular framework for 2-chlorothiophene

4.2.3 Gas Electron Diffraction

Electron diffraction data for both halogen-substituted thiophenes were obtained at two different distances using the Edinburgh apparatus. Data were recorded photographically on Kodak Electron Image plates, which were traced using a computer-controlled Joyce-Loebl MDM6 microdensitometer at the EPSRC Laboratory at Daresbury.[9] Four plates from each distance were studied for 2-bromothiophene, whereas three plates at long and short distances were used for 2-chlorothiophene. Electron wavelengths were determined from the scattering pattern of benzene vapour recorded immediately after each thiophene run. The weighting points for the off-diagonal weight matrices, correlation parameters, and scale factors for the two camera distances are given in **Table 4.1**. The data reduction and analysis of the data were performed using ed@ed,[10] employing the scattering factors of Ross *et al.*[11]

	2-Bromothiophene		2-Chlorothiophene	
camera distance/mm	255.79	91.81	256.26	94.1
T_{sample}/K	338	359	341	346
T_{nozzle}/K	339	370	353	357
Δs /nm^{-1}	2	4	2	4
s_{min}/nm^{-1}	40	120	20	84
sw_1/nm^{-1}	60	140	40	104
sw_2/nm^{-1}	130	212	132	288
s_{max}/nm^{-1}	152	248	154	336
correlation parameter	-0.0509	-0.3734	0.1473	0.2630
scale factor, k_a	1.000(4)	0.879(20)	0.876(5)	0.835(20)
electron wavelength /pm	6.02	6.02	6.02	6.02
a	1	2	1	2

Table 4.1: GED data analysis parameters for 2-bromothiophene and 2-chlorothiophene

On the basis of *ab initio* predictions structural refinements on 2-bromothiophene were carried out assuming C_s symmetry (**Figure 4.1**). In total fifteen geometric parameters were employed, seven parameters to define the core ring structure and a further eight to define the hydrogen and bromine atom positions. Parameters p_1 and p_2 define the average of distances S(1)-C(2) and S(1)-C(5), and their difference, respectively. The average of the bond distances C(2)-C(3) and C(5)-C(4) is defined by parameter p_3. The difference associated with it is defined by p_4. The carbon bromine distance, C(2)-Br(6) is described by p_5. The average bond distance between C(3)-H(7), C(4)-H(8) and C(5)-H(9) is described by p_6. The difference between C(3)-H(7) and C(4)-H(8) is defined by p_7, while p_8 represents the difference between C(4)-H(8) and C(5)-H(9). The C(5)-S(1)-C(2) angle is defined by p_9. The average angle between S(1)-C(2)-C(3) and S(1)-C(5)-C(4) is described by p_{10}, while its difference is represented by p_{11}. The parameter describing the angle S(1)-C(2)-Br(6) is p_{12}. The average angle between C(2)-C(3)-H(7), C(5)-C(4)-H(8) and S(1)-C(5)-H(9) is defined by p_{13}, while the average between C(5)-C(4)-H(8) and C(2)-C(3)-H(7) is represented by p_{14} and p_{15} defines the difference between C(3)-C(4)-H(8) and C(2)-C(3)-H(7).

On the basis of *ab initio* predictions structural refinements on 2-chlorothiophene were carried out assuming C_s symmetry (**Figure 4.2**). In total fifteen geometric parameters were employed, comprising seven to define the core ring structure and a further eight to define the hydrogen and chlorine atom positions. Parameters p_1, p_2 and p_5 define the average distance between S(1)-C(2), S(1)-C(5) and C(2)-Cl(6), the difference between S(1)-C(2) and S(1)-C(5), and the difference between S(1)-C(5) and C(2)-Cl(6), respectively. The average of the bond distances C(2)-C(3) and C(5)-C(4) is defined by parameter p_3. The difference associated with it, is defined by p_4. The average bond distance between C(3)-H(7), C(4)-H(8) and C(5)-H(9) is described by p_6. The difference between C(3)-H(7) and C(4)-H(8) is defined by p_7, while p_8 represents the difference between C(4)-H(8) and C(5)-H(9). The C(5)-S(1)-C(2) angle is defined by p_9. The average angle between S(1)-C(2)-C(3) and S(1)-C(5)-C(4) is described by p_{10}, while its difference is represented by p_{11}. The parameter describing the angle S(1)-C(2)-Cl(6) is p_{12}. The average angle between C(2)-C(3)-H(7), C(5)-C(4)-H(8) and S(1)-C(5)-H(9) is defined by p_{13}, while the average between C(5)-C(4)-H(8) and C(2)-C(3)-H(7) is represented by p_{14} and p_{15} defines the difference between C(3)-C(4)-H(8) and C(2)-C(3)-H(7).

Although the starting geometry estimate was taken from the MP2/6-311+G(d,p) level calculation for both halogen substituted thiophenes, the initial amplitudes of vibration (u) were obtained from the MP2(fc)/6-31G(d) force field, from which curvilinear corrections were extracted using the SHRINK program.[12] This force field was chosen as previously published thiophene structures revealed that MP2(fc)/6-31G(d) performed better than higher basis sets.[13]

4.2.4 Microwave data

The molecule 2-chlorothiophene is an asymmetric top with three rotational constants A_0, B_0 and C_0. However as it is planar the rotational constant C is equal to the sum of

A and *B*. These rotational constants were taken from a previous study[14] for which two isotopic species ($C_4SH_3{}^{35}Cl$ and $C_4SH_3{}^{37}Cl$) were investigated. The data were corrected to A_z, B_z and C_z. values using vibrational corrections calculated from a scaled force field. For previously stated reasons,[15] the uncertainties in the rotational constants areas result of the propagation of a 10% error in the correction for each mode. This was done to compensate for neglecting the anharmonic effects. All changes in geometry on isotopic substitution were neglected.

4.3 **Results**

4.3.1 Theoretical methods

Values of bond lengths and angles derived from calculations and electron diffraction measurements are presented in **Table 4.2** and **Table 4.3** for 2-bromothiophene and 2-chlorothiophene respectively. Other results from *ab initio* calculations are provided in appendix E on the attach CD.

For both compounds studied, the predicted geometry parameters are less affected by the definition of the basis set within the same level of theory than by the calculation method used, as previously observed for thiophene.[13] As expected the inclusion of electron correlation increases the multiple bond lengths within the ring. For 2-bromothiophene, bond distances C(2)-C(3) and C(4)-C(5) increase by 3.4 pm from 134.2 pm and 134.4 pm at HF/6-31G(d) to 137.6 pm and 137.6 pm for MP2/6-31G(d). Identical increases are observed for the 2-chlorothiophene. Further improvement in the treatment of electron correlation resulted in an increase of an average 2.2 pm at MP4(SDQ)/6-31G(d) and an even smaller increase of 1.0pm for CISD/6-31G(d) with respect to the self-consistent field theory. The effects of the electron correlation do not converge when the S(1)-C(2/5) bonds are involved. In fact MP2 and CISD show shorter bond lengths for both substituents with respect to the HF level while MP4 shows an average increase of 0.7 pm, with the same basis set and independently of the substitution. For 2-chlorothiophene the bond to the halogen

atom is not affected by the electron correlation whereas for 2-bromothiophene the carbon-bromine bond follows the same trend as the multiple bonds.

The addition of two "d" type and one "f" type function to the 6-311+G(d,p) basis set reduced all the core ring bond lengths, especially those involving sulfur and the halogen substituents. The C(2)-X(6) bond lengths are reduced on average by 1 pm from MP2/6-311+G(d,p) to MP2/6-311+G(3df,3pd), as C(2/5)-S(1) while a shrinkage of 0.3 pm is observed for the multiple carbon bond.

The addition of diffuse functions has practically no effect on the description of the ring or on the halogenated substituents. The biggest variation observed is of the order of 0.1 pm and 0.2 pm for 2-chloro- and 2-bromothiophene respectively. The biggest change affects the C(2)-C(3) and C(5)-C(4) bond distances.

Overall 1° is the biggest increase in bond angle observed through changes in treatment of electron correlation. As observed previously for thiazole,[15] the angle involving the sulfur is the most affected by the electron correlation, varying from 90.5° at HF/6-31G(d) to 91.1° at HF/6-31G(d) and back to 90.5° at MP4(SDQ)/6-31G(d) and 90.7° at CISD/6-31G(d) for 2-chlorothiophene. For 2-bromothiophene similar variations are observed.

With B3LYP theory, similar behaviour is observed as for MP2 in comparison to HF. Although, as expected for electron correlation methods, the multiple bonds are longer by an average of 2 pm with respect to self-consistent field theory, the S(1)-C(2/5) bonds are longer by 1.4 pm for both halogen-substituted thiophenes. While no drastic changes are observed through the increase in basis set and in definition of the "s" and "p" orbitals, the inclusion of two "d" and one "f" polarization functions has the effect of returning a similar geometry to that obtained by MP2/6-31G(d). It should be emphasized that the multiple bonds C(2/5)-C(3/4) are constant through all basis sets chosen for the density functional theory calculations. The descriptions of the ring angles at B3LYP/6-31G(d) are closest to those calculated at the CISD/6-31G(d) level.

Table 4.2: Calculated (r_e) and experimental (r_{h1}) structures of 2-bromothiophene.[a]

	Level of theory/ Basis set										
	HF		MP2				MP4	CISD	B3LYP		GED
	6-31G(d)	6-311+G(d,p)	6-31G(d)	6-311G(d)	6-311+G(d)	6-311+G(d,p)	6-31G(d)	6-31G(d)	6-31G(d)	6-311+G(3df,3pd)	
S(1)-C(2)	172.7	172.7	172.1	171.9	171.9	171.8	173.5	172.3	174.0	172.4	172.4(5)
S(1)-C(5)	172.8	172.7	172.1	171.7	171.7	171.7	173.4	172.2	173.9	172.2	172.4(5)
C(2)-C(3)	134.2	134.3	137.6	138.0	138.2	138.2	136.4	135.2	136.6	136.3	138.1(4)
C(2)-Br(6)	187.4	187.7	188.2	187.7	187.7	187.6	188.9	187.5	188.5	188.5	185.6(3)
C(3)-C(4)	143.7	143.7	141.9	142.0	142.1	142.0	143.5	143.0	143.0	142.2	142.4(9)
C(3)-H(7)	107.2	107.2	108.4	108.4	108.4	108.4	108.5	107.7	108.3	107.9	109.1(4)
C(4)-C(5)	134.4	134.4	137.6	137.9	138.1	138.1	136.5	135.4	136.7	136.3	136.8(11)
C(4)-H(8)	107.3	107.3	108.5	108.5	108.5	108.4	108.6	107.8	108.5	108.0	109.2(4)
C(5)-H(9)	107.1	107.1	108.3	108.3	108.3	108.2	108.4	107.6	108.2	107.7	108.9(4)
C(2)-S(1)-C(5)	90.6	90.7	91.1	91.4	91.5	91.5	90.5	90.7	90.8	91.2	91.2(1)
S(1)-C(2)-C(3)	112.8	112.7	112.7	112.5	112.4	112.4	113.0	112.9	112.5	112.3	112.7(3)
S(1)-C(2)-Br(6)	120.5	120.8	120.6	121.2	121.3	121.3	120.4	120.5	120.4	120.8	120.4(3)
C(2)-C(3)-C(4)	111.8	111.8	111.4	111.5	111.5	111.5	111.5	111.6	111.9	111.8	110.8(7)
C(2)-C(3)-H(7)	123.8	123.8	123.2	123.1	123.1	123.1	123.6	123.6	123.4	123.5	123.6(10)
C(3)-C(4)-C(5)	112.8	112.8	112.9	112.7	112.7	112.7	112.8	112.7	113.2	113.0	113.6(5)
C(5)-C(4)-H(8)	123.8	123.8	123.1	123.1	123.1	123.1	123.6	123.7	123.4	123.5	124.0(10)
S(1)-C(5)-C(4)	112.1	112.1	111.9	111.9	111.9	111.9	112.2	112.1	111.7	111.7	111.7(3)
S(1)-C(5)-H(9)	120.1	120.0	119.9	119.8	119.9	119.9	119.8	120.0	119.8	119.9	118.3(19)

[a] distances in pm, angles in °

Table 4.3: Calculated (r_e) and experimental (r_{h1}) structures of 2-chlorothiophene.[a]

	Level of theory/ Basis set										
	HF		MP2				MP4	CISD	B3LYP		GED
	6-31G(d)	6-311+G(d,p)	6-31G(d)	6-311G(d)	6-311+G(d)	6-311+G(d,p)	6-31G(d)	6-31G(d)	6-31G(d)	6-311+G(3df,3pd)	
S(1)-C(2)	173.0	172.8	172.5	172.0	172.0	172.0	173.8	172.6	174.4	172.7	172.9(3)
S(1)-C(5)	172.9	172.8	172.1	171.8	171.8	171.7	173.4	172.3	173.9	172.2	172.7(3)
C(2)-C(3)	134.2	134.1	137.5	137.8	138.0	138.0	136.3	135.2	136.6	136.3	136.2(4)
C(2)-Cl(6)	172.1	172.3	172.0	171.9	171.8	171.8	172.6	171.7	173.3	172.0	172.1(5)
C(3)-C(4)	143.7	143.8	141.9	142.0	142.1	142.1	143.5	143.0	142.9	142.2	143.6(7)
C(3)-H(7)	107.2	107.2	108.4	108.4	108.4	108.4	108.5	107.7	108.3	107.9	112.4(7)
C(4)-C(5)	134.3	134.4	137.5	137.9	138.0	138.1	136.5	135.3	136.6	136.3	136.7(5)
C(4)-H(8)	107.3	107.3	108.5	108.5	108.5	108.4	108.6	107.8	108.5	108.0	112.5(6)
C(5)-H(9)	107.1	107.1	108.3	108.2	108.3	108.2	108.4	107.6	108.2	107.7	112.2(6)
C(2)-S(1)-C(5)	90.5	90.5	91.1	91.3	91.3	91.4	90.5	90.7	90.7	91.1	91.2(2)
S(1)-C(2)-C(3)	112.8	112.9	112.5	112.6	112.5	112.5	112.8	112.8	112.4	112.3	113.1(5)
S(1)-C(2)-Cl(6)	120.6	120.5	120.8	120.9	121.0	121.0	120.4	120.6	120.6	120.7	120.1(2)
C(2)-C(3)-C(4)	111.7	111.7	111.6	111.5	111.5	111.5	111.6	111.7	111.9	111.8	110.8(7)
C(2)-C(3)-H(7)	123.7	123.7	123.1	122.9	122.9	122.9	123.5	123.5	123.4	123.3	124.1(10)
C(3)-C(4)-C(5)	112.9	112.8	112.9	112.7	112.7	112.7	112.8	112.8	113.2	113.1	113.7(5)
C(5)-C(4)-H(8)	123.8	123.7	123.1	123.1	123.1	123.1	123.7	123.6	123.4	123.6	124.1(10)
S(1)-C(5)-C(4)	112.1	112.1	111.9	111.9	111.9	111.9	112.2	112.1	111.8	111.7	111.2(3)
S(1)-C(5)-H(9)	120.0	120.0	119.8	119.7	119.8	119.8	119.7	119.9	119.7	119.9	115.1(31)

[a] distances in pm, angles in °

4.3.2 Gas Electron Diffraction

The model used for the GED refinement of 2-bromothiophene was based upon the geometry obtained from the optimised *ab initio* calculations. The least-squares refinement of the structure resulted in an R_G factor of 0.035 (R_D = 0.041), with optimized parameters listed in **Table 4.4** and dependent parameters in **Table 4.5**. A summary of final bond distances and amplitudes of vibration is recorded in **Table 4.6**. In total, 13 geometrical parameters and eight groups of amplitudes of vibration were refined. Flexible restraints were employed during the refinement using the SARACEN[16] method. Altogether, five geometric and one amplitude restraints were employed. These are listed in **Table 4.7**. For a full list of the final bond distances and amplitudes of vibration, see appendix E on the CD. The least-squares correlation matrix for the structural refinement is shown in **Table 4.8**. The success of the final refinement can be assessed on the basis of the molecular scattering curves, **Figure 4.3**, and radial distribution curve **Figure 4.4**.

Table 4.4: Geometrical parameters (r_{h1}) for 2-bromothiophene.[a, b]

	Parameter	GED	MP2/6-311+G(d,p)
p_1	av$r$ S(1)C(2)r S(1)C(5)	172.4(1)	171.7
p_2	dif$r$ S(1)C(2)r S(1)C(5)	0.0(8)	0.2
p_3	av$r$ C(2)C(3)r C(5)C(4)	137.4(4)	138.2
p_4	dif$r$ C(2)C(3)r C(5)C(4)	1.3(17)	0.1
p_5	r C(2)Br(6)	185.6(3)	187.6
p_6	av$r$ C(3)H(7)r C(4)H(8)r C(5)H(9)	109.1(4)	108.3
p_7	dif$r$ C(3)H(7)r C(4)H(8)	0.1	0.1
p_8	dif$r$ C(4)H(8)r C(5)H(9)	0.2	0.2
p_9	∠C(5)S(1)C(2)	91.2(1)	91.5
p_{10}	av∠S(1)C(2)C(3)∠S(1)C(5)C(4)	112.2(2)	112.2
p_{11}	dif∠S(1)C(5)C(4)∠S(1)C(2)C(3)	1.0(4)	0.6
p_{12}	∠S(1)C(2)Br(6)	120.4(3)	121.3
p_{13}	av[av∠CCH(7/8)∠S(1)C(5)H(9)]	121.1(9)	121.5
p_{14}	av∠CCH(7/8)	123.8(9)	123.1
p_{15}	dif∠CCH(7/8)	0.4(8)	0.0

[a] distances in pm, angles in °

[b] see text for parameter definitions

Table 4.5: Dependent parameters (r_{h1}) for 2-bromothiophene.[a]

	Parameter	GED	MP2/6-311+G(d,p)
d_1	r S(1)C(2)	172.4(5)	171.8
d_2	r S(1)C(5)	172.4(5)	171.7
d_3	r C(2)C(3)	138.1(7)	138.2
d_4	r C(5)C(4)	136.8(11)	138.1
d_5	r C(3)C(4)	142.4(9)	142.0
d_6	∠S(1)C(2)C(3)	112.7(3)	112.4
d_7	∠S(1)C(5)C(4)	111.7(3)	111.9
d_8	∠C(2)C(3)H(7)	123.6(10)	123.1
d_9	∠S(1)C(5)H(9)	118.3(19)	119.9
d_{10}	∠C(5)C(4)H(8)	124.0(10)	123.1
d_{11}	∠C(2)C(3)C(4)	110.8(7)	111.5
d_{12}	∠C(5)C(4)C(3)	113.6(5)	112.7

[a] distances in pm, angles in °

Table 4.6: Bond distances (r_a/pm) and amplitudes of vibration (u/pm) obtained in the GED refinement of 2-bromothiophene.

u	Atom pair	r_a	Amplitude	
u_1	S(1)-C(2)	172.1(4)	5.9	Tied to u_4
u_2	S(1)-C(5)	172.2(5)	5.9	Tied to u_4
u_3	C(2)-C(3)	137.9(7)	5.5	Tied to u_7
u_4	C(2)-Br(6)	185.5(2)	6.1(2)	
u_5	C(3)-C(4)	142.5(9)	5.7	Tied to u_7
u_6	C(3)-H(7)	109.0(3)	6.6	Tied to u_9
u_7	C(4)-C(5)	136.8(10)	5.5(3)	
u_8	C(4)-H(8)	109.1(3)	6.6	Tied to u_9
u_9	C(5)-H(9)	108.8(3)	6.6(4)	
u_{10}	S(1)...C(3)	258.8(7)	4.6(3)	
u_{11}	S(1)...C(4)	256.3(6)	4.6	Tied to u_{10}
u_{12}	S(1)...Br(6)	310.0(2)	8.0(2)	
u_{14}	S(1)...H(8)	360.6(8)	10.6	Tied to u_{19}
u_{15}	S(1)...H(9)	244.3(17)	11.3	Tied to u_{30}
u_{16}	C(2)...C(4)	230.7(4)	4.8	Tied to u_{10}
u_{17}	C(2)...C(5)	246.1(3)	5.1	Tied to u_{10}
u_{18}	C(2)...H(7)	216.48(12)	10.7	Tied to u_{30}
u_{19}	C(2)...H(8)	332.5(7)	10.8(26)	
u_{20}	C(2)...H(9)	350.2(8)	11.0	Tied to u_{19}
u_{21}	C(3)...C(5)	233.6(7)	4.8	Tied to u_{10}
u_{22}	C(3)...Br(6)	289.5(4)	5.5	
u_{23}	C(3)...H(8)	221.7(13)	10.8	Tied to u_{30}
u_{24}	C(3)...H(9)	338.2(10)	10.7	Tied to u_{19}
u_{25}	C(4)...Br(6)	410.4(3)	5.6(6)	
u_{26}	C(4)...H(7)	225.3(15)	10.7	Tied to u_{30}
u_{27}	C(4)...H(9)	219.5(20)	10.5	Tied to u_{30}
u_{28}	C(5)...Br(6)	427.1(3)	5.7	Tied to u_{25}
u_{29}	C(5)...H(7)	335.9(10)	10.8	Tied to u_{19}
u_{30}	C(5)...H(8)	215.0(14)	10.7(9)	

Table 4.7: Flexible restraints used in the GED refinement for 2-bromothiophene.

Restraints	Value /pm or °	Uncertainty /pm or °
dif*r* S(1)C(2)*r* S(1)C(5)	0.2	1.0
av∠CCH(7/8)	123.1	1.0
av[av∠CCH(7/8)∠S(1)C(5)H(9)]	121.5	1.0
dif∠CCH(7/8)	0.0	1.0
dif∠S(1)C(5)C(4)∠S(1)C(2)C(3)	0.6	0.5
u_{30}	9.7	0.9

Table 4.8: Least-squares correlation matrix (x100) for GED structure refinement of 2-bromothiophene.[a]

	p_4	p_5	p_9	p_{10}	p_{11}	p_{12}	u_1	u_4	u_{10}	u_{24}
p_1		-54					61			
p_2	-53					-85				
p_3			82	-90				83	72	
p_4			-59			61		-55		
p_5					67	-54	-81			
p_9				-90				71	57	
p_{10}								-75	-68	
p_{11}							-51			
u_4									71	
u_{20}										82
u_{23}										52

[a] Only elements with the absolute values > 50% are shown

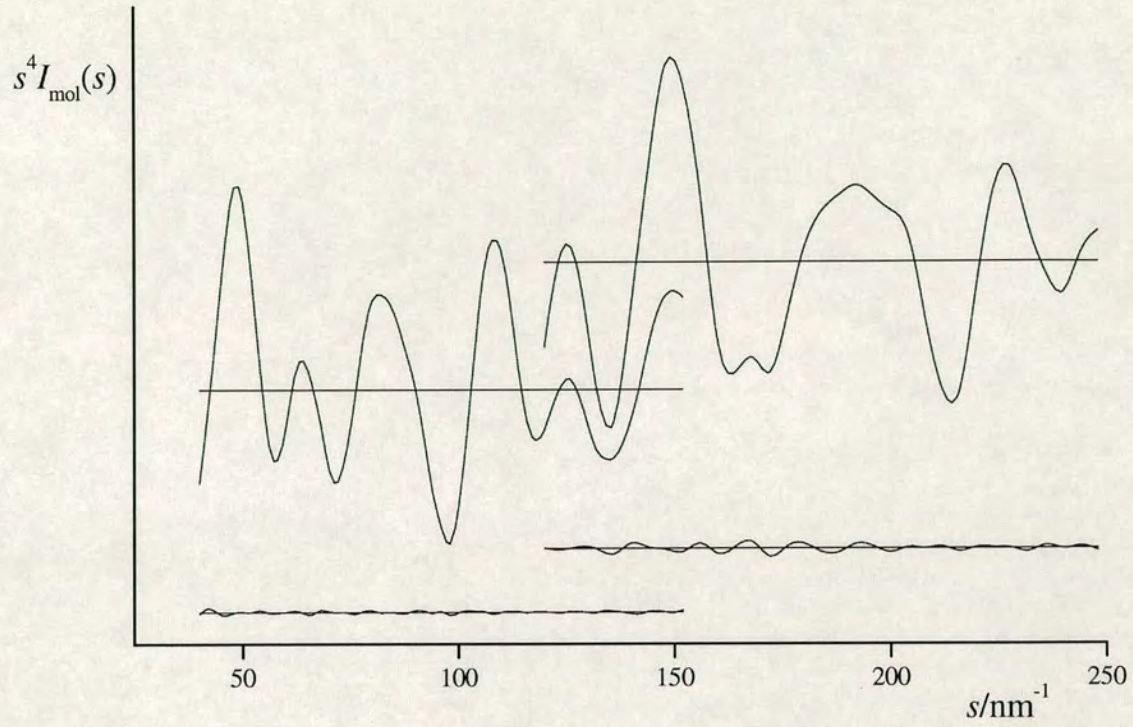

Figure 4.3: Experimental and final weighted difference (experimental-theoretical) molecular scattering intensities for 2-bromothiophene.

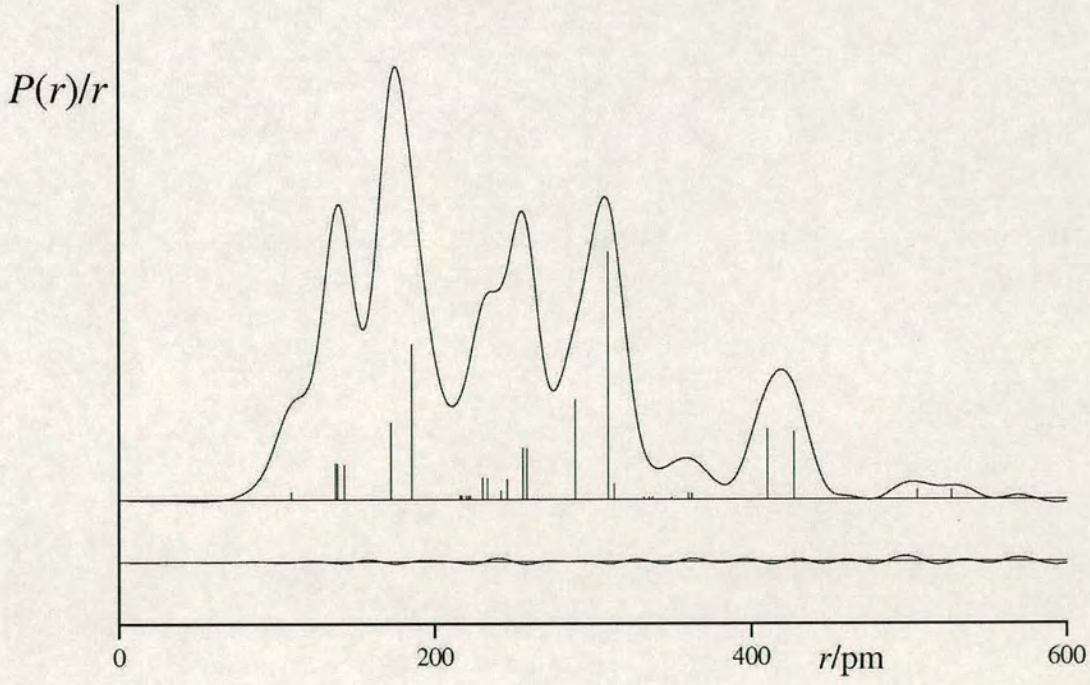

Figure 4.4: Experimental and difference (experimental – theoretical) radial distribution curves, $P(r)/r$, for 2-bromothiophene. Before Fourier inversion, the data were multiplied by $s.\exp(-0.00002s^2)/(Z_S-f_S)(Z_{Br}-f_{Br})$

The models used for the GED and GED/microwave spectroscopy (GED+MW) refinements of 2-chlorothiophene were based upon the geometry obtained from the optimised *ab initio* calculations and described by the same geometrical model. The least-squares refinement of the structure resulted in an R_G factor of 0.067 (R_D = 0.059) for GED and R_G factor of 0.085 (R_D = 0.071) for GED+MW, with optimized parameters listed in **Table 4.9** and dependent parameters in **Table 4.10**. A summary of final bond distances and amplitudes of vibration is recorded in **Table 4.11**. In total, 13 geometrical parameters and eight groups of amplitudes of vibration were refined. Flexible restraints were employed during the refinement using the SARACEN[14] method. All together, seven geometric and one amplitude restraints were employed for the GED refinement whereas six additional restraints were added for the GED+MW on the rotational constants. These are listed in **Table 4.12**. For a full list of the final bond distances and amplitudes of vibration, see appendix E on the CD. The least squares correlation matrix for the structural refinement is shown in **Table 4.13** and for the GED+MW refinement it is shown in **Table 4.14.** The success of the final refinement can be assessed on the basis of the molecular scattering curves, **Figure 4.5**, and radial distribution curve **Figure 4.6**. The GED+MW curves can be found in appendix E on the CD since no major visual differences can be noted.

Table 4.9: Geometrical parameters (r_{h1}) for 2-chlorothiophene.[a,b]

	Parameter	GED	GED + MW	MP2/6-311+G(d,p)
p_1	av$r$ S(1)C(2)r S(1)C(5)r C(2)Cl(6)	172.6(1)	172.5(1)	171.8
p_2	dif$r$ S(1)C(2)r S(1)C(5)	0.2(2)	0.2(2)	0.2
p_3	av$r$ C(2)C(3)r C(5)C(4)	136.4(3)	135.6(3)	138.0
p_4	dif$r$ C(5)C(4)r C(2)C(3)	0.5(7)	0.8(7)	0.1
p_5	dif$r$ S(1)C(5)r C(2)Cl(6)	0.6(8)	0.9(8)	0.1
p_6	av$r$ C(3)H(7)r C(4)H(8)r C(5)H(9)	112.4(6)	109.6(6)	108.4
p_7	dif$r$ C(3)H(7)r C(4)H(8)	0.1	0.1	0.1
p_8	dif$r$ C(4)H(8)r C(5)H(9)	0.2	0.2	0.2
p_9	∠C(5)S(1)C(2)	91.2(2)	90.9(2)	91.1
p_{10}	av∠S(1)C(2)C(3)∠S(1)C(5)C(4)	112.1(3)	112.2(3)	112.2
p_{11}	dif∠S(1)C(5)C(4)∠S(1)C(2)C(3)	1.9(6)	2.1(6)	0.6
p_{12}	∠S(1)C(2)Cl(6)	120.1(2)	120.0(2)	120.8
p_{13}	av∠CCH(7/8)∠S(1)C(5)H(9)	119.6(16)	120.0(14)	121.4
p_{14}	av∠CCH(7/8)	124.1(9)	123.5(8)	123.0
p_{15}	dif∠CCH(7/8)	0.0(10)	0.3(10)	0.2

[a] distances in pm, angles in °

[b] see text for parameter definitions

Table 4.10: Dependent parameters (r_{h1}) for 2-chlorothiophene.[a]

	Parameter	GED	GED + MW	MP2/6-311+G(d,p)
d_1	rS1C2	172.9(3)	172.9(3)	171.97
d_2	rS1C5	172.7(3)	172.7(3)	171.72
d_3	rC3C4	143.6(7)	143.6(7)	142.07
d_4	rC2C3	136.2(4)	135.2(4)	137.98
d_5	rC5C4	136.7(5)	136.0(5)	138.05
d_6	angS1C2C3	113.1(5)	113.3(5)	112.5344
d_7	angS1C5C4	111.2(3)	111.2(4)	111.9106
d_8	angC2C3C4	110.8(7)	110.7(7)	111.515
d_9	angC5C4C3	113.7(5)	113.9(5)	112.6786
d_{10}	rCl6C2	172.1(5)	171.8(5)	171.77
d_{11}	angC2C3H7	124.1(10)	123.3(10)	122.9382
d_{12}	angC5C4H8	124.1(10)	123.6(10)	123.1081
d_{13}	angS1C5H9	115.1(32)	115.1(26)	119.8037
d_{14}	A_z ^{35}Cl[b]		5391.6(23)	5393(6)[c]
d_{15}	A_z ^{37}Cl[b]		5391.5(23)	5393(6)[c]
d_{16}	B_z ^{35}Cl[b]		1874.4(2)	1874.4(3)[c]
d_{17}	B_z ^{37}Cl[b]		1818.0(2)	1818.0(3)[c]
d_{18}	C_z ^{35}Cl[b]		1390.9(1)	1390.9(2)[c]
d_{19}	C_z ^{37}Cl[b]		1359.5(1)	1359.5(2)[c]

[a] distances in pm, angles in °

[b] Rotational constants in MHz

[c] Oberved rotational constants in MHz

Table 4.11: Bond distances (r_a/pm) and amplitudes of vibration (u/pm) obtained in the GED and combined GED+MW refinement of 2-chlorothiophene.

u	Atom pair	r_a		Amplitude		
		GED	GED + MW	GED	GED + MW	
u_1	S(1)-C(2)	172.7(3)	172.7(3)	4.9	4.9	Tied to u_4
u_2	S(1)-C(5)	172.6(3)	172.5(3)	4.9	4.9	Tied to u_4
u_3	C(2)-C(3)	136.1(4)	135.1(4)	4.4	3.8	Tied to u_7
u_4	C(2)-Cl(6)	172.0(5)	171.7(5)	4.8(2)	4.8(2)	
u_5	C(3)-C(4)	143.8(7)	143.8(7)	4.6	3.9	Tied to u_7
u_6	C(3)-H(7)	112.2(6)	109.4(6)	7.5	7.7	Tied to u_9
u_7	C(4)-C(5)	136.8(5)	136.(5)	4.4(5)	3.8(5)	
u_8	C(4)-H(8)	112.3(6)	109.5(6)	7.5	7.7	Tied to u_9
u_9	C(5)-H(9)	112.0(6)	109.2(6)	7.5(6)	7.7(6)	
u_{10}	S(1)...C(3)	258.3(6)	257.8(5)	5.7	5.7	Tied to u_{11}
u_{11}	S(1)...C(4)	255.7(5)	255.0(5)	5.7(4)	5.7(4)	
u_{12}	S(1)...Cl(6)	298.3(2)	297.8(2)	7.8(2)	7.9(2)	
u_{15}	S(1)...H(9)	241.7(40)	239.5(32)	11.3	11.3	Tied to u_{11}
u_{16}	C(2)...C(4)	230.1(7)	229.1(6)	5.6(6)	5.4(7)	
u_{17}	C(2)...C(5)	246.8(7)	246.2(7)	6.4	6.4	Tied to u_{11}
u_{18}	C(2)...H(7)	219.2(13)	215.1(10)	10.2	9.8	Tied to u_{16}
u_{21}	C(3)...C(5)	234.8(7)	234.4(8)	5.6	5.4	Tied to u_{16}
u_{22}	C(3)...Cl(6)	275.4(4)	274.1(3)	5.8(6)	5.8(6)	
u_{23}	C(3)...H(8)	224.1(13)	222.2(13)	10.3	9.9	Tied to u_{16}
u_{25}	C(4)...Cl(6)	396.8(5)	395.6(5)	7.0(7)	7.0(7)	
u_{26}	C(4)...H(7)	226.6(16)	225.2(16)	10.3	9.9	Tied to u_{16}
u_{27}	C(4)...H(9)	227.9(29)	224.8(22)	10.1	9.7	Tied to u_{16}
u_{28}	C(5)...Cl(6)	414.4(3)	413.5(3)	7.2	7.9	Tied to u_{25}
u_{30}	C(5)...H(8)	219.3(13)	215.7(11)	10.2	9.8	Tied to u_{16}

Table 4.12: Flexible restraints used in GED and GED+MW refinements for 2-chlorothiophene

Restraints	Value /pm or °	Value /pm or °	Uncertainty /pm or °
dif$r$ C(5)C(4)r C(2)C(3)	0.1	0.1	0.7
dif$r$ S(1)C(2)r S(1)C(5)	0.3	0.3	0.2
dif$r$ S(1)C(5)r C(2)Cl(6)	0.1	0.1	1.0
dif∠S(1)C(5)C(4)∠S(1)C(2)C(3)	0.6	0.6	1.0
av∠CCH(7/8)∠S(1)C(5)H(9)	121.4	121.4	2.0
dif∠CCH(7/8)	0.2	0.2	1.0
av∠CCH(7/8)	123.0	123.0	1.0
u_9	7.4	7.4	0.7
A_z $^{35}Cl^a$		5393.0	6.0
A_z $^{37}Cl^a$		5393.0	6.0
B_z $^{35}Cl^a$		1874.4	0.3
B_z $^{37}Cl^a$		1818.0	0.3
C_z $^{35}Cl^a$		1390.9	0.2
C_z $^{37}Cl^a$		1359.6	0.2

[a] Rotational constants in MHz

Table 4.13: Least-squares correlation matrix (x100) for GED structure refinement of 2-chlorothiophene.[a]

	p_9	p_{10}	p_{11}	p_{12}	u_5	u_{15}	u_{23}	u_{24}	k_2
p_3		-58			74				
p_5	-63	82	59	-67					
p_9		-87		51		56			
p_{10}				-66	-55	-57			
p_{11}				-59					
p_{13}							-52		
u_1									76
u_{15}								55	

[a] Only elements with the absolute values > 50% are shown; k_2 is a scale factor.

Table 4.14: Least-squares correlation matrix (x100) for GED+MW structure refinement of 2-chlorothiophene.[a]

	p_9	p_{10}	p_{12}	u_5	u_{23}	u_{24}	k_2
p_3	57	-71		67			
p_5	-64	82	-60				
p_9		-85					
p_{10}			-56	-57			
p_{11}					-57		
u_1							75
u_{15}						57	

[a] Only elements with the absolute values > 50% are shown; k_2 is a scale factor

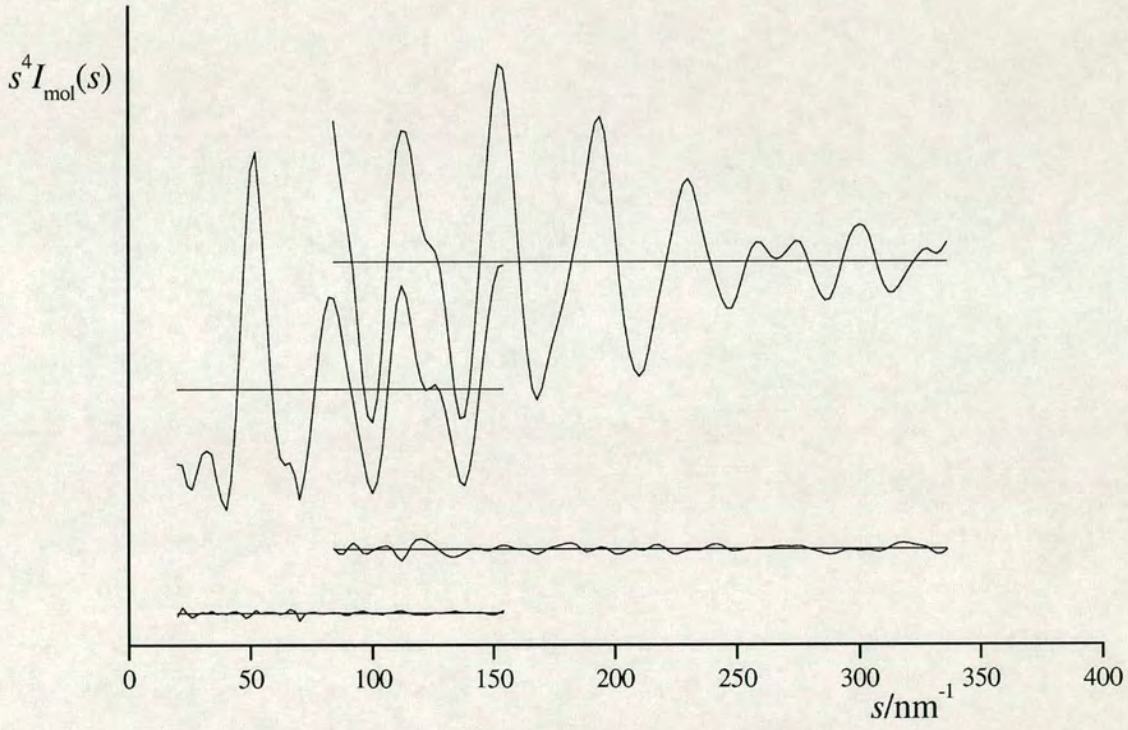

Figure 4.5: Experimental and final weighted difference (experimental-theoretical) molecular scattering intensities for 2-chlorothiophene.

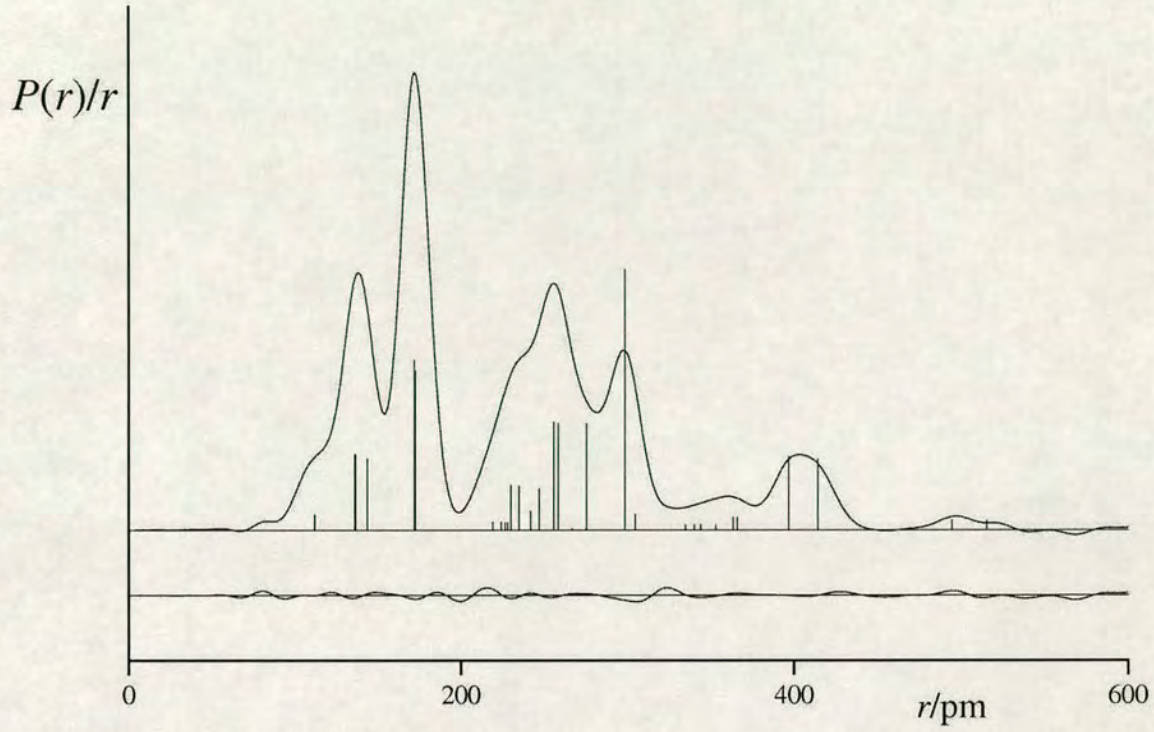

Figure 4.6: Experimental and difference (experimental – theoretical) radial distribution curves, $P(r)/r$, for 2-chlorothiophene. Before Fourier inversion, the data were multiplied by $s.\exp(-0.00002s^2)/(Z_S-f_S)(Z_{Cl}-f_{Cl})$

4.4 **Discussion**

The refinement performed on 2-bromothiophene was initially carried out using a larger s range including the region $2.0<s<4.0$. During the refinement it was observed that the ring was very different from the C_{2v} of the parent thiophene, as reported previously by R. Karl and S. Bauer.[1] Although in agreement with the previously published structure, the combination of a high R_G = 0.083 (R_D= 0.063) and the fact that the refined structure did not agree with theory, led us to investigate removing data from the region from $20<s<40$ from the refinement, as was carried out previously by J. L. Derissen.[2] The final refinement shows little deviation from the C_{2v} symmetry of the thiophene ring. Therefore region with $s< 4.0$ must contain erroneous information or random noise that affects the data. When counting the standard deviations and the geometric model made with C_s geometry there is almost

no deviation from the higher symmetry of the ring. At first a flexible restraint was used for the difference between C(2)-C(3) and C(4)-C(5) but later this was removed as no change was observed using a tighter restraint. From GED, the ring core and the halogen position are well defined. Due to their small e.s.ds, no restraints were necessary to allow these ring parameters to refine to plausible values. A lot of information could be extracted from the experimental results enabling the refinement of almost all amplitudes. The overall *s* range used is considerably smaller for electron diffraction than the one used for the 2-chlorothiophene. It is because the phase shift for Br-C, Br-S and Br-H atoms pairs caused the scattering intensities to decay much more rapidly than for the corresponding compound, 2-chlorothiophene. Hence for 2-bromothiophene, there is an equal amount of random noise at s>250 nm^{-1} present but less signal, structural information.

The 2-chlorothiophene refinement was first carried out solely with flexible restraints. The resulting ring structure showed a little more distortion from the C_{2v} symmetry of thiophene than the bromo-substituted ring. The halogen bond length had to be paired with the S(1)-C distance since their difference is less than 1 pm. This avoids the use of a flexible restraint on the bond itself, but instead was applied to the difference. As with the previous structure the ring is well defined, with poor definition for the hydrogen positions. The use of the microwave spectroscopy data[14] reduced the e.s.ds but did not change the cage parameter. The microwave data considerably reduced the lengths of the hydrogen bonds, as previously seen for thiadiazole,[15] from an average of 112.4 pm to the more reasonable 109.6 pm, in **Table 4.9**.

For both structures only the average C-H bond length was allowed to refine freely. If the difference or individual hydrogen positions were allowed to refine, no information could be extracted, due to their small individual contributions to the overall scattering intensity.

Although good overall agreement within one or two e.s.ds is observed, there exists some discrepancy between the theoretical and experimental results. This difference is observed for both substituted thiophenes on the S-C bond length. The observed

distance was on average longer by 0.8 pm with respect to MP2/6-311+G(d,p). This difference is bigger for 2-chlorothiophene than for 2-bromothiophene. This could be due to the choice of parameter, where for chloro substitution p_1 is the average of both S-C and the C-Cl whereas for bromo substitution the halogen distance is refined on its own. For both structures there is a large e.s.d. on the C(3)-C(4) bond length. Although these distances are not as well defined as the rest of the parameters they do agree with the theory. All angles describing the core ring are well defined with reasonably small e.s.ds (<0.7°). The angles involving the positions of the hydrogen atoms are in better agreement with theory once the extra microwave data are used. For 2-chlorothiophene all C-C-H angles in the GED+MW refinement are 0.7° smaller than in the GED refinement, for example C(2)-C(3)-H(7) 123.3° (GED+MW) to 124.1° (GED).

In the early seventies arguments were made about the distortion of the thiophene ring from C_{2v} symmetry by mono-substitution.[1] This work shows that there are some noticeable changes in the ring, but these are nowhere near as large as stated then. Chlorine contributes more to the distortion of the ring than the bromide substitution. Today, better agreement between the model and the experimental data was achieved for both species.

Since the *ab initio* results already carried out prior to GED refinement show similar variation to those found experimentally, it was of interest to include the entire series of halogens. Therefore calculations were also carried out on 2-fluoro and 2-iodo thiophene at the MP2/6-311G(d) level. Full *ab initio* results and geometrical parameters can be found in appendix E on the CD. **Table 4.15** shows the difference between the two sides of the halogenated thiophenes.

Table 4.15: Influence of halogen substitution on thiophene ring.[a]

	MP2/6-311G(d)			
#	dif*r* SC[b]	dif*r* CC[c]	dif∠SCC[d]	dif∠CCC[e]
1 2-fluorothiophene	-0.2	-0.7	1.7	-2.4
2 2-chlorothiophene	0.2	-0.1	0.6	-1.2
3 2-bromothiophene	0.2	0.1	0.6	-1.2
4 2-iodothiophene	0.3	0.3	0.3	-1.0

[a] Difference in pm, angles in °

[b] Difference between S(1)-C(2) and S(1)-C(5)

[c] Difference between the carbon-carbon double bonds, C(2)-C(3) and C(5)-C(4)

[d] Difference between S(1)-C(2)-C(3) and S(1)-C(5)-C(4)

[e] Difference between C(2)-C(3)-C(4) and C(5)-C(4)-C(3)

Only in 2-fluorothiophene did the substituted side show a shorter S-C bond length than the other half: S(1)-C(2) is smaller than S(1)-C(5) by 0.2 pm. **1** also shows a difference of 0.7 pm in between C(2)-C(3) and C(5)-C(4). For the other compounds different behaviour is observed, all three showing S(1)-C(2) longer than S(1)-C(5) by 0.2 pm. The difference in the C-C bond is less noticeable for the less electronegative halogen substituents. There is, however, a turnover from chloro- to bromo-thiophenes when S(1)-C(2), shorter in **2,** becomes longer in **3**. It is important to notice that a similar effect is observed by GED. The biggest differences between of the angle defining the ring is attributed to **1** with a difference of 1.7° for S-C-C and -2.4° for C-C-C. The two compounds studied in this chapter both illustrate distorted ring features with identical differences.

Table 4.16: Bond and angle differences with respect to thiophene.[a]

		MP2/6-311G(d)			
	Parameters	2-Fluorothiophene	2-Chlorothiophene	2-Bromothiophene	2-Iodothiophene
Bonds	S(1)-C(2)	-0.8	-0.6	-0.5	-0.5
	S(1)-C(5)	-0.9	-0.4	-0.3	-0.2
	C(2)-C(3)	1.0	0.2	-0.1	-0.3
	C(5)-C(4)	0.4	0.1	0.1	0.0
Angles	S(1)C(2)C(3)	-2.3	-0.9	-0.8	-0.4
	S(1)C(5)C(4)	-0.5	-0.3	-0.2	-0.1
	C(2)C(3)C(4)	1.7	0.8	0.8	0.6
	C(3)C(4)C(5)	-0.7	-0.4	-0.4	-0.4

[a] distances in pm, angles in °

Table 4.16 contains a compilation of the difference between bond lengths and angles in the halogenated compounds and unsubstituted thiophene. All calculations related to thiophene can be found in appendix E on the CD. The use of this table emphasizes the point earlier made, that the biggest distortion of the ring from C_{2v} symmetry is with the fluoro substituent. Going down group 17 from F to I shows that the ring symmetry converges to that of thiophene.

In **Table 4.17** the differences in atomic charges, derived from the Mülliken populations, for the substituted thiophenes relative to the unsubstituted parent compound are displayed. Although they might not accurately represent the true atomic charges and are subject to basis set definition, they show the trend through substitution. The addition of a strong σ electron-withdrawing substituent, fluorine, on C(2) reduces its negative charge, consequently having the effect of increasing the C(2)-C(3) bond. Other halogenated substitutions have more benign effect on the charges of the ring.

Table 4.17: Atomic charge distribution in 2-substituted thiophenes relative to thiophene. (MP2/6-31G(d))

	thiophene	2-fluorothiophene	2-chlorothiophene	2-bromothiophene
S(1)	0.00	0.00	-0.06	-0.06
C(2)	0.00	-0.40	0.16	0.05
C(3)	0.00	0.05	-0.04	-0.04
C(4)	0.00	-0.02	-0.02	-0.01
C(5)	0.00	0.01	0.00	0.00
X(6)	0.00	0.36	-0.04	0.06

The calculated energies for the orbitals are in a good agreement with photoelectron spectroscopy results (**Table 4.18**). As expected, 2-fluorothiophene is the most stable of the halogen-substituted thiophenes with bromothiophene being the least stable.[6,7]

Table 4.18: Orbital energy for 2-substituted thiophene and thiophene.

	LUMO	HOMO	SHOMO
thiophene	3.57	-8.72	-9.30
2-fluorothiophene	3.48	-8.85	-9.79
2-chlorothiophene	3.08	-8.77	-9.75
2-bromothiophene	3.04	-8.70	-9.74

4.5 References

1. R. R. Karl, S. H. Bauer, *Acta Cryst.*, 1972, **B28**, 2619.
2. J. L. Derissen, J. W. M. Kocken, R. H. Van Weelden, *Acta Cryst.*, 1971, **B27**, 1692.
3. J. Kao, L. Radom, *J. Am. Chem. Soc.*, 1978, **101**, 311.
4. L. J. Saethre, T. D. Thomas, *J. Org. Chem.*, 1991, **51**, 3935.
5. T. H. Musslimani, H. Mettee, *J. Mol. Struct.*, 2004, **672**, 35.
6. A.B. Trofimov, J. Schirmer, D. M. P. Holland, L. Karlsson, R. Maripuu, K Siegbahn, A. W. Potts, *Chem. Phys.*, 2001, **263**, 167.
7. A.W. Potts, A. B. Tromfimov, J. Schirmer, D. M. P. Holland, L Karlson, , *Chem. Phys.*, 2001, **271**, 337.
8. Gaussian 98, Revision A.7, M. J. Frisch, G. W. Trucks, H. B. Schlegel, G. E. Scuseria, M. A. Robb, J. R. Cheeseman, V. G. Zakrzewski, J. A. Montgomery, R. E. Stratmann Jr, J. C. Burant, S. Dapprich, J. M. Millam, A. D. Daniels, K. N. Kudin, M. C. Strain, O. Farkas, J. Tomasi, V. Barone, M. Cossi, R. Cammi, B. Mennucci, C. Pomelli, C. Adamo, S. Clifford, J. Ochterski, G. A. Petersson, P. Y. Ayala, Q. Cui, K. Morokuma, D. K. Malick, A. D. Rabuck, K. Raghavachari, J. B. Foresman, J. Cioslowski, J. V. Ortiz, A. G. Baboul, B. B. Stefanov, G. Liu, A. Liashenko, P. Piskorz, I. Komaromi, R. Gomperts, R. L. Martin, D. J. Fox, T. Keith, M. A. Al-Laham, C. Y. Peng, A. Nanayakkara, C. Gonzalez, M. Challacombe, P. M. W. Gill, B. Johnson, W. Chen, M. W. Wong, J. L. Andres, C. Gonzalez, M. Head-Gordon, E. S. Replogle and J. A. Pople, Gaussian, Inc., Pittsburgh PA, 1998.
9. S. Cradock, J. Koprowski, D. W. H. Rankin, *J. Mol. Struct.*, 1981, **71**, 217.
10. S. L. Hinchley, H. E. Robertson, K. B. Borisenko, A. R. Turner, B. F. Johnston, D. W. H. Rankin, M. Ahmadian, J. N. Jones, A. H. Cowley, *Dalton Trans.* 2004, 2469.
11. A. W. Ross, M. Fink, R. Hilderbrandt, *International Tables for Crystallography*; A. J. C. Wilson, Ed.; Kluwer Academic Publishers: Dordrecht, The Netherlands, 1992; **Vol. C**, 245.
12. V. A. Sipachev, *J. Mol. Struct.*, 1985, **121**, 143.

13. I. V. Kochikov, Yu. I. Tarasov, V. P. Spiridonov, G. M. Kuramshina, D. W. H. Rankin, A. S. Saakjan and A. G. Yagola. *J. Mol. Struct.*, 2001, **567-568**, 29.
14. J. Mjoberg, S. Ljunggren, *Z. Naturforsch A.*, 1973, **28**, 729.
15. S. F. Bone, B. A. Smart, H. Gierens, C. A. Morrison, P. T. Brain, D. W. H. Rankin, *Phys. Chem. Chem. Phys.*, 1999, **1**, 2421.
16. A. J. Blake, P. T. Brain, H. McNab, J. Miller, C. A. Morrison, S. Parsons, D. W. H. Rankin, H. E. Robertson and B. A. Smart, *J. Phys. Chem.*, 1996, **100**, 12280; P. T. Brain, C. A. Morrison, S. Parsons and D. W. H. Rankin, *J. Chem. Soc., Dalton Trans.*, 1996, 4589; N. W. Mitzel and D. W. H. Rankin, *J. Chem. Soc., Dalton Trans.*, 2003, 3650.

Chapter 5

Molecular structures of 2,5-dichlorothiophene and 3,4-dichloro-1,2,5-thiadiazole, by the combined analysis of gas-phase electron diffraction data and by *ab initio* calculations.

5.1 Introduction

Thiadiazole and thiophene derivatives are isoelectronic to thiazole, pyrazines, and to six-membered heterocycles such as benzene. A very large number of derivatives is known today. Their applications are numerous and quite diverse. For instance they are being used in fields such as pharmaceuticals, dyes, polymers and agricultural chemicals such as pesticides. These heterocycles are being considered in novel areas like materials science via their potential applications in electronics, nonlinear optics, sensors, and liquid crystals. However whilst over the last two decades many derivatives were developed, no crystal structure determination has been carried out so far for either thiophene or 1,2,5-thidiazole. Only data originating from electron diffraction or from microwave experiments are available.[1-3] These two important parent species were investigated through extensive theoretical calculations and by photoelectron experiment.[4-7] No structural information exists for the two heterocycles studied in this chapter. One photoelectron experiment on 2,5-dichlorothiophene has however been published giving information on its electronic structure.[10] Because of the broad economic implications of all of the derivatives of these two molecules, it was decided to analyze the structural differences between 2,5-dichlorothiophene and 3,4-dichloro-1,2,5-thiadiazole and between their respective parent species. Gas phase electron diffraction and extensive *ab initio* calculations were performed on both these molecules in order to assess the effect of the nitrogenation (replacement of carbon by nitrogen) of the thiophene ring and of the di-substitution of the rings.

5.2 Experimental

5.2.1 Synthesis

Samples of 2,5-dichlorothiophene (98%) and 3,4-dichloro-1,2,5-thiadiazole (96%) were purchased from the Aldrich Chemical Co. and used without further purification.

5.2.2 *Ab initio*

The *ab initio* calculations were performed using the Gaussian 98 program[9] to obtain initial predictions of geometric and vibrational parameters, and vibrational corrections for the rotational constants.

For both di-halogenated derivatives of thiophene and of thiadiazole, the same methodologies and basis sets were used. At first the geometry optimisation was carried out in planar (C_{2v}) symmetry using the standard gradient techniques at the HF/3-21G(d) level. Further calculations were carried out with basis sets ranging from 6-31G(d) to 6-311+G(d,p) at HF and MP2 levels to investigate the basis effects. To look into the improvement of electron correlation calculations using HF, MP2, MP4(SDQ), and CISD methods were included all with the 6-31G(d) basis set. Since for thiophene density functional theory seems to perform reasonably well, B3LYP was used, with all conventional basis sets from 6-31G(d) to 6-311+G(3df,3pd) for both species. The atomic numbering for 2,5-dichlorothiophene and 3,4-dichloro-1,2,5-thiadiazole can be found in **Figure 5.1** and **Figure 5.2** respectively. Vibrational frequency calculations were carried out with the 6-31G(d) basis at HF and MP2 levels of theory as well as B3LYP, verifying that the C_{2v} model represents a true minimum on the potential energy surface.

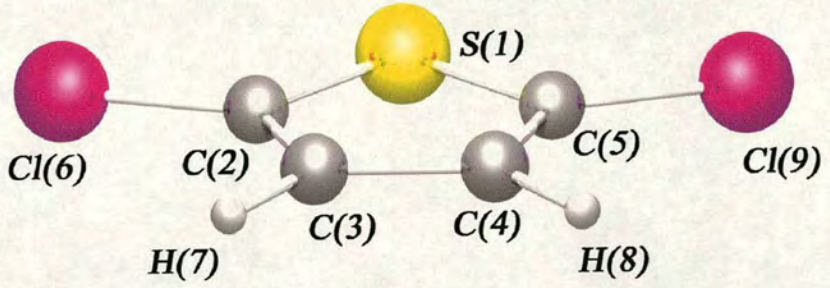

Figure 5.1: Molecular framework for 2,5-dichlorothiophene.

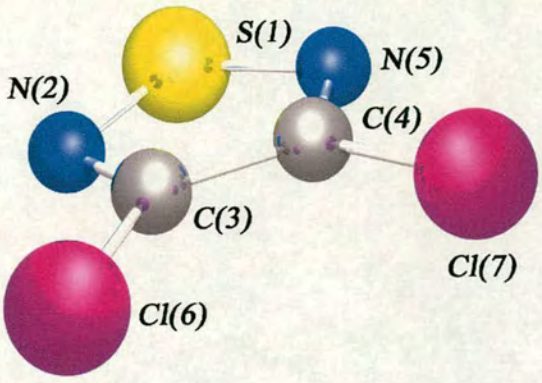

Figure 5.2: Molecular framework for 3,4-dichloro-1,2,5-thiadiazole.

5.2.3 Gas- phase electron diffraction

Electron diffraction data for both halogen-substituted thiophenes were obtained at two different distances using the Edinburgh apparatus. Data were recorded photographically on Kodak Electron Image plates, which were traced using a computer-controlled Joyce-Loebl MDM6 microdensitometer at the EPSRC Laboratory at Daresbury.[10] Four plates for long and three plates for short distances were studied for 2,5-dichlorothiophene, whereas three plates at both long and short distances were used for 3,4-dichloro-1,2,5-thiadiazole. Electron wavelengths were determined from the scattering pattern of benzene vapour recorded immediately after each thiophene run. The weighing points for the off-diagonal weight matrices, correlation parameters, and scale factors for the two camera distances are given in **Table 5.1**. The data reduction and analysis of the data were performed using ed@ed,[11] employing the scattering factors of Ross *et al.*[12]

Table 5.1: GED data analysis parameters for 2,5-dichlorothiophene and 3,4-dichloro-1,2,5-thiadiazole.

	2,5-dichlorothiophene		3,4-dichloro-1,2,5-thiadiazole	
camera distance/mm	262.96	97.63	258.29	91.81
T_{sample}/K	328	328	345	338
T_{nozzle}/K	391	352	368	373
Δs /nm^{-1}	2	4	2	4
s_{min}/nm^{-1}	40	100	20	132
sw_1/nm^{-1}	60	120	40	152
sw_2/nm^{-1}	130	288	132	288
s_{max}/nm^{-1}	152	336	154	336
correlation parameter	0.4267	0.2412	0.3874	0.3269
scale factor, k_a	0.851(5)	0.662(22)	0.986(10)	0.736(36)
electron wavelength /pm	6.02	6.02	6.02	6.02
a	1	2	1	2

On the basis of *ab initio* predictions structural refinements on 2,5-dichlorothiophene were carried out assuming C_{2v} symmetry (**Figure 5.1**). In total eight geometric parameters were employed, comprising four to define the core ring structure and a further four to define the hydrogen and chlorine atom positions. Parameters p_1 and p_3 define the average distance between S(1)-C(2) and C(2)-Cl(6), and their difference respectively. The bond distance C(2)-C(3) is defined by parameter p_2. The carbon hydrogen distance, C(3)-H(7) is described by p_4. p_5 defines the C(5)-S(1)-C(2) angle. The angle S(1)-C(2)-C(3) is described by p_6. The parameter describing the angles S(1)-C(2)-Cl(6) and C(2)-C(3)-H(7) are defined by p_7 and p_8 respectively.

On the basis of *ab initio* predictions structural refinements on 3,4-dichloro-1,2,5-thiadiazole were carried out assuming C_{2v} symmetry (**Figure 5.2**). In total six geometric parameters were employed, comprising four to define the core ring structure and two to define the chlorine atom positions. Parameters p_1 and p_3 define the average distance between S(1)-N(2) and C(3)-Cl(6), and their difference respectively. The bond distance N(2)-C(3) is defined by parameter p_2. p_4 defines the N(5)-S(1)-N(2) angle. The angle S(1)-N(2)-C(3) is described by p_5. Finally the parameter describing the angle N(2)-C(3)-Cl(6) is defined by p_6.

Although the starting geometry estimate was taken from the MP2/6-311+G(d,p) and MP2/6-311+G(df) level calculations for the disubstituted thiophene and thiadiazole respectively, the initial amplitudes of vibration (u) were obtained from the MP2(fc)/6-31G(d) force field, from which curvilinear corrections were extracted using the SHRINK program.[13] This level of theory for the force field was chosen since previously published thiophene structures revealed that MP2(fc)/6-31G(d) performed better than a higher basis set.

5.3 Results

5.3.1 *Ab initio*

Values of bond lengths and angles derived from calculations and electron diffraction measurements are presented in **Table 5.2** and **Table 5.3** for 2,5-dichlorothiophene and 3,4-dichloro-1,2,5-thiadiazole respectively. Other results from *ab initio* calculations are provided in appendix F on the attach CD.

Overall for both compounds studied, the predicted geometrical parameters are less affected by the definition of the basis set within the same level of theory than the calculation methods used, as previously observed for thiophene and mono-substituted halogenated thiophenes. As expected, the inclusion of electron correlation increases the multiple bond lengths within the ring. For 2,5-dichlorothiophene, the bond distance C(2)-C(3) increases by 3.4 pm from 134.0 pm at HF/6-31G(d) to 137.4 pm for MP2/6-31G(d). For 3,4-dichloro-1,2,5-thiadiazole, the increase for the multiple bonds is even greater (6.2 pm). In fact the bond distance N(2)-C(3) changes from 127.1 pm at HF/6-31G(d) to 133.3 pm at MP2/6-31G(d). Further improvement in the electron correlation treatment, as seen already in the previous chapter for the mono-substituted thiophene, results in an increase of 2.2 pm at MP4(SDQ)/6-31G(d) and an even smaller change of 0.9 pm for CISD/6-31G(d) with respect to the self-consistent field theory. Once again for the substituted thiadiazole the inclusion of more electron correlation has a drastic effect; the N(2)-C(3) bond length is increased by 3.6 pm at MP4(SDQ)/6-31G(d) and a change of 1.8 pm is observed for CISD/6-

31G(d) with respect to Hartree Fock. The S(1)-C(2) distance in the disubstituted thiophene shows perfect agreement between the CISD and MP2 whereas at the MP4 level this bond is 1.3 pm longer. Almost no changes are observed for the C(2)-Cl(6) bond through all the methodology employed. Although the C(2)-S(1)-C(5) angle has a difference of 0.6° with the 6-31G(d) basis set between HF and MP2, inclusion of more electron correlation leaves this angle unaffected, a direct consequence of the C(4)-C(3) length being constant. All other angles describing the core ring have converged with respect to the increase in electron correlation methodology. The angles describing the chlorine and hydrogen positions are fairly constant and therefore have also converged with respect to theory. Calculations for 3,4-dichloro-1,2,5-thiadiazole revealed that once again there is no convergence with respect to involvement of electron correlation. A positive difference of 0.6 pm is observed for the C(3)-Cl(6) passing from HF to MP4 whereas passing from HF to CISD going through MP2 the bond distance decreases by 0.4 pm. In contrast to the thiophene substitution, all angles are affected strongly by the inclusion of electron correlation, directly linked to the C(3)-C(4) bond distances. The biggest variation is observed for N(2)-S(1)-N(5), with a difference of 2.8°, 1.2° and 0.7° from HF to MP2, MP4 and CISD respectively. Whereas little variation is observed for the halogens angles in the thiophene substituted complexes, in the thiadiazole derivatives considerable variations are noticed. These differences are, however, smaller than in self consistent field theory.

In both heterocycles under investigation, passing from 6-31G(d) to 6-311G(d), little variation is observed in most of the parameters describing the ring, emphasizing a convergence in basis set. The addition of extra s and p functions only affects the bond involving the sulfur atoms, S(1)-C(2) being decreased by 0.4 pm whereas S(1)-N(2) is shortened by 0.8 pm in 2,5-dichlorothiophene and 3,4-dichloro-1,2,5-thiadiazole respectively.

The addition of two d type and one f type functions to the 6-311+G(d,p) basis set reduced all the core ring bond lengths in 2,5-dichlorothiophene especially those involving sulphur and the chlorine substituents. The C(2)-Cl(6) bond is reduced by

1.0 pm and C(2)-S(1) shrinks by 1.1 pm from MP2/6-311+G(d,p) to MP26-311+G(3df,3pd).

For 3,4-dichloro-1,2,5-thiadiazole, the addition of one f type function to the 6-311+G(d) basis set reduced all the core ring bond lengths, especially those involving sulfur and the one involving the halogen substituent, as for the thiophene substituents. The S(1)-N(2) bond is reduced by 1.3 pm while C(3)-Cl(6) shrinks by 0.6 pm from MP2/6-311+G(d) to MP2/6-311+G(df). A further addition of two extra d type functions has no effect with respect to the previous variation except for the bond S(1)-N(2), which is further shortened by 1 pm. On the other hand N(2)-C(3) at this basis set is back to the result found with 6-311+G(d).

The addition of diffuse functions has practically no effect on the description of the ring or of the halogenated substituents. At most, a variation of 0.2 pm is observable for C(3)-Cl(6) in 3,4-dichloro-1,2,5-thiadiazole.

The B3LYP level of theory in 2,5-dichlorothiophene overestimates the S(1)-C(2) distance by 1.9 pm, C(4)-C(3) by 1.1 pm and C(2)-Cl(6) by 1.3 pm with respect to MP2, while the multiple bond is shorter by 0.9 pm. In the disubstituted thiadiazole, similar divergences are observed to those of the thiophene derivatives. Hence, while the S(1)-N(2) distance is overestimated by 1.7 pm, C(3)-Cl(6) by 1.6 pm and C(3)-C(4) by 2.6 pm, N(2)-C(3) is smaller by 2.7 pm with respect to MP2. Whereas all ring core angles have no significant divergence from MP2 for 2,5-dichlorothiophene, the N(2)-S(1)-N(5) angle in 3,4-dichloro-1,2,5-thiadiazole is 98.1° by DFT in comparison to 99.5° by MP2.

Table 5.2: Calculated (r_e) and experimental (r_{h1}) structures of 2,5-dichlorothiophene.

	Level of theory/ basis set										
	HF		MP2				MP4	CISD	B3LYP		GED
	6-31G(d)	6-311+G(d,p)	6-31G(d)	6-311G(d)	6-311+G(d)	6-311+G(d,p)	6-31G(d)	6-31G(d)	6-31G(d)	6-311+G(3df,3pd)	
S(1)-C(2)	173.3	173.2	172.9	172.5	172.6	172.5	174.2	172.9	174.8	173.2	173.0(6)
C(2)-C(3)	134.0	133.9	137.4	137.7	137.8	137.8	136.2	134.9	136.5	136.0	136.9(4)
C(4)-C(3)	143.8	143.9	141.9	142.0	142.1	142.1	143.5	143.0	143.0	142.3	143.5(8)
C(2)-Cl(6)	171.9	172.1	171.8	171.7	171.7	171.6	172.4	171.5	173.1	171.8	171.5(6)
C(3)-H(7)	107.2	107.2	108.5	108.4	108.5	108.4	108.5	107.7	108.4	107.9	107.7(8)
C(2)-S(1)-C(5)	89.8	89.8	90.4	90.5	90.6	90.6	89.8	90.0	89.9	90.4	90.2(2)
S(1)-C(2)-C(3)	113.0	113.0	112.7	112.8	112.7	112.7	113.0	113.0	112.6	112.4	113.1(4)
C(2)-C(3)-C(4)	112.1	112.1	112.1	112.0	112.0	112.0	112.1	112.1	112.4	112.4	111.8(3)
S(1)-C(2)-Cl(6)	120.2	120.1	120.4	120.5	120.6	120.6	120.1	120.2	120.3	120.3	119.8(1)
C(2)-C(3)-H(7)	123.8	123.8	123.1	122.9	122.9	122.9	123.5	123.6	123.4	123.4	121.6(9)

[a] distances in pm, angles in °

Table 5.3: Calculated (r_e) and experimental (r_{h1}) structures of 3,4-dichloro-1,2,5-thiadiazole.

	Level of theory/ basis set										
	HF		MP2				MP4	CISD	B3LYP		GED
	6-31G(d)	6-311+G(d)	6-31G(d)	6-311G(d)	6-311+G(d)	6-311+g(df)	6-31G(d)	6-31G(d)	6-31G(d)	6-311+G(3df)	
S(1)-N(2)	164.2	164.1	165.0	164.2	164.3	163.1	166.5	164.2	166.7	162.3	164.2(2)
N(2)-C(3)	127.1	126.8	133.3	133.1	133.2	132.9	130.7	128.9	130.6	133.4	131.5(2)
C(3)-C(4)	145.1	145.3	142.2	142.3	142.3	141.9	144.6	144.0	144.6	141.3	143.4(5)
C(3)-Cl(6)	171.0	171.2	170.9	170.8	170.6	169.9	171.6	170.6	172.5	169.7	170.6(2)
N(2)-S(1)-N(5)	96.7	96.5	99.5	99.6	99.5	100.0	97.9	97.4	98.1	100.3	99.1(2)
S(1)-N(2)-C(3)	108.5	108.6	106.0	106.2	106.2	106.0	107.0	107.8	106.7	106.0	106.6(2)
N(2)-C(3)-C(4)	113.2	113.1	114.3	114.0	114.1	114.0	114.0	113.5	114.2	113.9	113.9(1)
N(2)-C(3)-Cl(6)	122.5	122.6	120.9	121.2	121.1	121.3	121.7	122.1	121.6	121.4	121.5(2)

[a] distances in pm, angles in °

5.3.2 Gas-phase electron diffraction

The model used for the GED refinement of 2,5-dichlorothiophene was based upon the geometry obtained from the optimised *ab initio* calculations. The least-squares refinement of the structure resulted in an R_G factor of 0.095 (R_D = 0.067), with optimized parameters listed in **Table 5.4** and dependent parameters in **Table 5.5**. A summary of final bond distances and amplitudes of vibration is presented in **Table 5.6**. Eight geometrical parameters and eight groups of amplitudes of vibration were refined. Flexible restraints were employed during the refinement using the SARACEN method.[15] Altogether, two geometric and one amplitude restraints were employed. These are listed in **Table 5.7**. For a full list of the final bond distances and amplitudes of vibration, see appendix F on the CD. The least-squares correlation matrix for the structural refinement is labelled **Table 5.8**. The success of the final refinement can be assessed on the basis of the molecular scattering curves, **Figure 5.3**, and radial distribution curve **Figure 5.4**.

Table 5.4: Geometrical parameters (r_{h1}) for 2,5-dichlorothiophene.[a,b]

	Parameter	GED	MP2/6-311+G(d,p)
p_1	av*r* S(1)C(2)*r* C(2)Cl(6)	172.27(9)	172.1
p_2	*r* C(2)C(3)	136.9(4)	137.8
p_3	dif*r* S(1)C(2)*r* C(2)Cl(6)	1.55(10)	0.9
p_4	*r* C(3)H(7)	107.7(8)	108.4
p_5	∠C(5)S(1)C(2)	90.2(2)	90.6
p_6	∠S(1)C(2)C(3)	113.1(4)	112.7
p_7	∠S(1)C(2)Cl(6)	119.8(1)	120.6
p_8	∠C(2)C(3)H(7)	121.6(9)	122.9

[a] distances in pm, angles in °

[b] see text for parameter definitions

Table 5.5: Dependent parameters (r_{h1}) for 2,5-dichlorothiophene.[a]

	Parameter	GED	MP2/6-311+G(d,p)
d_1	rS(1)C(2)	173.0(6)	172.5
d_2	rC(2)Cl(6)	171.5(6)	171.6
d_3	rC(3)C(4)	143.5(8)	142.1
d_4	∠C(2)C(3)C(4)	111.8(3)	112.0

[a] distances in pm, angles in °

Table 5.6: Bond distances (r_a/pm) and amplitudes of vibration (u/pm) obtained in the GED refinement of 2,5-dichlorothiophene.

u	Atom pair	r_a	Amplitude	
u_1	S(1)-C(2)	172.9(6)	4.2	Tied to u_3
u_2	C(2)-C(3)	137.0(4)	3.5(7)	
u_3	C(2)-Cl(6)	171.5(6)	4.1(2)	
u_4	C(3)-C(4)	143.7(7)	3.8	Tied to u_2
u_6	S(1)...C(3)	259.2(3)	5.2(5)	
u_7	S(1)...Cl(6)	297.6(2)	7.0(2)	
u_9	C(2)...C(4)	232.0(3)	4.9(5)	
u_{10}	C(2)...C(5)	244.8(10)	5.2	Tied to u_9
u_{13}	C(2)...Cl(9)	411.9(5)	6.8	Tied to u_{16}
u_{14}	C(3)...Cl(6)	275.8(3)	5.0(5)	
u_{16}	C(3)...Cl(9)	397.9(4)	6.6(7)	
u_{17}	Cl(6)...H(7)	298.9(18)	14.3	Tied to u_7
u_{19}	Cl(6)...Cl(9)	574.0(3)	8.6(5)	

Table 5.7: Flexible restraints used in GED refinement for 2,5-dichlorothiophene.

Restraints	Value /pm or °	Uncertainty /pm or °
∠C(2)C(3)H(7)	122.9	1.0
rC(3)H(7)	108.4	1.0
u_9	5.4	0.5

Table 5.8: Least-squares correlation matrix (x100) for GED structure refinement of 2,5-dichlorothiophene.[a]

	p_5	p_6	p_7	u_2	u_{14}	u_{16}	k_2
p_1			-64				
p_2		-54		65			
p_3	52	-93				-69	
p_5		-68					
p_6						71	
u_3							75
u_6					61		
u_7							56

[a] Only elements with the absolute values > 50% are shown; k_2 is a scale factor.

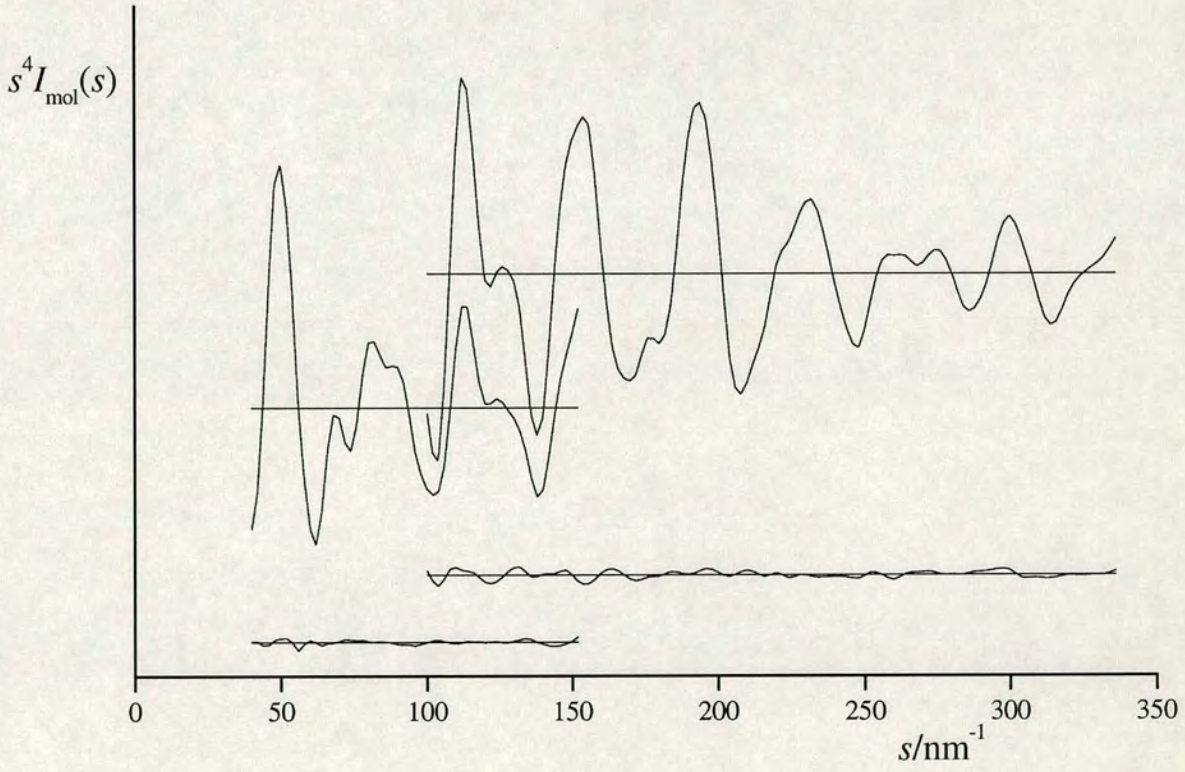

Figure 5.3: Experimental and final weighted difference (experimental-theoretical) molecular scattering intensities for 2,5-dichlorothiophene.

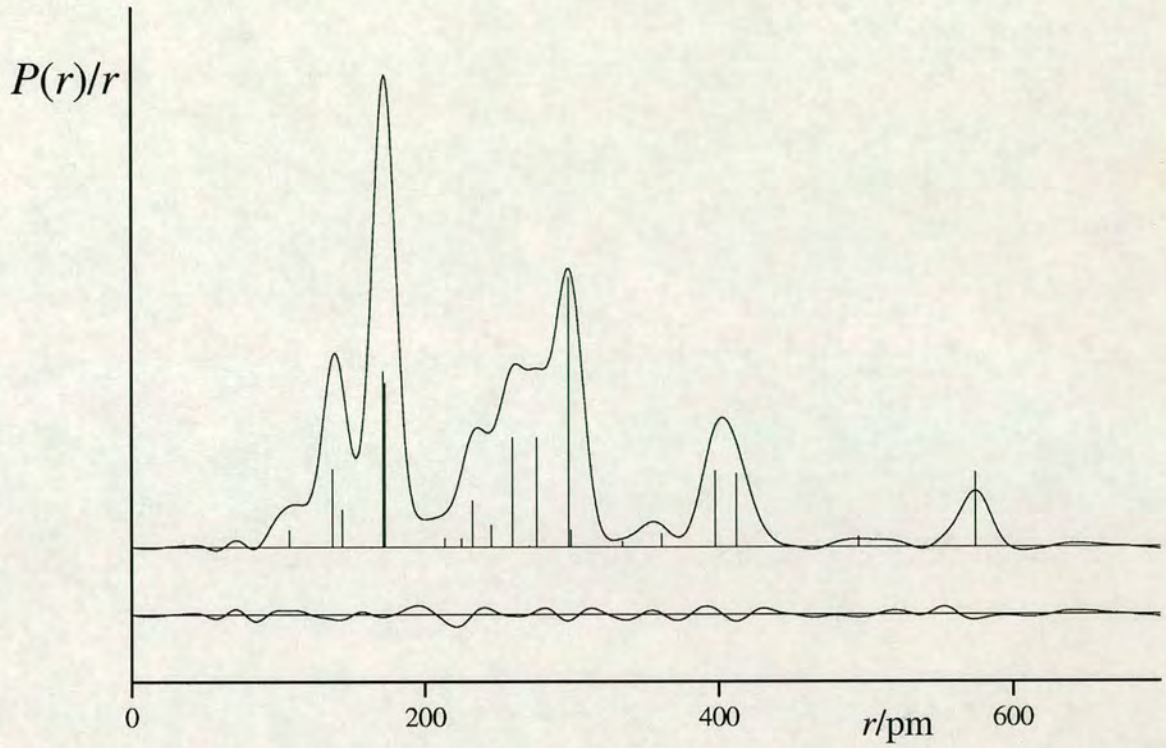

Figure 5.4: Experimental and difference (experimental – theoretical) radial distribution curves, $P(r)/r$, for 2,5-dichlorothiophene. Before Fourier inversion, the data were multiplied by $s.\exp(-0.00002s^2)/(Z_S\text{-}f_S)(Z_{Cl}\text{-}f_{Cl})$

The model used for the GED refinement of 3,4-dichloro-1,2,5-thiadiazole was based upon the geometry obtained from the optimised *ab initio* calculations. The least-squares refinement of the structure resulted in an R_G factor of 0.059 (R_D = 0.042), with optimized parameters listed in **Table 5.9** and dependent parameters can be found in **Table 5.10**. A summary of final bond distances and amplitudes of vibration are recorded in **Table 5.11**. Six geometrical parameters and six groups of amplitudes of vibration were refined. No flexible restraints were employed during the refinement using since all amplitudes and parameters were well defined. For a full list of the final bond distances and amplitudes of vibration, see appendix F on the CD. The least-squares correlation matrix for the structural refinement is labelled **Table 5.12**. The success of the final refinement can be assessed on the basis of the molecular scattering curves, **Figure 5.5,** and radial distribution curve **Figure 5.6**.

Table 5.9: Geometrical parameters (r_{h1}) for 3,4-dichloro-1,2,5-thiadiazole.[a,b]

	Parameter	GED	MP2/6-311+G(df)
p_1	av$r$ SNr CCl	167.41(8)	166.5
p_2	r NC	131.5(2)	132.9
p_3	dif$r$ SNr CCl	6.5(3)	6.8
p_4	∠NSN	99.1(2)	100.0
p_5	∠SNC	106.6(2)	106.0
p_6	∠NCCl	121.5(2)	121.3

[a] distances in pm, angles in °

[b] see text for parameter definitions

Table 5.10: Dependent parameters (r_{h1}) for 3,4-dichloro-1,2,5-thiadiazole.[a]

	Parameter	GED	MP2/6-311+G(df)
d_1	r CC	143.4(5)	141.9
d_2	r SN	164.2(2)	163.1
d_3	r CCl	170.6(2)	169.9
d_4	∠NCC	113.9(1)	114.0

[a] distances in pm, angles in °

Table 5.11: Bond distances (r_a/pm) and amplitudes of vibration (u/pm) obtained in the GED refinement of 3,4-dichloro-1,2,5-thiadiazole.

u	Atom pair	r_a	Amplitude	
u_1	S(1)-N(2)	164.1(2)	5.1(3)	
u_2	N(2)-C(3)	131.5(2)	3.7(7)	
u_3	C(3)-C(4)	143.4(5)	4.0	Tied to u_2
u_4	C(3)-Cl(6)	170.6(2)	4.9	Tied to u_1
u_5	S(1)...C(3)	237.6(2)	4.7(4)	
u_6	S(1)...Cl(6)	403.2(1)	6.5(3)	
u_7	N(2)...N(5)	249.8(5)	5.5	Tied to u_5
u_8	N(2)...C(4)	230.3(4)	5.1	Tied to u_5
u_9	N(2)...Cl(6)	264.1(2)	5.8(4)	
u_{10}	N(2)...Cl(7)	391.7(3)	7.1	Tied to u_6
u_{11}	C(3)...Cl(7)	277.8(2)	6.0	Tied to u_9
u_{12}	Cl(6)...Cl(7)	336.1(4)	10.9(4)	

Table 5.12: Least-squares correlation matrix (x100) for GED structure refinement of 3,4-dichloro-1,2,5-thiadiazole.[a]

	p_4	p_5	u_5	u_6	k_1	k_2
p_1		-53				
p_2	55	-61				
p_4	100	-88				
u_1			55	58	62	80
u_2						62
u_5				59	52	67
u_6					61	69
k_1						71

[a] Only elements with the absolute values > 50% are shown; k_2 and k_1 are scales factor.

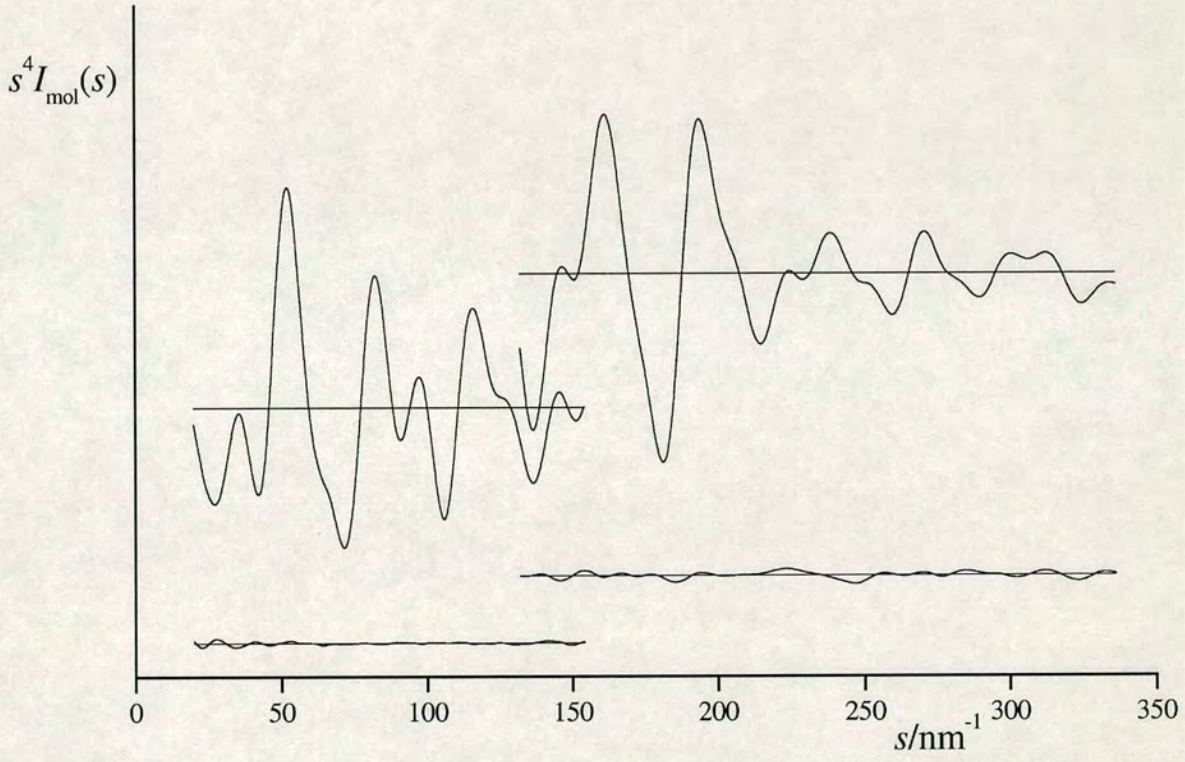

Figure 5.5: Experimental and final weighted difference (experimental-theoretical) molecular scattering intensities for 3,4-dichloro-1,2,5-thiadiazole.

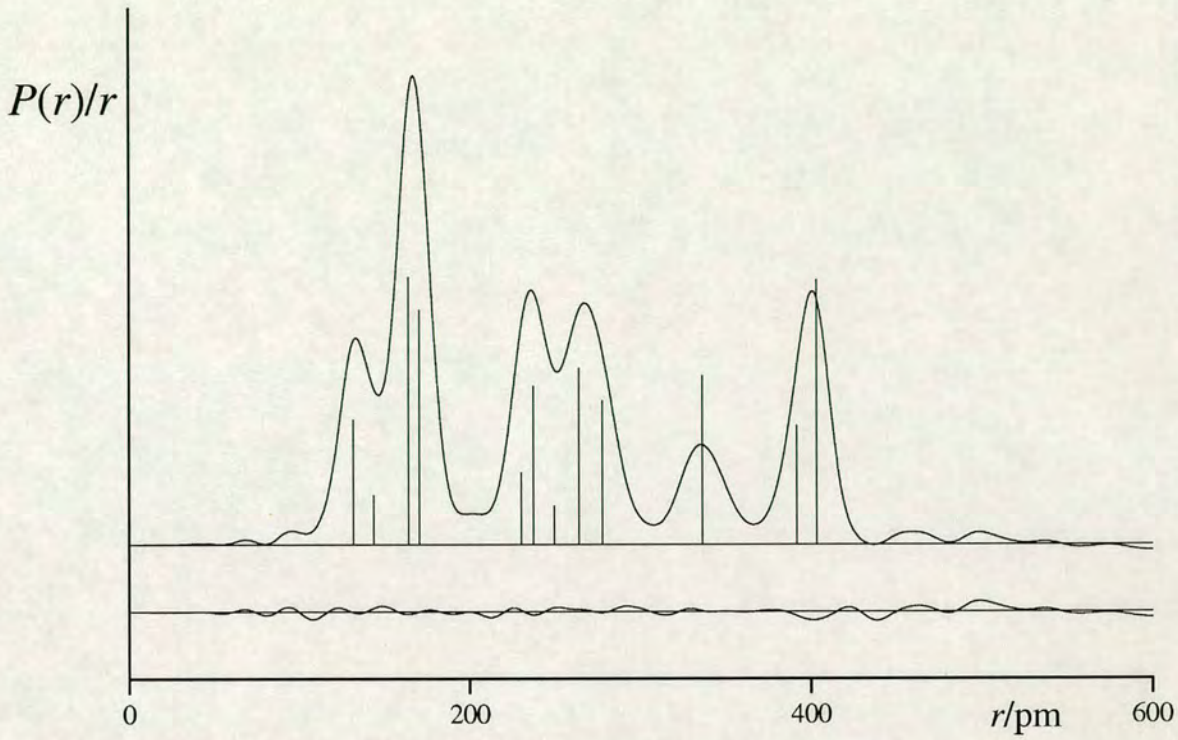

Figure 5.6: Experimental and difference (experimental – theoretical) radial distribution curves, $P(r)/r$, for 3,4-dichloro-1,2,5-thiadiazole. Before Fourier inversion, the data were multiplied by $s.\exp(-0.00002s^2)/(Z_S\text{-}f_S)(Z_{Cl}\text{-}f_{Cl})$

5.4 **Discussion**

Experimental results agree with the predicted geometry and their trends are well defined. For both structures the biggest difference from theory (MP2) is observed for the C(3)-C(4) bond with a 1.4 pm lengthening. This could be due to poor definition of electron correlation with the MP2 method. In fact, as stated previously, the inclusion of more electron correlation does have the effect of lengthening this bond, which then becomes comparable to GED within one esd. The MP2 bond lengths are however, not necessarily wrong since they both agree with the GED data to within two esds.

The R_G factor is slightly higher for 2,5-dichlorothiophene than for 3,4-dichloro-1,2,5-thiadiazole. This can be explained by the presence of random noise, which can not be taken into account during the refinement. There is no discrepancy, however, in the

precision of the parameters as seen in **Figure 5.3** and **Figure 5.4**. The difference curve below the bonding region, *r* less than 100 pm, and beyond the largest intermolecular distance of the molecule, *r* greater than 560 pm, in **Figure 5.4**, is characteristic of random noise. The constant wave nature of the difference curves, under the radial distribution, shows that at no point was the noise fitted by the structure. To a lesser extent similar noise is observed in the refinement of 3,4-dichloro-1,2,5-thiadiazole.

In order to investigate the effect of the addition of more electron-withdrawing groups on the disubstituted thiophene ring, *ab initio* calculations were carried out on 2,5-difluorothiophene, **Table 5.13**. A summary of calculations on 3,4-dichlorothiophene can be found in **Table 5.14**. This allows assessment of the effect of introduction of nitrogen atoms in the ring in 3,4-dichloro-1,2,5-thiadiazole. Full results can be found in appendix F on the CD.

Table 5.13: Calculated (r_e) structure of 2,5-difluorothiophene.

	Level of theory/ basis set					
	HF		MP2		B3LYP	
	6-31G(d)	6-311G(d,p)	6-31G(d)	6-311+G(d,p)	6-31G(d)	6-311+G(3df,3pd)
S(1)-C(2)	173.8	173.7	173.6	173.2	175.5	173.8
C(2)-C(3)	133.1	133.0	136.3	136.5	135.5	135.0
C(4)-C(3)	144.8	144.9	143.1	143.3	143.9	143.4
C(2)-Cl(6)	131.6	131.2	134.4	133.7	133.5	133.2
C(3)-H(7)	107.2	107.2	108.3	108.3	108.3	107.8
C(2)-S(1)-C(5)	88.3	88.3	88.5	88.6	88.3	88.6
S(1)-C(2)-C(3)	114.5	114.5	114.5	114.5	114.1	114.1
C(2)-C(3)-C(4)	111.4	111.4	111.3	111.2	111.8	111.6
S(1)-C(2)-Cl(6)	118.1	118.2	118.4	118.6	118.3	118.7
C(2)-C(3)-H(7)	123.8	123.9	123.3	123.3	123.4	123.6

[a] distances in pm, angles in °

Table 5.14: Calculated (r_e) structure of 3,4-dichlorothiophene.

	Level of theory/ basis set							
	HF		MP2				B3LYP	
	6-31G(d)	6-311+G(d,p)	6-31G(d)	6-311G(d)	6-311+G(d)	6-311+G(d,p)	6-31G(d)	6-311+G(3df,3pd)
S(1)-C(2)	172.2	172.1	171.4	171.0	171.1	171.0	173.3	171.5
C(2)-C(3)	134.2	134.1	137.5	137.8	138.0	138.0	136.5	136.2
C(2)-H(6)	107.0	107.0	108.2	108.2	108.2	108.1	108.1	107.6
C(3)-C(4)	144.0	143.9	142.4	142.3	142.4	142.4	143.6	142.8
C(3)Cl(7)	172.3	172.5	172.1	171.9	171.8	171.8	173.7	172.3
C(2)-S(1)-C(5)	91.6	91.6	92.4	92.4	92.5	92.5	91.9	92.3
S(1)-C(2)-C(3)	111.7	111.6	111.4	111.5	111.4	111.5	111.3	111.3
S(1)-C(2)-H(6)	121.3	121.3	121.3	121.3	121.3	121.3	121.1	121.2
C(2)-C(3)-C(4)	112.5	112.6	112.5	112.3	112.3	112.3	112.7	112.6
C(2)-C(3)-Cl(7)	123.8	123.8	123.6	123.7	123.7	123.7	123.6	123.8

[a] distances in pm, angles in °

Because a direct experimental comparison could not be carried out between 3,4-dichloro-1,2,5-thiadiazole and 3,4-dichlorothiophene due to the non-availability of this latter compound, theoretical results were used. All the thio-aromatic ring calculations carried out have so far agreed extremely well with the experimental results, and so it seems reasonable to assume that the conclusions drawn from *ab initio* will reflect the experimental behaviour. In a fashion similar to that described previously, thiophene and thiadiazole[1] were compared to their 3,4-halogen derivatives. The addition of the two nitrogens into the 3,4-dichlorothiophene ring has little effect. In fact the C(3)-C(4) difference between both rings at 6-311+G(d,p)/MP2 is only of the order of 0.5 pm. In both cases these distances are longer than that observed in benzene (139.7 pm) and shorter than that in cylcopentadiene (146 pm).

Table 5.15 : Influence of halogen substitution on thiophene and thiadiazole ring (in pm and °).

	MP2/6-311+G(d,p)					
#	dif*r* SX	dif*r* XC	dif*r* CC	dif∠XSX	dif∠SXC	dif∠XCC
1 3,4-dichlorothiophene	0.2	0.2	-0.3	-0.3	0.2	-0.1
2 2,5-dichlorothiophene	-1.3	0.4	0.0	1.5	-1.0	0.2
3 2,5-difluorothiophene	-1.9	1.7	-1.2	3.5	-2.8	1.0
4 3,4-dichloro-1,2,5-thiadiazole	-0.4	1.3	-1.3	0.1	0.0	0.0

A full investigation on the divergence of the ring geometry for both heterocycle derivatives is summarized in **Table 5.15**. The divergences of the rings are defined with respect to their parents' species. Therefore the di-halogenated substituted thiophene rings and 3,4-dichloro-1,2,5-thidiazole are compared to thiophene and 1,2,5-thidiazole respectively. dif*r*SC corresponds to the variation in the bond length of the bonded sulfur to its neighbouring atom X(2), carbon in thiophene and nitrogen in thiadiazole. dif*r*XC and dif*r*CC are the bond lengths X(2)-C(3) and C(3)-C(4) respectively. The difference of the three angles in the C_{2v} ring, X(2)-S(1)-X(5), S(1)-X(2)-C(3) and X(2)-C(3)-C(4) are represented by dif∠XSX, dif∠SXC and dif∠XCC. The biggest deformations are observed for the 2,5-halo-thiophenes with a bigger effect seen with fluorine substitution. The S(1)-C(2) bond distance increases

by almost 2 pm for the fluorothiophene with respect to its parent. The sp^2 carbon bound to the halogen is well known to be electron deficient. Therefore the carbon bound to the sulfur atom will carry a positive charge. Therefore the two atoms will share the same sign and will repel each other, consequently increasing S(1)-C(2). This effect is more evident for fluorine, a better electron-withdrawing substituent than chlorine. It was noted that, whereas in **2** there are barely any changes in the parameters C(2)-C(3) and C(3)-C(4), in **3** they are shorter by 1.7 pm and longer by 1.2 pm respectively. The effect of the electron delocalization of the ring is observed all over the ring, with a bigger difference for **3.** While the angle C(2)-S(1)-C(2) shrinks by 3.5°, S(1)-C(2)-C(3) increases by 2.8°. For **1** no major difference is observed with respect to its parent. The difference in bond length for the sulfur–carbon bond can be explained using the resonance forms previously employed for the reaction mechanism of 2,5 vs. 3,4-halothiophene.[14]

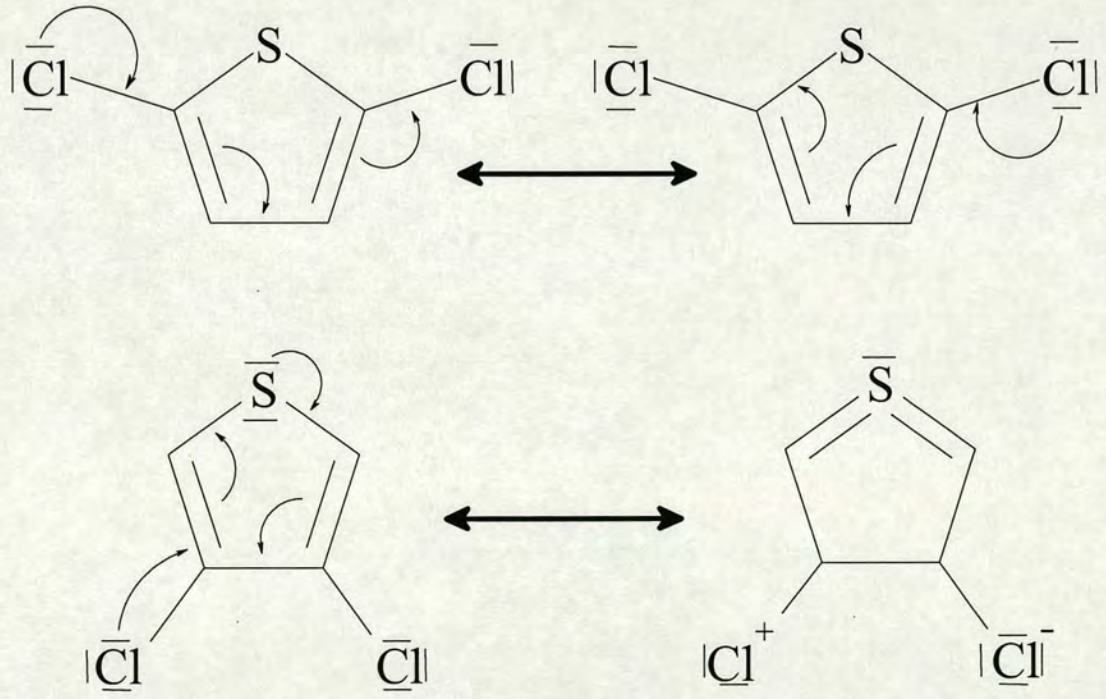

Figure 5.7: Resonance forms of 2,5-dichlorothiophene and 3,4-dichlorothiophene.

4 shows only observable differences in the bonds length of the ring with respect to 1,2,5-thiadiazole, while the halogen-substitution leaves the ring angles unchanged. In fact, the halogen substituent shortens N(2)-C(3) and lengthens C(3)-C(4). It is due to the electron-withdrawing property of the substituent giving a more positive partial charge on C(3). Knowing that partial charges on nitrogen are negative it has the direct consequence of increasing the attraction between these two poles, resulting in a shorter bond length N(2)-C(3). C(4) and C(3) possess the same charge and repel one another. All these interactions are summarized by **Figure 5.8**.

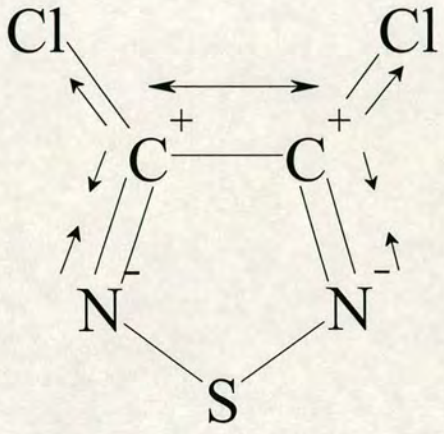

Figure 5.8: Charge delocalization of 3,4-dichloro-1,2,5-thiadiazole with respect to thiadiazole

The calculated energies for the orbitals are in good agreement with the photoelectron spectroscopy results for 2,5-dichloro-thiophene.[8] (**Table 5.16**). In agreement with previous exoerimental results,[16] via *ab initio* it was confirmed that 3,4-dichlorothiophene is more stable than 2,5-dichlorothiophene. In accordance with the trends observed for the mono-substituted compound, the addition of fluorines to the thiophene ring stabilizes the species more than chlorines do. The addition of two chlorines onto thiadiazole destabilizes the ring.

Table 5.16: Orbital energies, in eV, for dihalo-thiophene derivatives and dihalo-thiadiazole derivatives.

	LUMO	HOMO	SHOMO
thiophene	3.57	-8.71	-9.30
2,5-difluorothiophene	3.41	-9.02	-10.26
2,5-dichlorothiophene	2.65	-8.83	-10.17
3,4-dichlorothiophene	2.75	-9.29	-9.57
1,2,5-thiadiazole	2.01	-10.12	-11.44
3,4-dichloro-1,2,5-thiadiazole	1.31	-10.22	-11.77

Although both rings share the same trends in the energy stabilization, the composition of their HOMO and SHOMO orbitals are different. In fact, these two orbitals are swapped. The HOMO in 3,4-dichloro-1,2,5-thidiazole consists of π C(3)-C(4), $3p_z$ S(1) and $3p_z$ Cl(6), whereas in 3,4-dichlorothiophene it includes π C(2)-C(3), C(5)-C(4) and $3p_z$ Cl(6). On the other hand, the SHOMO for thiadiazole has contributions from π N(2)-C(3) and $3p_z$ Cl(6) and in the thiophene ring π C(4)-C(3) and $3p_z$ S(1).

If further investigation of thiophenes or the thiadiazole ring were to be instigated MP2/6-31G(d) would be sufficient. However, if no computing cost constraints existed, it would be better to use a larger basis set than to use any of the higher correlation methods due to their poor convergences. If computing cost is critical, B3LYP/6-311G(3df,3pd) should be chosen as its costs are a fraction of those using the second order Møller-Plesset method.

5.5 References

1. F. A. Momany, R. A. Bonham, *J. Am. Chem. Soc.*, 1961, **83**, 4475; 1964, **86**, 162.
2. Sr. V. Dobyns, L. Pierce, *J. Am. Chem. Soc..*, 1963, **85**,3553.
3. I. V. Kochikov, Yu. I. Tarasov, V. P. Spiridonov, G. M. Kuramshina, D. W. H. Rankin, A. S. Saakjan and A. G. Yagola. *J. Mol. Struct.*, 2001, **567-568**, 29-40.
4. M. D. Glossman, A. L. Marquez, *J. Mol. Struc.*, 2001, **548**, 153.
5. M. D. Glossman, *J. Mol. Struc.*, 2003, **634**, 77.
6. A.B. Trofimov, J. Schirmer, D. M. P. Holland, L. Karlsson, R. Maripuu, K Siegbahn, A. W. Potts, *Chem. Phys.*, 2001, **263**, 167.
7. A.W. Potts, A. B. Tromfimov, J. Schirmer, D. M. P. Holland, L Karlson, *Chem. Phys.*, 2001, **271**, 337.
8. A. D. Baker, D. Betteridge, N. R. Kemp, R. E. Kriby, *Anal. Chem.*, 1970, **42**, 1064.
9. Gaussian 98, Revision A.7, M. J. Frisch, G. W. Trucks, H. B. Schlegel, G. E. Scuseria, M. A. Robb, J. R. Cheeseman, V. G. Zakrzewski, J. A. Montgomery, R. E. Stratmann Jr, J. C. Burant, S. Dapprich, J. M. Millam, A. D. Daniels, K. N. Kudin, M. C. Strain, O. Farkas, J. Tomasi, V. Barone, M. Cossi, R. Cammi, B. Mennucci, C. Pomelli, C. Adamo, S. Clifford, J. Ochterski, G. A. Petersson, P. Y. Ayala, Q. Cui, K. Morokuma, D. K. Malick, A. D. Rabuck, K. Raghavachari, J. B. Foresman, J. Cioslowski, J. V. Ortiz, A. G. Baboul, B. B. Stefanov, G. Liu, A. Liashenko, P. Piskorz, I. Komaromi, R. Gomperts, R. L. Martin, D. J. Fox, T. Keith, M. A. Al-Laham, C. Y. Peng, A. Nanayakkara, C. Gonzalez, M. Challacombe, P. M. W. Gill, B. Johnson, W. Chen, M. W. Wong, J. L. Andres, C. Gonzalez, M. Head-Gordon, E. S. Replogle and J. A. Pople, Gaussian, Inc., Pittsburgh PA, 1998.
10. S. Cradock, J. Koprowski, D. W. H. Rankin, *J. Mol. Struct.*, 1981, **71**, 217.
11. S. L. Hinchley, H. E. Robertson, K. B. Borisenko, A. R. Turner, B. F. Johnston, D. W. H. Rankin, M. Ahmadian, J. N. Jones, A. H. Cowley, *Dalton Trans.* 2004, 2469.

12. A. W. Ross, M. Fink, R. Hilderbrandt, *International Tables for Crystallography*; A. J. C. Wilson, Ed.; Kluwer Academic Publishers: Dordrecht, The Netherlands, 1992; **Vol. C**, 245.
13. V. A. Sipachev, *J. Mol. Struct.*, 1985, **121**, 143.
14. C. Eon, C. Pommier, G. Guiochon, *J. Phys. Chem.*,1971, **75**, 2632.
15. A. J. Blake, P. T. Brain, H. McNab, J. Miller, C. A. Morrison, S. Parsons, D. W. H. Rankin, H. E. Robertson, B. A. Smart, *J. Phys. Chem.*, 1996, **100**, 12280; P. T. Brain, C. A. Morrison, S. Parsons, D. W. H. Rankin, *J. Chem. Soc., Dalton Trans.*, 1996, 4589; N. W. Mitzel, D. W. H. Rankin, *J. Chem. Soc., Dalton Trans.*, 2003, 3650.
16. M. S. Mubarak, D. Peters, *J. Org. Chem.*, 1996, **61**, 8074.

Chapter 6

Molecular structures of 1-ethynyl- and 1-trimethylsilylethynyl-*para*-carboboranes, by combined analysis of gas-phase electron diffraction data and by *ab initio* calculations.

6.1 **Introduction**

"Carborane" is the contraction of the term "carboborane", used in IUPAC to describe all borane clusters containing at least one carbon atom in either the *closo*- or *nido*- polyhedra form, closed or open cage. Members of this electron-deficient family have too few electrons to coordinate the skeletal atoms fully and more orbitals to fill than electrons available. They compensate for this deficiency by having multi-centre bonds in which three or more atoms are linked by a single electron pair.[1-3] With 20 faces and 12 vertices, the substituted dodeca carboranes are in effect three-dimensional analogues of benzene and have thus been labelled "superaromatic". [4] These compounds are robust and substitution is possible at both the boron and carbon sites without breaking the cage.

Although practical direct applications of the compounds studied in this chapter have not yet been elucidated, it is important to note that there are a number of important utilizations of the 1,12-$C_2B_{10}H_{12}$ cages and their derivatives described. These boron clusters have a preponderant role in medicine, essentially due their stability and solubility. Boron neutron capture therapy uses their low toxicity to enter tumour cells in order to destroy them. Because of the need to access high boron content, *para*-carboranes are the best candidates for such methodology. Other methods use the carborane cage as means of transport, because it has essentially the same volume as a benzene ring spinning on one of its 2-fold axes. Several icosahedral carboranes have recently attracted the attention of the pharmaceutical industry. Some derivatives, more potent than *cis*-platin against tumours, are in early clinical development stages.

Recently, some carboranes substituted in the 1,12-position have been used in non-linear optics,[5] where an electromagnetic field is fed in and a frequency or pulse is given back. For a push-pull system, carborane substituted cages are essentially first in their class. Their use is essentially in data storage and optical switching for which a fast time response is required. They also fulfil all requirements to become good liquid crystal candidates. These cages can also be polymerized and used as conducting polymers. The market prospect of these carborane derivatives is

immeasurable. They are already being utilized in the high temperature area to protect nuclear fusion reactor inner walls.[1]

The first synthesis of carboranes was performed in the early fifties, although they were only first characterized in the early sixties. The number of publications through the years has increased and shows a considerable interest nowadays. Despite that it is still not an easily accessible domain, as the cost of the starting material is still considerably higher than that of alternative organic sub-structure compounds. After a relatively slow start several decades ago, thousands of carboranes now exist and because of their many applications, this number will still grow significantly over the coming years.

Mono-substituted 1,12-carboranes were studied by Mark Fox in Durham. He wanted to fully understand the effect of *para* substitution on the boron ring constituent of the cage. The disubstituted *para*-$C_2B_{10}H_{12}$ ethynyl has been recently characterised[6] and there is a need to clarify and understand the effect of the *para* substitutent on the boron cage. Therefore it was emphasized that there was a need to analyze simple carboranes systematically. The structural analyses of *para- ortho-* and *meta-*$C_2B_{10}H_{12}$ were previously carried out by gas electron diffraction[7](GED) but no mono-substituted *para*-carborane was ever observed by GED. Although the X-ray structure of some disubstituted *para* species had been published, none existed for 1,12-$C_2B_{10}H_{11}$-C≡CH and 1,12-$C_2B_{10}H_{11}$-C≡C-$SiMe_3$ at the time this work was carried out. This work will therefore highlight any potential trend for *para*-carborane substitution, using gas-phase electron diffraction and *ab initio* calculations. The behaviour of the simplified molecules will undoubtedly help our comprehension of the effects of more extensive substitution on the cage.

6.2 Experimental

6.2.1 Synthesis

The compounds 1,12-$C_2B_{10}H_{11}$-C≡CH and 1,12-$C_2B_{10}H_{11}$-C≡C-$SiMe_3$ were prepared by literature methods.[8] The samples, provided by Mark Fox, were used for GED without further purification.

6.2.2 Theoretical methods

The *ab initio* calculations were performed using the Gaussian 98 program[9] to obtain initial predictions of geometric and vibrational parameters.

Geometry optimizations for 1,12-$C_2B_{10}H_{11}$-C≡CH and 1,12-$C_2B_{10}H_{11}$-C≡C-$SiMe_3$ were carried out using C_{5v} and C_s symmetry, respectively. Three different methods were used; HF and two methods including electron correlation, B3LYP and MP2. For these methods, basis sets ranging from 6-31G(d) to aug-cc-pVDZ[10-14] were used. Diffuse and polarisation functions were also added to the basis sets, important when a C≡C triple bond is present in the compound. Frequency calculations at HF/6-31G(d), B3LYP/6-31G(d) and B3LYP/cc-pVDZ levels of theory allowed the nature of the stationary points to be determined, confirming that the observed C_{5v} and C_s structures are true minima. The structures of 1,12-$C_2B_{10}H_{11}$-C≡CH and 1,12-$C_2B_{10}H_{11}$-C≡C-$SiMe_3$ with their atom numbering schemes are shown in **Figure 6.1** and **Figure 6.2**.

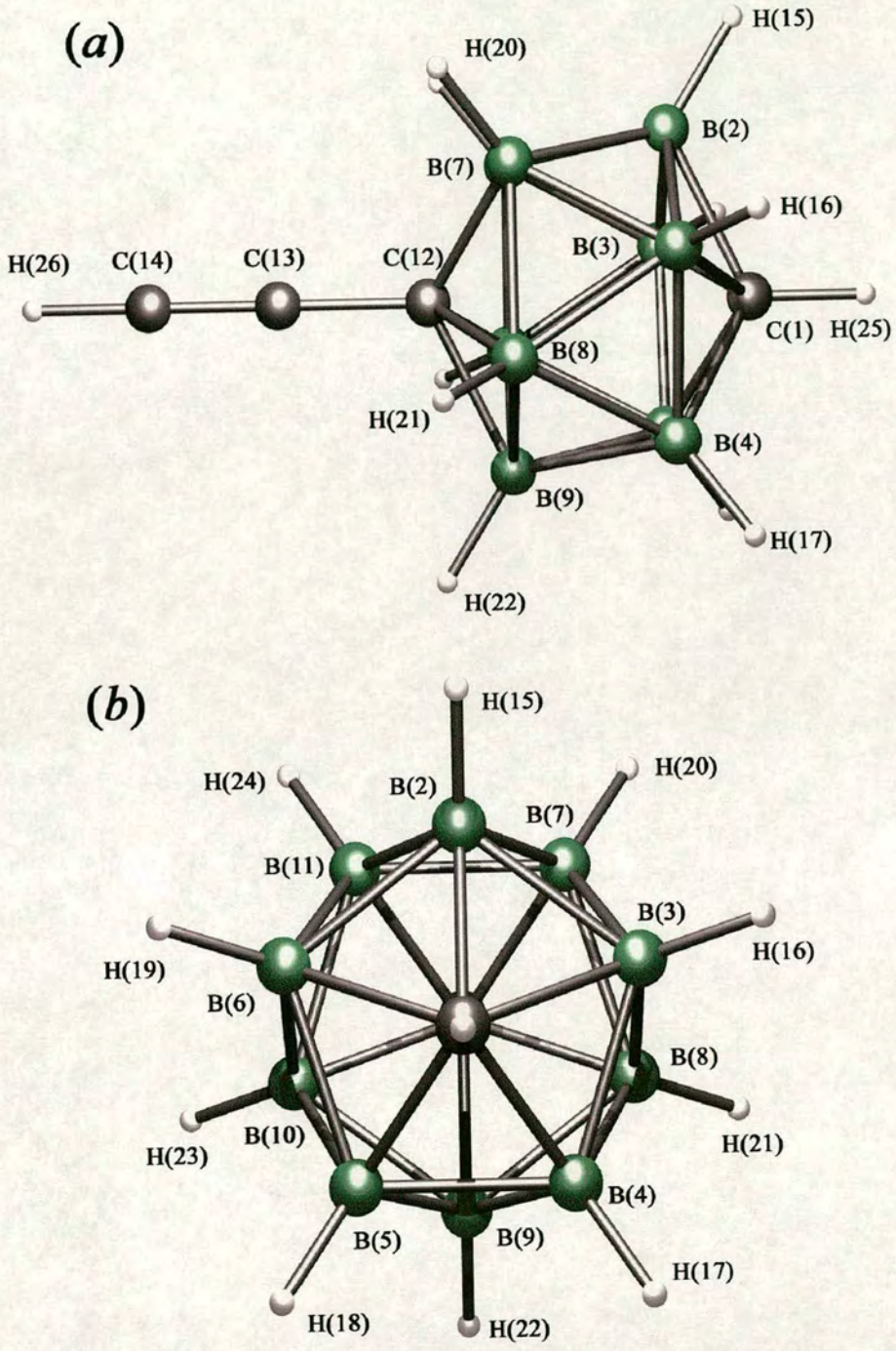

Figure 6.1 : Molecular framework with atom numbering for 1,2-$C_2B_{10}H_{11}$-C≡CH (*a*) side view, (*b*) top view.

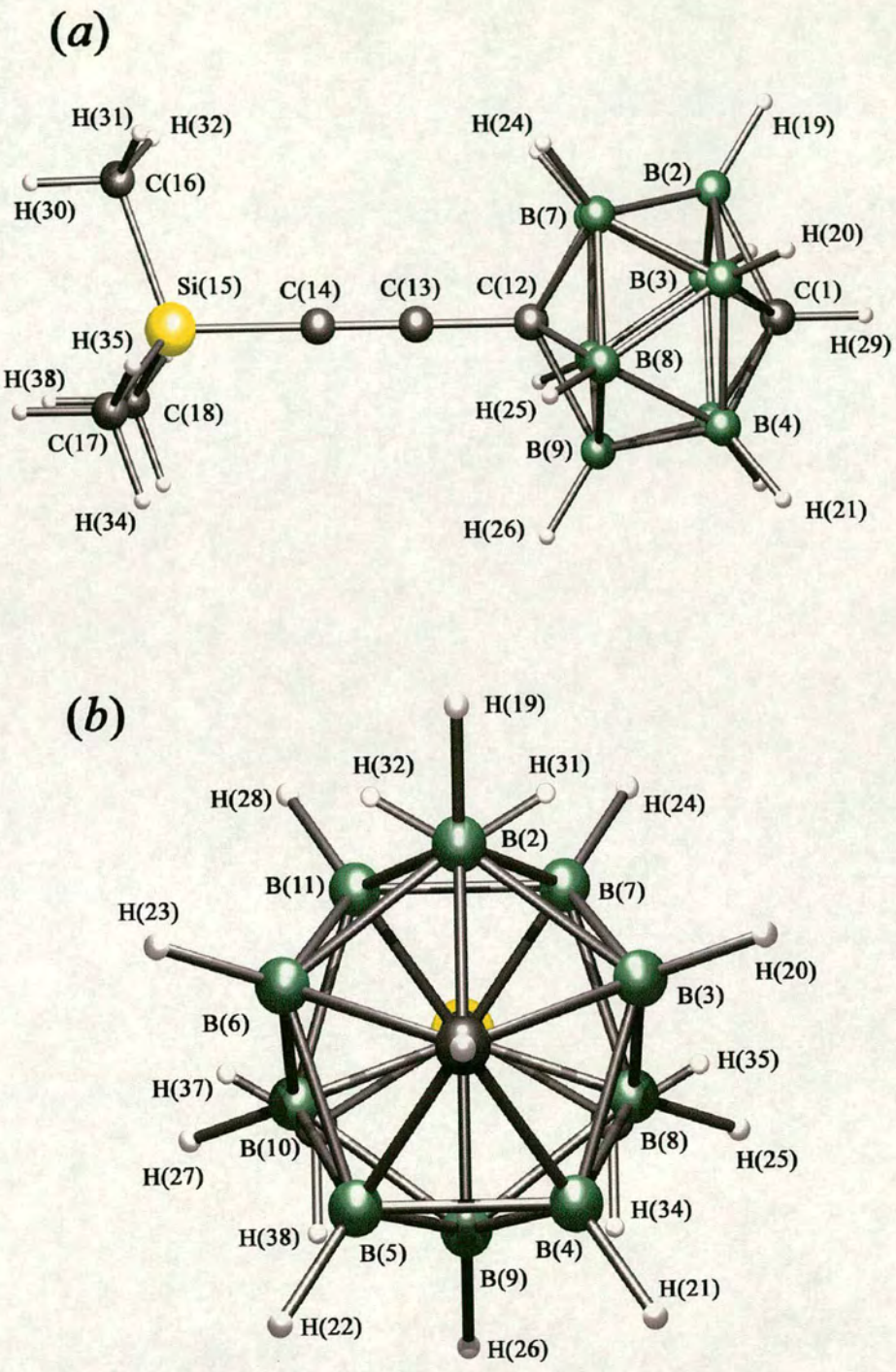

Figure 6.2: Molecular framework with atom numbering for 1,12-$C_2B_{10}H_{11}$-C≡C-$SiMe_3$ (*a*) side view, (*b*) top view

6.2.3 Gas-phase electron diffraction experiment

GED data for both substituted *p*-carboranes were collected at two different camera distances using the Edinburgh apparatus.[11] The data were recorded photographically on Kodak Electron Image films. Three films from each distance were studied for 1,12-$C_2B_{10}H_{11}$-C≡CH, whereas four and three films at long and short distances, respectively, were used for 1,12-$C_2B_{10}H_{11}$-C≡C-$SiMe_3$. The electron-scattering patterns were converted into digital form using an Epson Expression 1600 Pro flatbed scanner with a scanning program as described elsewhere.[15] Electron wavelengths were determined from the scattering pattern of benzene vapour recorded immediately after each carborane run. The weighting points for the off-diagonal weight matrices, correlation parameters, and scale factors for the two camera distances are given in **Table 6.1**. The data reduction and analysis were performed using the program *ed@ed*,[16] employing the scattering factors of Ross *et al.*[17]

Table 6.1: GED data analysis parameters for 1,12-$C_2B_{10}H_{11}$-C≡CH and 1,12-$C_2B_{10}H_{11}$-C≡C-$SiMe_3$.

	1,12-$C_2B_{10}H_{11}$-C≡CH		1,12-$C_2B_{10}H_{11}$-C≡C-$SiMe_3$	
camera distance/mm	261.00	95.26	260.92	96.63
T_{sample}/K	348	365	400	424
T_{nozzle}/K	358	385	413	426
Δs /nm^{-1}	1	2	1	2
s_{min}/nm^{-1}	20	80	20	80
sw_1/nm^{-1}	40	100	40	100
sw_2/nm^{-1}	131	288	129	258
s_{max}/nm^{-1}	152	334	150	300
correlation parameter	0.4991	0.4759	0.4968	0.4106
scale factor, k_a	0.755(4)	0.716(9)	0.784(4)	0.828(11)
electron wavelength /pm	6.02	6.02	6.02	6.02
a	1	2	1	2

Eleven geometric parameters were used to describe structure of *para*-$C_2B_{10}H_{11}$-C≡CH, with a model of C_{5v} symmetry (**Figure 6.1**), for the refinement procedure. Parameters p_1, p_2 and p_3 define the distance between the two C(cage) [C(1)···C(12)], C(cage)-C(ethynyl) [C(12)-C(13)], and C(13)≡C(14) respectively. The average of the bond distances C(1)-B(2) and C(12)-B(7) is defined by parameter p_4. The difference associated with it is defined by p_6 [C(1)-B(2) minus C(12)-B(7)]. The average hydrogen/boron bond distance between B(2)-H(15) and B(7)-H(20) is described by p_5 while p_7 represents the average hydrogen/carbon bond distance between C(1)-H(25) and C(14)-H(26). p_8 defines the average angle between H(25)-C(1)-B and C(13)-C(12)-B whereas the difference between these two angles is represented by p_{11}. While the average angle between C(1)-B-H and C(12)-B-H is defined by p_9, p_{10} defines the differences between these two angles.

The structure of 1,12-$C_2B_{10}H_{11}$-C≡C-$SiMe_3$ was defined by a model of C_s symmetry, using 15 parameters (**Figure 6.2**). In analogy to *para*-$C_2B_{10}H_{11}$-C≡CH parameters p_1, p_2 and p_3 correspond to the C(cage)-C(cage), C(cage)-C(ethynyl) and C(ethynyl)≡C(ethynyl). p_4 defines the average of the bond distance between the C(1)-B(2) and C(12)-B(7), while p_6 is the difference between theses two distances. The average between C-H and B-H distances is described by parameter p_5, while p_7 represents the difference between these two bond distances. The average distance between C(14)-Si(15) and Si-C(16/17/18), and the difference, are defined by p_8 and p_9. The average of angles H(29)-C(1)-B and C(13)-C(12)-B is described by p_{10} whereas their difference is represented by p_{13}. The angle C(1)-B(2)-H(19) and C(12)-B(7)-H(24) are defined by an average and difference (p_{11} and p_{12}). p_{14} represents the angle C(14)-Si(15)-C(16). The methyl group assumes C_{3v} local symmetry and the angles Si(15)-C-H are represented by p_{15}.

The starting parameters for the r_{h1} refinement were taken from the theoretical geometry optimised at MP2/6-311G(d) for para-$C_2B_{10}H_{11}$-C≡CH and MP2/6-31G(d) for 1,12-$C_2B_{10}H_{11}$-C≡C-$Si(Me)_3$. For both compounds a theoretical Cartesian force field was obtained at B3LYP/cc-pVDZ and converted into a force field described by a set of symmetry coordinates using the program SHRINK. [18] It must be noted that

no major differences were seen between the Pople basis set and Dunnings[10-14] type in the Cartesian force field.

6.3 **Results**

6.3.1 Theoretical methods:

For 1,12-$C_2B_{10}H_{11}$-C≡CH, all geometric parameters at all levels of theory and basis set studied are presented in **Table 6.2**. Overall within each method, increasing the basis set has little effect on the bond distances and even less on the angles. The self consistent field level of theory underestimates C-H and B-H distances by 0.8-1.6 pm in comparison to B3LYP and MP2. For C(1)···C(12), effectively the dimension of the carborane cage, B3LYP overestimates it by ~1 pm, while HF underestimates it by the same amount, both with respect to the MP2 method with the same basis set. The ethynyl bond distance, C(13)≡C(14), is underestimated by an average of 4 pm at HF in comparison to MP2. This bond distance with the B3LYP level of theory is calculated to be 3 pm shorter than MP2, both with Pople type basis. This difference is reduced to 2 pm by using Dunning's basis set. Although distances B(2)-B(7) and C(1)-B(2) are invariant for the self consistent field and density functional theory methods, they increase by 0.7 pm when changing basis set from 6-31G(d) to 6-311G(d), at MP2. While the use of the more computationally intensive Dunning's basis sets shows no difference in parameters, aside from the ethynyl distance, differences are observed at MP2 with the Pople basis set at B3LYP. In fact all distances are 1 pm longer with Dunning's basis sets than with the Pople basis sets. Hardly any changes are observed by increasing the description of the valence orbitals. In fact, on average through the methods, only a difference of 0.1 pm for bonded parameters and 0.2° for angles is noted.

Table 6.2: Calculated (r_e) and experimental (r_{h1}) structures of 1,12-$C_2B_{10}H_{11}$-C≡CH

Geometric parameter[a]	Level of theory/ basis set												GED
	HF				MP2				B3LYP				
	6-31G(d)	6-31+G(d)	6-311G(d)	6-311+G(d)	6-31G(d)	6-31+G(d)	6-311G(d)	cc-pVDZ	6-31G(d)	6-311+G(d,p)	cc-pVDZ	Aug-cc-pVDZ	
C(1)-B(2)	170.8	170.7	171.0	171.0	170.2	170.4	171.0	171.9	170.8	170.7	171.0	171.0	170.4(5)
C(1)-H(25)	107.3	107.3	107.2	107.2	108.8	108.9	108.6	109.4	108.4	108.1	108.8	108.7	110.2(12)
B(2)-B(7)	177.1	177.1	177.3	177.2	176.1	176.2	176.8	178.2	176.4	176.4	177.1	176.9	177.8(4)
B(2)-H(15)	117.9	117.9	117.9	117.9	118.7	118.8	118.6	119.5	118.4	117.9	119.1	118.6	118.4(3)
B(7)-C(12)	172.4	172.4	172.6	172.6	171.8	172.0	172.4	173.3	172.7	172.7	172.9	172.8	173.0(5)
B(7)-H(20)	117.7	117.7	117.7	117.7	118.6	118.7	118.6	119.4	118.3	117.7	118.9	118.5	118.4(3)
C(12)-C(13)	145.0	145.0	144.8	144.8	143.9	144.0	143.8	144.6	144.0	143.8	144.3	144.2	143.1(5)
C(13)-C(14)	118.5	118.7	118.2	118.3	122.1	122.3	122.0	123.3	120.6	120.1	121.1	121.0	123.3(5)
C(14)-H(26)	105.7	105.8	105.6	105.6	106.8	106.9	106.6	107.6	106.7	106.3	107.3	106.9	110.2(12)
C(1)...C(12)	306.6	306.5	306.7	306.8	307.3	307.5	307.9	309.3	308.7	308.6	308.7	308.5	307.9(5)
B(2)-C(1)-H(25)	116.9	116.8	116.8	116.8	117.2	117.2	117.1	117.0	117.3	117.2	117.1	117.1	116.7(2)
C(1)-B(2)-H(15)	120.6	120.6	120.5	120.6	120.8	120.8	120.6	120.7	120.7	120.9	120.9	120.9	120.0(7)
C(12)-B(7)-H(20)	119.7	119.6	119.5	119.6	119.5	119.5	119.2	119.3	119.6	119.7	119.7	119.6	118.7(7)
C(13)-C(12)-B(7)	117.5	117.5	117.4	117.5	117.9	117.9	117.8	117.6	118.0	118.0	117.9	117.9	117.8(3)

[a] distances in pm, angles in °

Table 6.3: Calculated (r_e) and experimental (r_{h1}) structures of 1,12-$C_2B_{10}H_{11}$-C≡C-$SiMe_3$

	Level of theory/ Basis set					
Geometric	HF	MP2		B3LYP		GED
parameter[a]	6-31G(d)	6-31G(d)	6-31G(d)	6-311++G(d,p)	cc-pVDZ	
C(1)-B(2)	170.7	170.3	170.8	170.7	171.0	171.1(7)
C(1)-H(29)	107.3	108.8	108.4	108.1	108.8	108.9(4)
B(2)-B(7)	177.1	176.1	176.5	176.4	177.2	176.5(8)
B(2)-H(19)	117.9	118.7	118.4	117.8	119.1	120.1(6)
B(7)-C(12)	172.4	171.9	172.8	172.8	173.0	172.5(5)
B(7)-H(24)	117.7	118.7	118.3	117.7	118.9	120.1(6)
C(12)-C(13)	144.9	143.7	143.9	143.7	144.2	144.2(5)
C(13)-C(14)	119.5	123.4	121.7	121.2	122.1	122.7(5)
C(14)-Si(15)	185.8	184.7	184.8	185.1	186.3	184.0(5)
Si(15)-C(16)	188.6	188.1	188.9	188.4	189.1	187.4(5)
C(16)-H(30)	108.8	109.5	109.7	109.3	110.3	108.9(4)
C(1)···C(12)	306.7	307.6	309.1	309.0	309.1	308.3(9)
B(2)-C(1)-H(29)	116.9	117.2	117.3	117.2	117.1	117.0(3)
C(1)-B(2)-H(19)	120.6	120.8	120.7	120.8	120.8	119.6(9)
C(12)-B(7)-H(24)	119.7	119.5	119.6	119.7	119.7	118.3(9)
B(7)-C(12)-C(13)	117.5	118.0	118.0	118.0	117.9	118.1(3)
C(14)-Si(15)-C(16)	108.2	108.1	108.2	108.0	107.9	109.7(4)
Si(15)-C(16)-H(30)	110.9	110.7	110.7	110.7	110.6	108.6(9)

[a] distances in pm, angles in °

Geometry optimizations for 1,12-$C_2B_{10}H_{11}$-C≡C-$SiMe_3$ were started with C_s symmetry, but after vibrational frequency analysis, independent of methods or basis sets used, was also performed, an imaginary frequency was returned hinting that the C_s structure is a transition state and not a minimum. However, when the calculations are carried out with no symmetry restraint (C_1), the final optimized structure showed close to no deviation from the previous C_s conformation (**Table 6.3**). The frequency calculations confirmed that the C_1 symmetry is a local minimum. Since the lowest vibration calculated at B3LYP/6-31G(d) and B3LYP/cc-pVDZ[10-14] corresponds to the torsional twist of the $SiMe_3$ group (20 cm^{-1}) and the C_1 symmetry calculated has no more deviation than 0.1 pm for bond distances or 0.02° for angles through bonds, the GED model was made with C_s symmetry.

6.3.2 Gas-phase electron diffraction

The model used for the GED refinement of 1,12-$C_2B_{10}H_{11}$-C≡CH was based upon the geometry obtained from the optimised *ab initio* calculations. The least-squares refinement of the structure resulted in an R_G factor of 0.053 (R_D = 0.029), with optimized parameters listed in **Table 6.4**. A summary of final bond distances and amplitudes of vibration is recorded in **Table 6.6**. All 11 geometrical parameters and also 11 groups of amplitudes of vibration were refined. Flexible restraints were employed during the refinement using the SARACEN[19] method. Altogether, six geometric and three amplitude restraints were employed. These are listed in **Table 6.5**. For a full list of the final bond distances and amplitudes of vibration, see appendix G on the CD. The least-squares correlation matrix for the structural refinement is shown in **Table 6.7**. The success of the final refinement can be assessed on the basis of the molecular scattering curves, **Figure 6.4**, and radial distribution curve **Figure 6.7**.

Table 6.4: Geometrical parameters (r_{h1}) for 1,12-$C_2B_{10}H_{11}$-C≡CH.[a,b]

	Parameter	GED	MP2/6-311G(d)
p_1	rC(1)...C(12)	307.8(5)	307.9
p_2	rC(12)C(13)	143.1(5)	143.8
p_3	rC(13)C(14)	123.3(5)	122.0
p_4	av$r$C(1)BrC(12)B	171.6(3)	171.7
p_5	av$r$BH	118.4(3)	118.6
p_6	dif$r$C(12)BrC(1)B	2.6(9)	1.5
p_7	av$r$CH	110.2(12)	107.6
p_8	av∠HC(1)B∠C(13)C(12)B	117.2(1)	117.4
p_9	av∠C(1)BH∠C(12)BH	119.3(7)	119.9
p_{10}	dif∠C(1)BH∠C(12)BH	1.3(1)	1.4
p_{11}	dif∠HC(1)B∠C(2)C(12)B	1.7(4)	0.6

[a] distances in pm, angles in °

[b] see text for parameter definitions

Table 6.5: Flexible restraints used in GED refinement for 1,12-$C_2B_{10}H_{11}$-C≡CH.

	Parameter	Value /pm or °	Uncertainty /pm or °
p_6	dif$r$C(12)BrC(1)B	1.4	0.1
p_7	av$r$CH	108.6	2.0
p_9	av∠C(1)BH∠C(12)BH	120.0	0.9
p_{10}	dif∠C(1)BH∠C(12)BH	1.3	0.1
p_{11}	dif∠HC(1)B∠C(2)C(12)B	0.6	0.3
d_1[a]	B(2)-B(3)	176.1	1.0
u_4	C(12)-C(13)	4.6	0.7
u_{45}	C(12)...C(14)	5.1	0.7
u_{13}	C(1)...C(12)	6.4	0.9

[a] dependent parameter

Table 6.6: Bond distances (r_a/pm) and amplitudes of vibration (u/pm) obtained in the GED refinement of 1,12-$C_2B_{10}H_{11}$-C≡CH.

u	Atom pair	r_a	Amplitude	
u_1	C(14)-H(26)	109.9(12)	7.26	(fixed)
u_2	C(1)-H(25)	110.0(12)	7.5	(fixed)
u_3	C(13)-C(14)	123.3(5)	3.7(3)	
u_4	C(12)-C(13)	143.0(5)	4.0(5)	
u_5	C(1)-B(2)	170.4(5)	7.1	Tied to u_9
u_6	B(2)-B(6)	178.9(6)	7.0	Tied to u_9
u_7	B(7)-C(12)	173.0(5)	7.3	Tied to u_9
u_8	B(7)-B(11)	179.8(6)	7.1	Tied to u_9
u_9	B(7)-B(2)	177.4(4)	6.9(1)	
u_{10}	B(7)-H(20)	118.1(3)	8.7	Tied to u_3
u_{11}	B(2)-H(15)	118.2(3)	8.7	Tied to u_3
u_{12}	C(1)...B(7)	273.9(6)	7.2(3)	
u_{13}	C(1)...C(12)	308.3(5)	6.5(6)	
u_{14}	C(1)...H(16)	250.3(9)	11.4	Tied to u_{37}
u_{15}	C(1)...H(21)	384.8(10)	12.7	Tied to u_{40}
u_{19}	B(2)...C(12)	276.9(6)	7.3	Tied to u_{12}
u_{20}	B(2)...B(10)	288.9(1)	7.5(2)	
u_{21}	B(2)...B(9)	340.0(1)	7.8(3)	
u_{22}	B(2)...B(4)	289.3(10)	7.9	Tied to u_{20}
u_{23}	B(2)...H(25)	240.4(10)	11.0	Tied to u_{37}
u_{24}	B(2)...H(16)	257.6(6)	11.8	Tied to u_{37}
u_{25}	B(2)...H(17)	388.8(10)	13.7	Tied to u_{40}
u_{26}	B(2)...H(21)	394.6(4)	13.3	Tied to u_{40}
u_{28}	B(2)...H(24)	265.8(10)	11.5	Tied to u_{37}
u_{29}	B(2)...C(13)	403.6(4)	9.1	Tied to u_{40}
u_{30}	B(2)...C(14)	518.3(4)	10.9(4)	
u_{32}	B(7)...B(10)	290.8(9)	8.076	Tied to u_{20}
u_{33}	B(7)...H(25)	369.3(12)	14.0	Tied to u_{40}
u_{34}	B(7)...H(16)	265.1(9)	11.5	Tied to u_{37}
u_{35}	B(7)...H(17)	394.4(4)	13.3	Tied to u_{40}
u_{37}	B(7)...H(21)	258.3(5)	11.8(6)	
u_{38}	B(7)...H(22)	390.1(9)	13.9	Tied to u_{40}
u_{39}	B(7)...C(13)	270.9(6)	9.4	Tied to u_{12}
u_{40}	B(7)...C(14)	377.6(6)	13.9(4)	
u_{43}	C(12)...H(16)	387.3(9)	12.8	Tied to u_{40}
u_{44}	C(12)...H(21)	251.1(8)	11.5	Tied to u_{37}
u_{45}	C(12)...C(13)	265.3(6)	5.4(6)	
u_{46}	C(12)...H(26)	373.2(13)	10.2	Tied to u_{40}
u_{63}	H(21)...C(14)	374.7(15)	26.4	Tied to u_{40}

Table 6.7: Least-squares correlation matrix (x100) for GED structure refinement of 1,2-$C_2B_{10}H_{11}$-C≡CH.[a]

	p_4	p_8	p_{11}	u_9	u_{12}	u_{20}	u_{37}	u_{40}	k_2
p_1	69	88		52					
p_2			-62						
p_3								52	
p_4		93		65					
p_8				64					
p_9							51		
p_{11}					-57				
u_9									51
u_{12}						69			

[a] Only elements with the absolute values > 50% are shown; k_2 is a scale factor

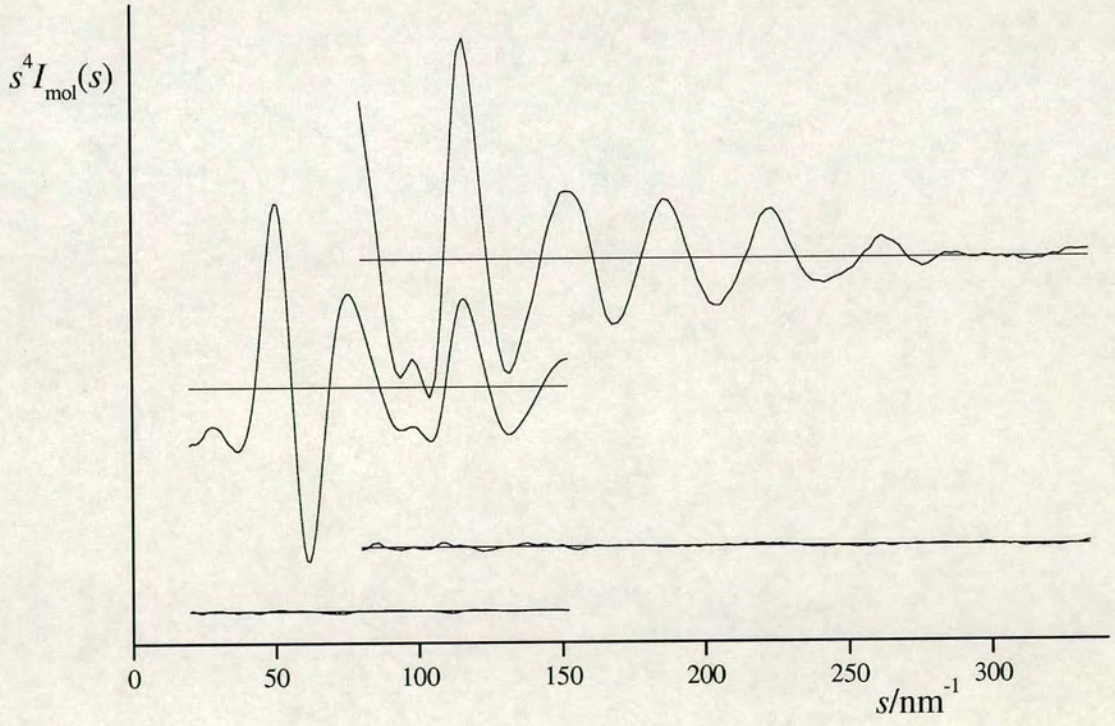

Figure 6.3: Experimental and final weighted difference (experimental-theoretical) molecular scattering intensities for 1,12-$C_2B_{10}H_{11}$-C≡CH.

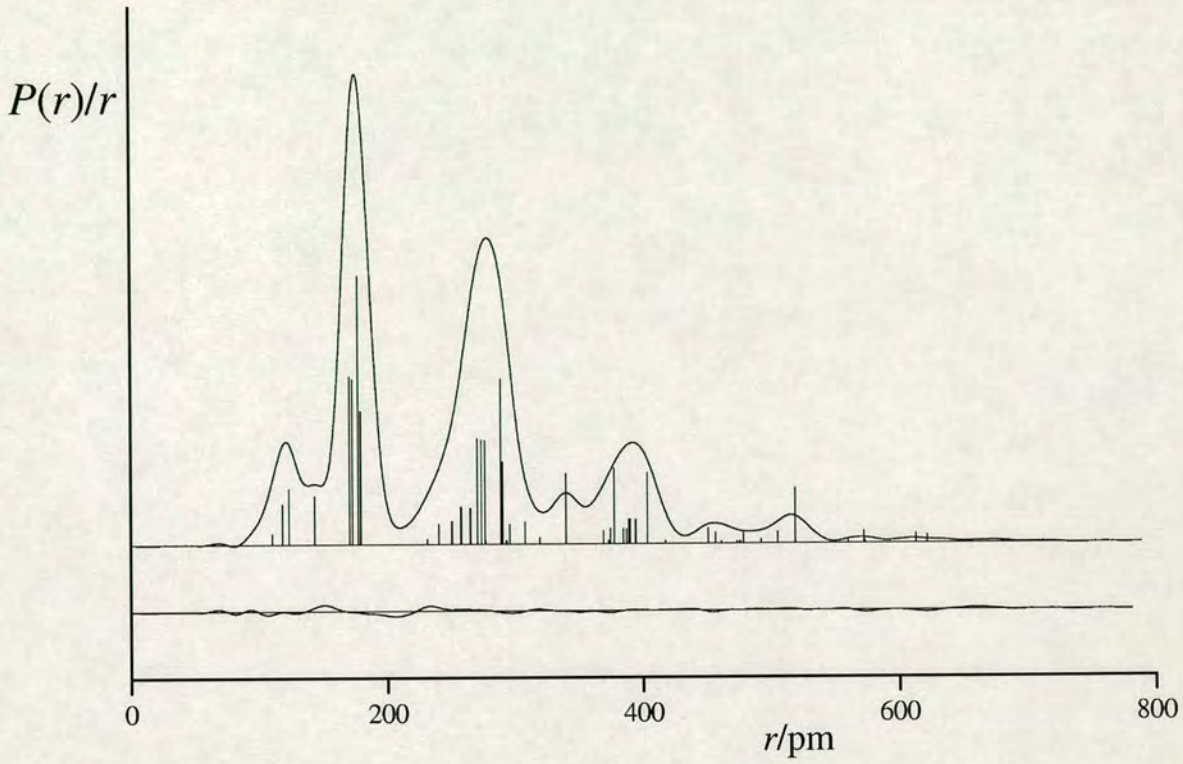

Figure 6.4: Experimental and difference (experimental – theoretical) radial distribution curves, $P(r)/r$, for 1,12-$C_2B_{10}H_{11}$-C≡CH. Before Fourier inversion, the data were multiplied by $s.\exp(-0.00002s^2)/(Z_B\text{-}f_B)(Z_C\text{-}f_C)$

The model used for the GED refinement of 1,12-$C_2B_{10}H_{11}$-C≡C-$SiMe_3$ was based upon the geometry obtained from the optimised *ab initio* calculations. The least-squares refinement of the structure resulted in an R_G factor of 0.048 (R_D = 0.026), with optimized parameters listed in **Table 6.8**. A summary of final bond distances and amplitudes of vibration are recorded in **Table 6.10**. All 15 geometrical parameters and 20 groups of amplitudes of vibration were refined. Flexible restraints were employed during the refinement using the SARACEN[19] method. Altogether, seven geometric and five amplitudes restraints were employed. These are listed in **Table 6.9**. For a full list of the final bond distances and amplitudes of vibration, see appendix G on the CD. The least-squares correlation matrix for the structural refinement is shown in **Table 6.11**. The success of the final refinement can be assessed on the basis of the molecular scattering curves, **Figure 6.5**, and radial distribution curve **Figure 6.6**.

Table 6.8: Geometrical parameters (r_{h1}) for 1,12-$C_2B_{10}H_{11}$-C≡C-$SiMe_3$.[a,b]

	Parameter	GED	MP2/6-31G(d)
p_1	r C(1)...C(12)	308.3(9)	307.6
p_2	r C(12)C(13)	144.2(5)	143.7
p_3	r C(13)C(14)	122.7(5)	123.4
p_4	av$r$ C(1)Br C(12)B	171.8(6)	171.1
p_5	av(av$r$ BHav$r$ CH)	114.5(3)	114.0
p_6	dif$r$ C(12)Br C(1)B	1.4(8)	1.6
p_7	dif(av$r$ BHav$r$ CH)	11.3(8)	9.3
p_8	av$r$ C(14)Si(15)r C(16)Si(15)	185.7(3)	186.4
p_9	dif$r$ C(16)Si(15)r C(14)Si(15)	3.5(8)	3.4
p_{10}	av∠HC(1)B∠C(13)C(12)B	117.6(2)	117.6
p_{11}	av∠C(1)BH∠C(12)BH	119.0(9)	120.1
p_{12}	dif∠C(1)BH∠C(12)BH	1.3(2)	1.3
p_{13}	dif∠HC(1)B∠C(13)C(12)B	1.1(4)	0.7
p_{14}	∠C(14)Si(15)C(16)	109.7(4)	108.1
p_{15}	∠SiCH	108.6(9)	110.7

[a] distances in pm, angles in °

[b] see text for parameter definitions

Table 6.9: Flexible restraints used in GED refinement for 1,12-$C_2B_{10}H_{11}$-C≡C-$SiMe_3$.

	Parameter	Value /pm or °	Uncertainty /pm or °
p_6	dif$r$ C(12)Br C(1)B	1.6	0.8
p_7	dif(av$r$ BHav$r$ CH)	9.3	1.0
p_9	dif$r$ C(16)Si(15)r C(14)Si(15)	3.4	1.0
p_{11}	av∠C(1)BH∠C(12)BH	120.1	1.0
p_{12}	dif∠C(1)BH∠C(12)BH	1.3	0.2
p_{13}	dif∠HC(1)B∠C(13)C(12)B	0.7	0.5
p_{14}	∠C(14)Si(15)C(16)	108.1	0.5
u_1	C(1)-H(29)	7.5	0.5
u_4	C(12)-C(13)	4.7	0.5
u_{10}	C(14)-Si(15)	5.3	0.5
u_{17}	B(2)...H(20)	12.7	1.2
u_{130}	B(2)...Si(15)	16.8	3.0

Table 6.10: Bond distances (r_a/pm) and amplitudes of vibration (u/pm) obtained in the GED refinement of 1,12-$C_2B_{10}H_{11}$-C≡C-Si(Me)$_3$.

u	Atom pair	r_a	Amplitude	
u_1	C(1)-H(29)	108.6(4)	8.2(4)	
u_2	B(2)-H(19)	119.9(6)	9.0	Tied to u_1
u_3	C(13)-C(14)	122.6(5)	3.9	Tied to u_1
u_4	C(12)-C(13)	144.2(5)	4.1(4)	
u_5	C(1)-B(2)	170.9(7)	8.2(5)	
u_6	B(7)-C(12)	171.9(6)	8.6	Tied to u_5
u_7	B(2)-B(7)	176.4(8)	7.2	Tied to u_9
u_8	B(2)-B(3)	179.3(7)	7.2	Tied to u_9
u_9	B(7)-B(8)	179.3(6)	7.4(3)	
u_{10}	C(14)-Si(15)	184.0(5)	5.4(5)	
u_{11}	Si(15)-C(16)	187.4(5)	6.6(4)	
u_{14}	Si(15)...H(30)	244.5(12)	10.0(7)	
u_{15}	C(1)...H(19)	252.1(12)	11.2	Tied to u_{17}
u_{16}	C(12)...H(24)	251.5(12)	11.4	Tied to u_{17}
u_{17}	B(2)...H(20)	259.3(8)	11.8(9)	
u_{18}	B(7)...H(25)	259.3(7)	11.8	Tied to u_{17}
u_{19}	B(7)...H(19)	266.1(12)	11.2	Tied to u_{17}
u_{20}	C(12)...C(14)	265.6(6)	4.8	Tied to u_{17}
u_{21}	B(2)...H(24)	266.0(14)	11.3	Tied to u_{17}
u_{22}	B(7)...C(13)	271.5(9)	10.4	Tied to u_{23}
u_{23}	C(1)...B(7)	273.2(7)	7.9(4)	
u_{26}	B(2)...B(8)	288.3(3)	7.9(4)	
u_{27}	B(2)...B(4)	290.0(11)	8.2	Tied to u_{26}
u_{28}	B(7)...B(9)	289.6(9)	8.5	Tied to u_{26}
u_{31}	C(13)...H(24)	297.2(18)	18.3	Tied to u_{32}
u_{32}	C(14)...C(16)	302.3(9)	12.5(8)	
u_{33}	C(13)...Si(15)	304.3(6)	6.4	Tied to u_{32}
u_{34}	C(1)...C(12)	307.6(9)	7.0	Tied to u_{32}
u_{35}	C(16)...C(17)	305.6(11)	13.0	Tied to u_{32}
u_{42}	B(2)...B(9)	339.2(3)	8.2(4)	
u_{45}	B(7)...C(14)	375.3(9)	15.9(15)	
u_{47}	C(1)...H(24)	385.8(11)	11.9	Tied to u_{50}
u_{48}	C(12)...H(19)	388.3(10)	12.0	Tied to u_{50}

u_{49}	B(2)...H(21)	391.0(13)	13.0	Tied to u_{50}
u_{50}	B(7)...H(26)	390.5(11)	13.1(4)	
u_{51}	B(7)...H(21)	395.6(6)	12.6	Tied to u_{50}
u_{52}	B(2)...H(25)	395.5(7)	12.6	Tied to u_{50}
u_{53}	C(14)...H(30)	391.4(11)	14.3	Tied to u_{50}
u_{54}	C(13)...C(16)	407.1(11)	18.6(23)	
u_{55}	B(2)...C(13)	403.7(6)	9.9(6)	
u_{56}	C(16)...H(34)	394.8(13)	14.5	Tied to u_{50}
u_{57}	C(13)...H(31)	409.5(19)	37.2	Tied to u_{54}
u_{61}	C(12)...Si(15)	446.4(7)	9.1(5)	
u_{62}	C(1)...C(13)	451.2(9)	9.0	Tied to u_{61}
u_{63}	B(2)...H(26)	457.2(6)	13.5	Tied to u_{61}
u_{64}	B(7)...H(22)	457.3(6)	13.5	Tied to u_{61}
u_{72}	C(13)...H(19)	506.3(12)	14.4	Tied to u_{76}
u_{76}	B(2)...C(14)	516.5(5)	12.5(6)	
u_{77}	Si(15)...H(24)	519.1(20)	33.6	Tied to u_{76}
u_{80}	C(12)...C(16)	536.8(12)	26.0	Tied to u_{83}
u_{83}	B(7)...Si(15)	544.8(8)	18.8(6)	
u_{130}	B(2)...Si(15)	690.3(6)	20.4(7)	

Table 6.11: Least-squares correlation matrix (x100) for GED structure refinement of 1,12-$C_2B_{10}H_{11}$-C≡C-$SiMe_3$.[a]

	p_4	p_8	p_{10}	u_5	u_9	u_{12}	u_{18}	u_{26}	u_{32}	u_{49}	u_{84}
p_1	79	-68	89	60	56						
p_4		-64	95	79						54	
p_8			-62	-53	-71						
p_9						-52					
p_{10}				79						51	
p_{15}							63				
u_5										56	
u_9						67		58	65		
u_{23}								81	61		
u_{26}									82		
u_{76}											59

[a] Only elements with the absolute values > 50% are shown

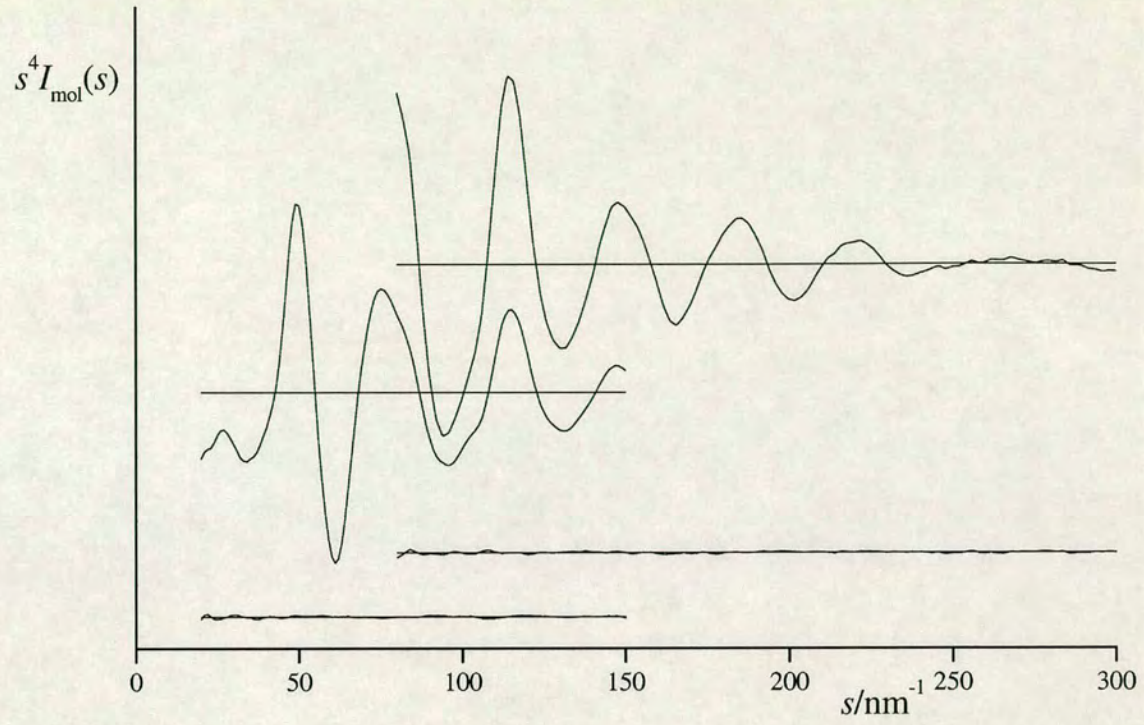

Figure 6.5: Experimental and final weighted difference (experimental-theoretical) molecular scattering intensities for 1,12-$C_2B_{10}H_{11}$-C≡C-$SiMe_3$.

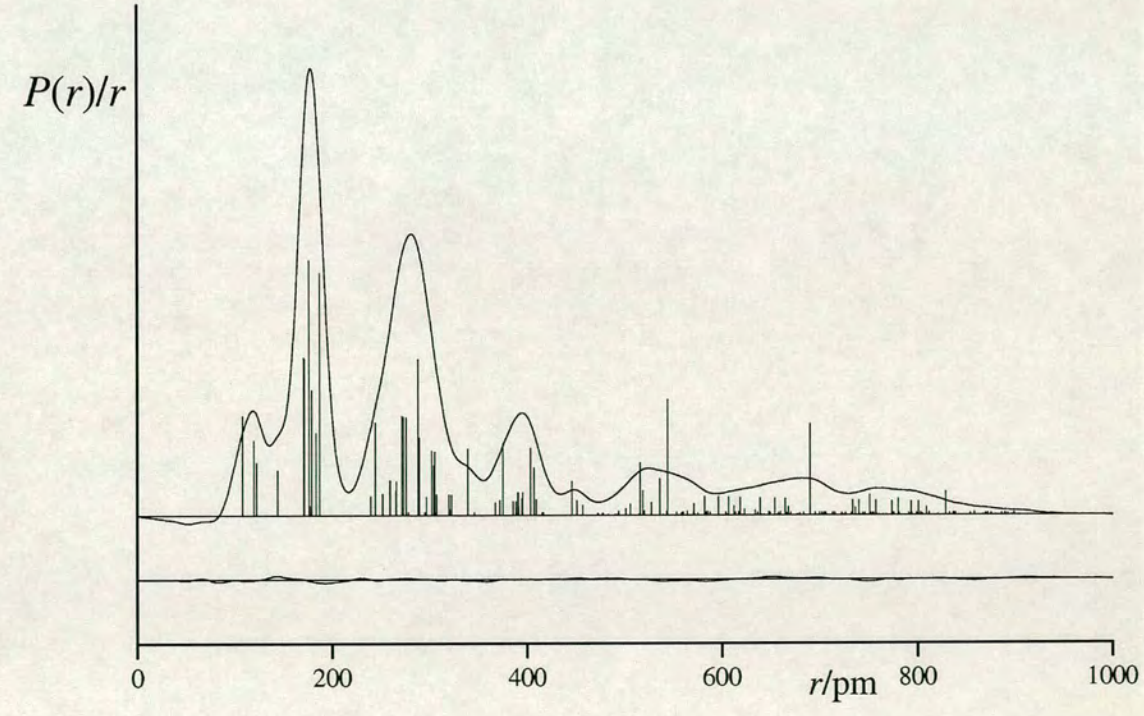

Figure 6.6: Experimental and difference (experimental – theoretical) radial distribution curves, $P(r)/r$, for 1,12-$C_2B_{10}H_{11}$-C≡C-$SiMe_3$. Before Fourier inversion, the data were multiplied by $s.\exp(-0.00002s^2)/(Z_B\text{-}f_B)/(Z_C\text{-}f_C)$

6.4 **Discussion**

Overall the *ab initio* methods used and the basis sets chosen perform reasonably well in predicting the gas-phase structures of the carborane cages. In general the Pople basis performed extremely well. Theoretical calculations are in good agreement with the experimental data from GED, using electron correlation (MP2) and the 6-31G(d) basis set. The biggest differences in distances are not more than 1 pm in the description of the cage, corresponding to one or two estimated standard deviations (e.s.d.). The differences in angles are less than 0.5°. This method and definition of orbital geometry is the best compromise between information retrieval and computing time cost. Therefore, for carborane cages, investigation via *ab initio* is a good methodology to understand the correlation between the systematic variation in the cage structure and its substitutions. This would allow us to generate *in silico* a family of compounds that would be rather challenging synthetically and thus identify those that might display the most important features. Of course, the *ab initio* calculations will never replace experimental results.

In both refinements, the C-B-H angles were defined as an average and a difference, due the fact that there is *ab initio,* independent of method or basis set, a difference of 1° between the two halves of the cage. Both differences and averages were restrained with uncertainties of 1° using the Saracen method. Without these restraints the C-B-H would become unrealistically large, as encountered previously in the gas-phase structure of 1,12-dicarba-closo-dodecarborane.[7]

One parameter was used to describe the C-H bonds in 1,12-$C_2B_{10}H_{11}$-C≡C-$SiMe_3$, although from *ab initio* calculations there is a difference of 2 pm between all the methyl C-H and the C-H from the carborane cage. It would be impossible to differentiate between them in GED as independent parameters. They would have a large e.s.d., and would have to be constrained to their calculated values. No information defining the C-H would have been extracted from the experimental data. For 1,12-$C_2B_{10}H_{11}$-C≡CH an average parameter for the B-H bond was used, although

no difference between B(2)-H(15) and B(7)-H(20) was observed *ab initio* (less than 0.1 pm). This parameter is really well characterised and close to the theoretical prediction without any restraint in the gas-phase structure.

In the theoretical calculations, it was noticed that there was no change in the angle, through level of theory and basis set, between the five-fold axis of the borane cages and the C-B bonds, less than 0.1°. A constant difference of 0.7° between the two sides of the cage is observed as well. With an e.s.d. of less than half of a degree it can be concluded that the two parameters describing these angles are well characterized.

A prior refinement of 1,12-$C_2B_{10}H_{11}$-C≡CH revealed the B(2)-B(7) bond distance, between the two penta-borane rings, to be longer than calculated, with a distance of 178.5 pm measured instead of the 176-177 pm predicted by *ab initio* calculations. The second refinement, carried out on 1,12-$C_2B_{10}H_{11}$-C≡C-$SiMe_3$, showed good agreement with theory. Analysing the trends in **Table 6.12** confirmed that this distance is relatively constant and does not depend on the method of measurement or on the substituents on the carborane cage. Therefore a restraint of 1 pm was placed on the dependent parameter defining this particular bond distance. The use of this restraint yielded a more realistic B(2)-B(7) distance of 177.8(4) pm. This agrees well with that in the previously published structure of the unsubstituted carborane[7] (177.2 pm). The overall effect on the geometry of the molecule was not significant, the biggest difference observed being of the order of one half of an e.s.d. for the C(1)-B(2). When a tighter restraint of 0.5 pm was applied, all the other geometry parameters were forced to compensate for the change in B-B and the R_G factor increased by 20% with respect to the refinement carried out with looser restraints.

Both 1,12-$C_2B_{10}H_{11}$-C≡C-$SiMe_3$ and 1,12-$C_2B_{10}H_{11}$-C≡CH display the same characteristics in the carborane cage. Both cages display C_{5v} symmetry. The substitution at the ethynyl carbon atom results in no noticeable changes in the cage geometry. In fact all the changes in the geometry of the cage are only within one order of e.s.d. The C···C distances, which are of the order of 308 pm for both

compounds, emphasize the fact that the dimension of the cage is not affected by a substitution on the ethynyl terminal carbon atom.

For 1,12-dicarboxyl-1,12-dicarbaba-closo-decaborane[20] and all other 1,12-substituted carboranes determined by X-ray crystallography, the tropical, basal B-B (ii_1 and ii_2 **Figure 6.7**) are longer than the meridianal, C-B (i_1 and i_2 **Figure 6.7**) and the longitudinal B-B (iii **Figure 6.7**) by 2 pm on average. The differences between the two tropical B-B distances in the two gas-phase structures are identical or at most have one esd difference. Therefore, in this study, the B-B basal bond lengths are independent of the substitution on their respective carbon ends.

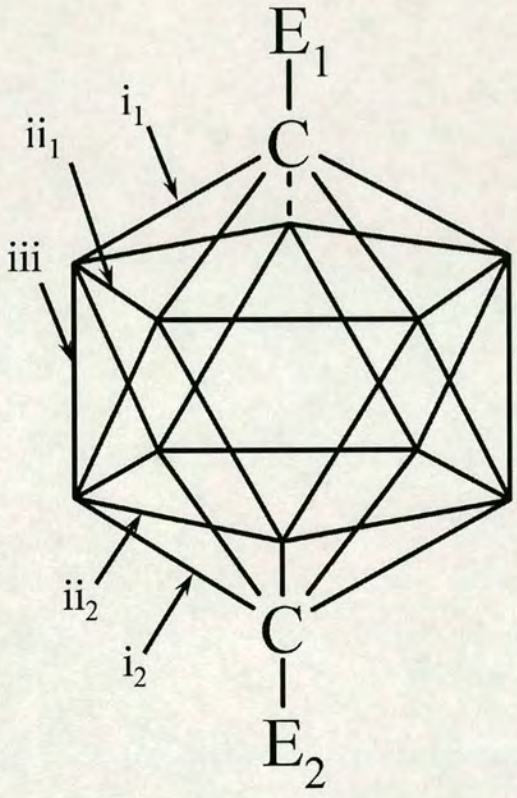

Figure 6.7: Schematic of the carboranes showing the C-B (i_1 and i_2), tropical B-B (ii_1 and ii_2) and the longitudinal B-B distances (iii).

Although a longer ethynyl CC bond distance would be expected because of the electron-donating capability of the silane substituent, the experimental structure shows a difference of 1 pm to the calculation that can hardly be differentiated due to the 0.5 pm e.s.d.. The C(cage)-C(ethynyl) bonds display identical distances with both

substitutions, with hybridization expected to make the bond longer than pure sp-sp hybridization, as mentioned by Mark Fox.[6] They lie between the standard $C(sp^2)$-C(sp) and $C(sp^3)$-C(sp) bond length. The molecular orbital, in **Figure 6.8**, analysis shows that, due to symmetry, the HOMO orbital is doubly degenerate and consists of π-bonding in the C(ethynyl)-C(ethynyl) bond. The C(cage) *p* orbital is out of phase with respect to the orbital sign of C(ethynyl). The LUMO, on the other hand, shows π anti-bonding of C(ethynyl)-C(ethynyl) and π-bonding of the C(ethynyl)-C(cage) bond. This orbital also includes of some π-bonding in the carborane cage. This is true for both species. The addition of the silane group stabilizes the LUMO orbital by 13 kJ mol^{-1} or 0.1 eV.

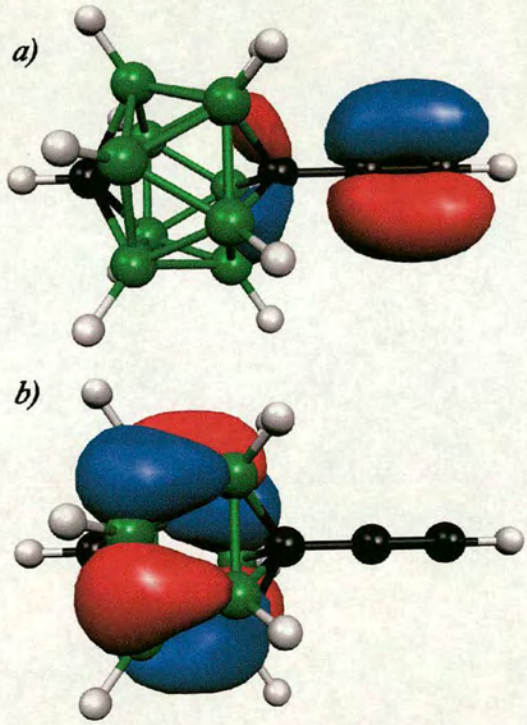

Figure 6.8: (a) HOMO and (b) HOMO-2 orbitals for 1,12-$C_2B_{10}H_{11}$-C≡CH showing the "superaromaticity" of typical carborane cages.

Table 6.12 shows all the relevant structures of the *para*-substituted carboranes and some extra substitutions carried out via *ab initio* calculations at the MP2/6-31G(d) level (see **Figure 6.7**). It emphasizes the point made earlier that the B-B meridional distances (iii) are unaffected by substitution at the poles of the carborane cage. Looking at the *para*-disubstituted ethynyl carborane and the unsubstituted carborane crystal structure, the values of ii_x and iii are unchanged. The major changes, as observed previously,[6] are for bonds i_x, with a difference of 2 pm. Since all other distances are unchanged between the two it was expected that mono substitution would have affected only one side of the cage. Therefore no compensation for the change in electronic environment on the pole should be observed through the molecule. These calculations were the first to confirm this fact. It was confirmed through the GED experimental structure that the cage is split into two polar caps independent of one another and therefore not aware of the other environment. In fact the H and the ethynyl sides are in perfect agreement with their respective disubstituted X-ray structures. The increase in length of bond i from the unsubstituted to the *para*-substituted structures has the direct effect of increasing the cage size for which the C···C is increased by 4-5 pm. Both GED structures have C···C longer by 2.5 pm in comparison to **1** and to the previously reported 1,12-carborane GED structure.[7] This corresponds to half the distance change of the disubstituted carborane between **1** and **5**. The change for the carbonyl substitution is of the order of 1 pm for C-B for **8** and **9**. Once again the calculations agree extremely well with the X-ray structure. The predicted change in the unsubstituted C···C bond distance is expected to be less than for the previously studied structures **8** and **9**, for which changes of the order of 2 pm and 1 pm were observed, respectively.

Since the *ab initio* calculations were in perfect agreement with the experimental results it was decided to extrapolate and to investigate in more general terms the properties of the cage. Because of computing efficiency and cost, mono substitutions were carried out, and only when X-ray data were available were calculation for the disubstituted species performed. The steady behaviour of the C-H pole highlighted

the lack of communication between the two poles. All studies were carried out at the MP2/6-31G(d) level, these being the best compromise between information gained and cost. Two effects were investigated, the electron-withdrawing group capability on the carborane cage and the electron-donating capabilities of the cage itself. Increasing the strength of the electron-withdrawing substituent has the opposite effect to what had been observed so far. Substituting chlorine by fluorine resulted in i_2 shortening by more than 0.5 pm. The electron-withdrawing substituent shrank the cage size from 305.6 pm for **1** to 304 pm for **13**. The rest of the cage dimensions are consistent with the previously reported structures and, iii and ii do not vary. The study was completed by including the effect of a silyl group, as well as an amine substitution at one of the poles of the cage. As would be expected with electron-donating groups, the i_2 and C···C distances have increased in comparison to **1**, leaving i_1, iii and ii_x unchanged. Replacement of the ethynyl hydrogen by fluorine or chlorine has no effect on the cage itself although the C(ethynyl)···C(ethynyl) has understandably shortened due to the presence of the electron withdrawing group.

Table 6.12: *Para*-carborane substitution effect on the shape of the cage.[a]

#	E_1	E_2	i_1	i_2	iii	ii_1	ii_2	C···C	C(cage)-C(E_2)	C(ethynyl)-C(ethynyl)	Reference	method
1	H	H	170.4(5)	170.4(5)	176.2(5)	178.1(7)	178.1(7)	305.6(4)			20	XRD
2	H	H	170.3(3)	170.3(3)	176.5(3)	177.7(3)	177.7(3)	307.1			21	XRD
3	H	H	170.3	170.3	176.2	178.1	178.1	304.7			21	MP2/6-31G(d)
4	H	C≡CH	170.4(5)	173.0(5)	177.8(4)	179.0(5)	179.9(5)	307.9(5)	143.1(5)	123.3(5)	this work	GED
5	H	C≡CH	170.2	171.8	176.1	177.9	178.4	307.3	143.9	122.1	this work	MP2/6-31G(d)
6	C≡CH	C≡CH	172.6(3)	172.6(3)	176.1(2)	179.3(3)	179.3(3)	310.4(2)	144.9(2)	118.0(3)	22	XRD
7	C≡CH	C≡CH	171.8	171.8	175.9	178.4	178.4	309.9	143.8	122.1	this work	MP2/6-31G(d)
8	C≡C-$SiMe_3$	C≡C-$SiMe_3$	172.6(2)	172.6(2)	176.5(2)	1.789(2)	1.789(2)		145.2(2)	119.3(3)	23	XRD
9	C≡C-$SiMe_3$	C≡C-$SiMe_3$	171.9	171.9	175.9	178.3	178.3	310.5	143.7	123.5	this work	MP2/6-31G(d)
10	H	C≡C-$SiMe_3$	170.8(7)	172.5(6)	176.5(8)	179.2(7)	178.9(6)	308.3(9)	144.1(5)	122.7(5)	this work	GED
11	H	C≡C-$SiMe_3$	170.3	171.9	176.1	178.0	178.5	307.6	143.7	123.4	this work	MP2/6-31G(d)
12	CO_2H	CO_2H	171.1(3)	171.1(3)	175.8(3)	178.4(5)	178.4(5)	306.5(2)	151.5(1)		24	XRD
13	H	CO_2H	170.1[b]	171.1[b]	176.1[b]	178.1[b]	178.5[b]	305.7	151.2		this work	MP2/6-31G(d)
14	H	C≡CF	170.2	171.8	176.1	177.9	178.4	307.4	143.9	121.4	this work	MP2/6-31G(d)
15	H	C≡CCl	170.3	171.9	176.1	178.0	178.5	307.4	143.7	122.4	this work	MP2/6-31G(d)
16	H	Cl	170.2	170.8	176.1	178.0	178.4	305.4			this work	MP2/6-31G(d)
17	H	F	170.3	170.2	176.1	178.1	178.4	304.0			this work	MP2/6-31G(d)
18	H	NH_2	170.3[b]	171.5[b]	176.2[b]	177.9[b]	177.6[b]	308.3			this work	MP2/6-31G(d)
19	H	SiH_3	170.3[b]	171.3[b]	176.3[b]	178.1[b]	177.7[b]	307.5			this work	MP2/6-31G(d)

[a] see Figure 7 for description of E_1, E_2, i_1, i_2 , iii, ii_1 and ii_2.

[b] C_s symmetry; average bond distances shown.

The *para*-substituted carborane cages are susceptible to the electron-donating/withdrawing capabilities of their substituent, although smaller effects are observed for electron-withdrawing groups. These effects are only reflected on the substituted side. Only the C(cage) position and the distance between the centre of gravity of the borane ring and the C(cage) are affected by the substituent. There is a constant difference between the B-B meridional distances (iii) and the tropical B-B bond distance (ii_x) of 2 pm, independent of the substituent. The B-B bond distances in each pentaborane ring are constant but the distance between the two ends, ii_1 and ii_2, is calculated to vary by 0.5 pm. However, this difference cannot be observed experimentally as the standard deviation is bigger than that difference. Although it is beyond the scope of this study it would be interesting to see the behaviour of the *ortho* and *meta*-substituted carborane cages, as well, to investigate systematic substitution of the boron cage with electron-withdrawing/donating groups, to see the properties of each atom building up the cage.

The disubstituted *para* calculation carried out virtually reproduced the X-ray structure. This allows us to conclude that the cage is rigid and temperature has little effect on its structure. The differences in structure due to vibration of the cage are not measurable experimentally.

While in electron diffraction the shrinkage effect is taken into account, in X-ray crystallography it is not. Moreover X-ray diffraction locates centre of electron density rather than nuclear positions. These explain the discrepancy in the C(ethynyl)-C(ethynyl) bond distance calculated *ab initio* and observed in the X-ray structure. The difference of 4 pm confirms that there is a need to include vibrational corrections during the X-ray structure refinement as in GED. The other way to reduce this effect would be to grow a crystal and collect the diffraction pattern at a temperature ideally closer to absolute zero. This effect is only observable for this distance due to the fact that it is the only distance involving a large-amplitude vibrational mode.

Graphical analysis of the electronic density has only highlighted what was expected, a higher electronic density on the ethynyl bond (the red region in **Figure 6.9**). A difference in electronic density should be observed in the B-C(cage) between the substituted end and non-substituted end, but unfortunately it is impossible to draw such conclusions from the multiple cut planes presented in appendix G on the CD.

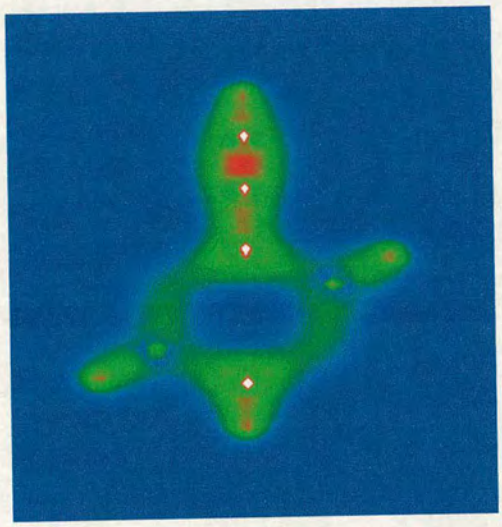

Figure 6.9: A section through the electronic density along the C(1)B(7)B(6) plane. The highest electronic density is shown in red.

The molecular orbital studies follow the expected trends (**Table 6.13**). Although less stable than the unsubstituted cage, all the *para*-carboranes are still considerably more stable than the benzene ring. The ethynyl substitutions destabilise the HOMO by 72 kJ mol^{-1} in comparison to those with a fluorine substituent.

#	E_1	E_2	LUMO	HOMO	HOMO-2
4	H	C≡CH	3.162	-10.601	-11.163
7	H	C≡C-$SiMe_3$	3.026	-10.601	-11.130
9	H	CO_2H	2.874	-11.234	-12.485
10	H	C≡CF	3.183	-10.842	-11.240
11	H	C≡CCl	3.060	-10.358	-11.252
12	H	Cl	3.379	-11.330	-11.986
13	H	F	3.054	-11.350	-12.620
14	H	SiH_3	3.491	-11.077	-12.200

Table 6.13: Orbital energy in eV vs. substituents.

6.5 **Conclusions**

This work contains the gaseous structures of two carboranes with substituted cages, 1,12-$C_2B_{10}H_{11}$-C≡C-$SiMe_3$ and 1,12-$C_2B_{10}H_{11}$-C≡CH. It has shown that *ab initio* calculations perform extremely well with rather small basis sets but there is electron correlation, so that a method such as MP2 should be used. The hybrid density functional theory chosen (B3LYP) also performs well, and has a distinct computing cost advantage in comparison to MP2. The reason there is such a good agreement between the theoretical and experimental methods is that the cage is relatively rigid and only slightly subject to the temperature changes for its amplitudes of vibration. In fact GED is measuring an average vibrating molecule whereas the theory is the representation of the molecule at absolute 0 K.

6.6 **References**

1. R. N. Grimes, *J. Chem. Ed.*, 2004, **81**, 657
2. J. Casanova, *The Borane, Carborane, Carbocation Continuum*, John Wiley & Sons Inc., New York, 1998.
3. R. E. Williams, *Chem. Rev.* 1992, ***92***, 177_207.
4. F. A. Cotton, G. Wilkinson, C. A. Murillo, M. Bochmann, *Advanced Inorganic Chemistry*, John Wiley & Sons Inc., New York, 1999.
5. P. R. Prasad, D. J. Williams, *Introduction to Nonlinear Optical Effects in Molecules and Polymers*; Wiley & Sons: New York, 1991.
6. A. S. Batsanov, M. A. Fox, J. A. K. Howard, H. J. A. MacBride, K. Wade, *J. Organomet. Chem.*, 2000, **610**, 20.
7. R. K. Bohn, M. D. Bohn, *Inorg. Chem.*, 1971, **10**, 351.
8. A. S. Batsanov, A. M. Cameron, M. A. Fox, A. E. Geota, P. J. Low, M. A. J. Paterson, D. W. H. Rankin, H. E. Robertson, J. T. Schirlin, *manuscript in preparation.*
9. Gaussian 98, Revision A.7, M. J. Frisch, G. W. Trucks, H. B. Schlegel, G. E. Scuseria, M. A. Robb, J. R. Cheeseman, V. G. Zakrzewski, J. A. Montgomery, R. E. Stratmann Jr, J. C. Burant, S. Dapprich, J. M. Millam, A. D. Daniels, K. N. Kudin, M. C. Strain, O. Farkas, J. Tomasi, V. Barone, M. Cossi, R. Cammi, B. Mennucci, C. Pomelli, C. Adamo, S. Clifford, J. Ochterski, G. A. Petersson, P. Y. Ayala, Q. Cui, K. Morokuma, D. K. Malick, A. D. Rabuck, K. Raghavachari, J. B. Foresman, J. Cioslowski, J. V. Ortiz, A. G. Baboul, B. B. Stefanov, G. Liu, A. Liashenko, P. Piskorz, I. Komaromi, R. Gomperts, R. L. Martin, D. J. Fox, T. Keith, M. A. Al-Laham, C. Y. Peng, A. Nanayakkara, C. Gonzalez, M. Challacombe, P. M. W. Gill, B. Johnson, W. Chen, M. W. Wong, J. L. Andres, C. Gonzalez, M. Head-Gordon, E. S. Replogle and J. A. Pople, Gaussian, Inc., Pittsburgh PA, 1998.
10. D. E. Woon, T. H. Dunning, *J Chem. Phys.*, 1993, **98**, 1358.
11. C. M. Huntley, G. S. Laurenson, D. W. H. Rankin, *J. Chem. Soc., Dalton Trans.* 1980, 954.
12. T. H. Dunning, *J. Chem. Phys.*, **1989**, 90, 1007.

13. R. A. Kendall, T. H. Dunning, R. J. Harrison, *J Chem. Phys.*, 1994, **100**, 7410.
14. A. Wilson, T. van Mourik, T. H. Dunning, *J. Mol. Struct.*, 1997, **388**, 339.
15. J. R. Lewis, R. J. Mawhorter, S. L. Hinchley, D. W. H. Rankin, *manuscript in preparation*.
16. S. L. Hinchley, H. E. Robertson, K. B. Borisenko, A. R. Turner, B. F. Johnston, D. W. H. Rankin, M. Ahmadian, J. N. Jones, A. H. Cowley *Dalton Trans.* 2004, 2469.
17. A. W. Ross, M. Fink, R. Hilderbrandt, *International Tables for Crystallography*; A. J. C. Wilson, Ed.; Kluwer Academic Publishers: Dordrecht, The Netherlands, 1992; **Vol. C**, 245.
18. V. A. Sipachev, *J. Mol. Struct.*, 1985, **121**, 143.
19. A. J. Blake, P. T. Brain, H. McNab, J. Miller, C. A. Morrison, S. Parsons, D. W. H. Rankin, H. E. Robertson, B. A. Smart, *J. Phys. Chem.*, 1996, **100**, 12280; P. T. Brain, C. A. Morrison, S. Parsons, D. W. H. Rankin, *J. Chem. Soc., Dalton Trans.*, 1996, 4589; N. W. Mitzel, D. W. H. Rankin, *J. Chem. Soc., Dalton Trans.*, 2003, 3650.
20. R. Cetonre, M. R. Ciajolo, A. Tuzi, *Acta Cryst*, 1994, **50**, 905

Chapter 7

Conclusions, future work and last thoughts.

7.1 Reservoir and nozzle

We have demonstrated that by using both the new reservoir and the slit nozzle design the temperature at which the experiments can be run can be reduced. We have shown that time and the sizes of the reservoir are crucial elements for compounds in low vaporisation conditions. Although the measured amplitudes of vibration get slightly larger, the integration of the codes utilized in the diffraction simulations from the slit nozzle will allow for these differences, resulting in unperturbed structures and amplitudes. Candidates for this new hardware improvement in gas-phase electron diffraction are main group and transition metal complexes with phosphorus-containing cyclo-polyene ligands. The indium and gallium compounds synthesised and provided by Prof. J. F. Nixon are shown in **Figure 7. 1**.

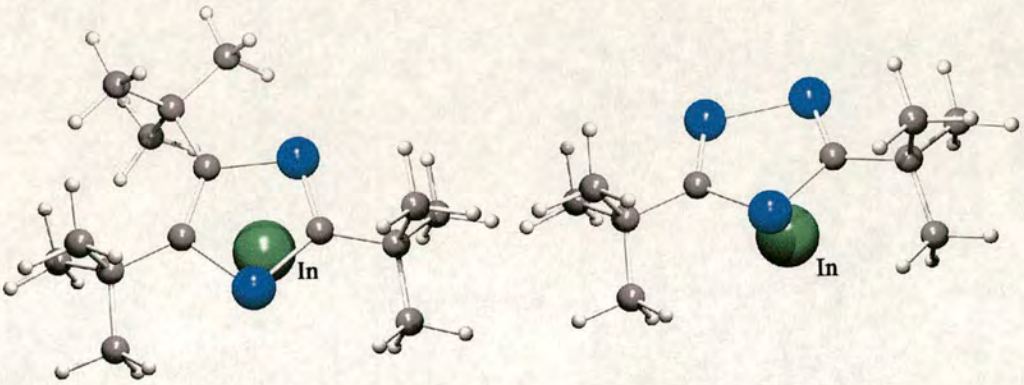

Figure 7. 1: Candidates for new hardware GED design phospha-polyene metal complexes.

Benzothiazole, with a boiling point of 231°C, would be a good candidate to test the limit of the new apparatus design. As currently neither an X-ray crystal structure nor an electron diffraction structure have been published for 2-hydroxyphenyl-benzothiazole or for benzoxazole, this technology would give a reference dataset for further investigations. The aromaticity upon substitution of the compound can also be monitored. Although the exact positioning of the hydrogen atom of the hydroxyl group would be a challenge with common methods, the use of DYNAMITE[1] should solve this problem. An accurate O-H bond length can therefore be determined for the hydroxyl, unlike the previously published X-ray structure.[2] The program Shrink[3]

would be required as well since a low frequency is observed (25 cm^{-1}), and so large-amplitude corrections are expected. Primary *ab initio* investigations of the core structure reveal that the electronic density changes considerably due to 2-substitution.

When looking for other readily available candidate compounds, we noticed that there are still a number of low molecular weight natural products for which no GED structures exist. Some do not even have an X-ray crystal structure, despite their wide interest implied by the thousands of references to them. Some of the potential candidates might be challenging because of the number of torsional degrees of freedom, but it should still be feasible to get structural information. Consequently they will all require the latest software improvements to achieve reliable structures. Potential compounds for structural studies are shown in **Figure 7. 2**.

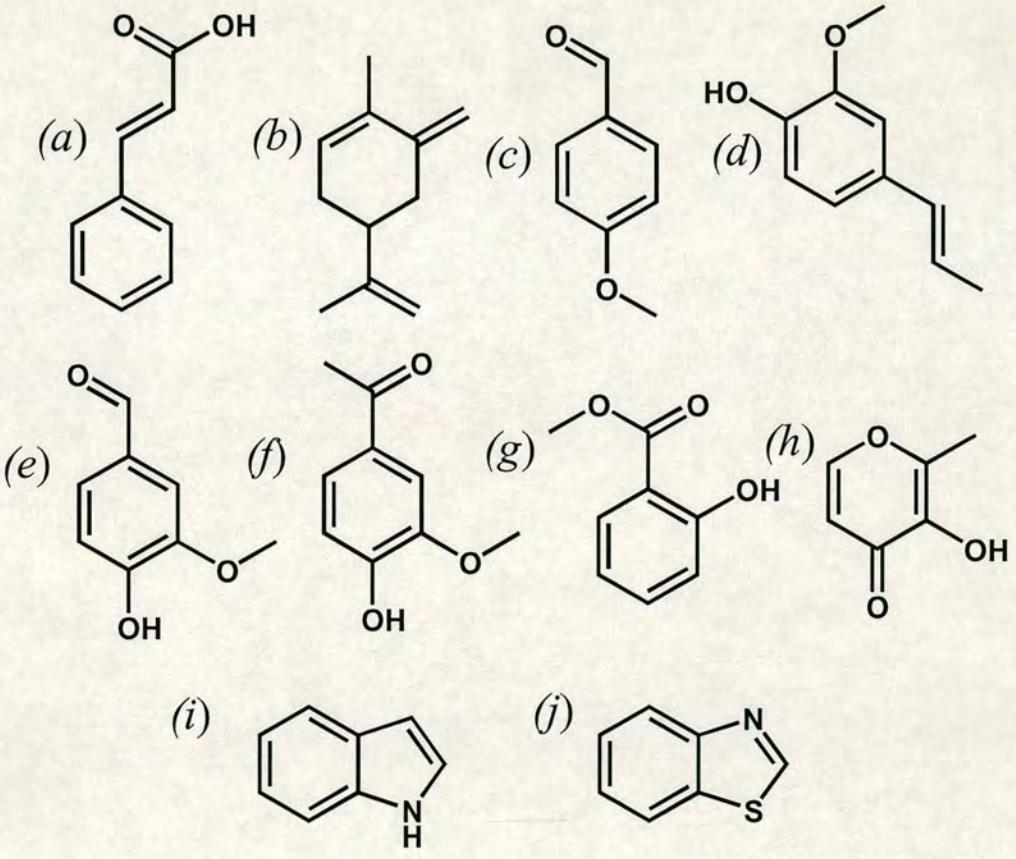

Figure 7. 2: Natural product candidates for GED investigation: (*a*) cinnamic acid, (b) carvone, (c) p-anisaldehyde, (d) isoeugenol, (e) vanillin, (f) acetovanillone, (g) methyl salicylate, (h) maltol, (*i*) indole, (*j*) benzothiazole.

7.2 Centring method

Since the data collected with our new nozzle are basically unfocussed images of the scattered electrons obtained by a conventional nozzle, it is critical for the image to be centred. In other words, it is important that the centre of gravity of the concentric rings is located accurately. Otherwise, with the application of the refinement program, the error originating from the centring method would be spread over the entire data set and would irreversibly affect our capability to determine an accurate structure. Thus a good program giving access to the true centre of the plate is needed. That same program would be able to identify erroneous data and eliminate them prior to structure refinement. The major advantage of such a program would be the ability to use the most valuable data from each photographic plate. Our current standard procedure currently is to discard data wedges, therefore discarding only poor quality pieces of the recorded data but not the entire data sets. This centring method would lead to a better refinement and a more accurate structure.

This program would cut the photographic plates into wedges, as is already the case for the current method of centring. But now, these wedges would be cut by circles as shown in **Figure 7. 3**. The inner part of the plate would not be taken into account, considering it does not have consistent shapes of concentric rings.

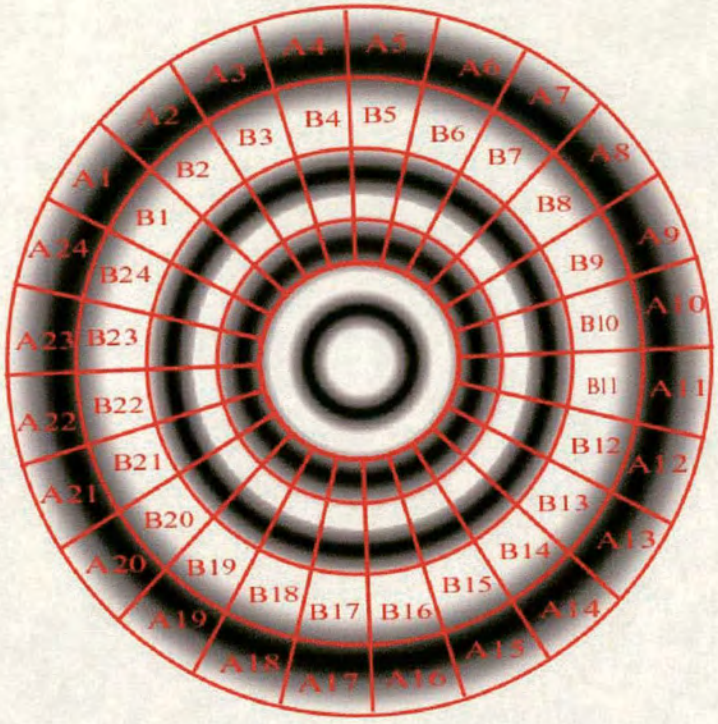

Figure 7. 3: Centring method

The total intensity coming from each of these small areas will be summed up and averaged out:

$$A_{avg} = \frac{1}{n} \sum_{1}^{n} A_n$$

These small areas of intensity will be compared to their respective averages. With an overall analysis of the behaviour of each of these, the centre of the concentric ring would be found. Thus if A_1 is bigger than its average and B_1 is smaller than its average, whilst the opposite B_{13} is bigger and A_{13} is smaller than their respective average, it would mean that the centres of the circles and ultimately the centre of the data are downward to the right. The smaller the wedges of intensities used, the more accurate the resulting centre definition would be. If odd behaviour is noted, for example in the same slice of circle one of the areas behaves contrary to all the others, this would mean that the data inside this area are erroneous and would have to be

rejected. Similar logic could be applied to an entire slice. However if half of the data behaves differently than the other half, not knowing at present how it should behave, the whole plate would have to be discarded. In the future with the help of the deconvolution program, we would be able to discern which half can still be used by comparing the behaviour of the other collected plates to the questionable one.

A major factor needs to be taken into account while performing this centring operation: we have to keep in mind the fact that intensities are sometimes darker on one side of the plate than on the other side. This can be explained by the fact that the main beam, while collecting diffraction patterns, is not going through the centre of the rotating sector. Its shape of s^4 opening, which corrects for the intensity fall, affects the intensities recorded. Thus the program will correct the intensity prior to each operation of re-centring the plate.

7.3 General thoughts on calculations in the solid phase.

This comment is an outside look at this new developing field. For a decade now, there has been a vulgarisation of calculation in the solid phase (or state) as more and more non-experts are able to carry out calculations with the help of commercial packages, the same way as Gaussian was for the gas phase in the mid eighties. Most of the calculations performed still need, as a starting point, one X-ray structure, from which the dimensions of the cell and the symmetry within the crystal can be extracted. No program up to now can give a good approximation of even simple organic molecules in the absence of empirical data. Before Density Functional Theory calculations could be carried out, most of the specialized solid phase calculation groups used the Monte Carlo method to give random starting points for crystal simulations. Because many structures in the solid phase have similar energy levels, their differences in energy are usually small, which carries a challenge to the researchers to predict the correct structures.

The Cambridge Data base is huge, and is only consulted in part at each time. In this database all conditions of crystal growth, for each X-ray structure determination are reported, such as solvent, pressure and temperature. Many crystals of the same compound or complex were grown under various conditions, and are also reported with different space groups and cell dimensions. We could therefore hypothesize that a newly designed code could easily extract trends within families of compounds, monitoring changes and variations as a function of crystallization conditions. Although the code would have no "chemistry knowledge" it might be taught some chemistry later on. Most crystallographers perform from time to time such comparisons. A computing algorithm carrying out these various steps would allow the user to look for trends, more in depth. It is true that in crystals, many variables are to be taken into consideration. This is why only computing code would be able to carry out such trend searches. This code could be used as Monte Carlo is today, as a starting guess geometry for further DFT investigation, giving a starting point for the calculations. Both predictive methods can be parallelized or run sequentially, either interchanging information or comparing their results. Although there are many variables, they are computationally feasible by today's computing standards, and these variations would be faster than any search by pure DFT.

7.4 **References**

1 S. L. Hinchley, M. F. Haddow and D. W. H. Rankin, *Dalton Trans.*, 2004, 384.

2 P. Stenson, Acta Chem. Scand., 1970, **24**, 3729.

3 V. A. Sipachev, *J. Mol. Struct.*, 1985, **121**, 143.

Chapter 8

Bibliography

Bibliography

Jensen F. 1999 Introduction to Computational Chemistry (Wiley: Chichester)

Goodman P. 1981 Fifty years of Electron diffraction (Dordrecht: London)

Hargittai I. and Hagrittai M. 1988 Stereochemical Application of Gas-Phase Electron Diffraction (VCH:Weinheim)

Leach A. 1996 Molecular Modelling: Principle and Applications (Pearson: London)

Appendix A

Courses and Conferences attended

Courses attended

- Unix 1, 2001.
- Unix 2, 2001.
- Fortran, 2001.
- Visual Basic, 2002.
- Applied Computer Science, 2003.
- Applied Numerical Transforms, 2003.
- Finance Basics, 2003.
- Creativity, 2003.
- Intellectual Property in Information Technology, 2004.
- Intellectual Property for Biotechnologist, 2004.
- Patent Searching, 2004.
- Departmental colloquia, 2001-2004.
- University of Edinburgh Inorganic Meetings, 2001-2004.

Conferences attended

University of Scotland Inorganic Conference (USIC),
University of St. Andrews, U.K., September 2001

19th Austin Symposium on Molecular Structures,
Austin, U.S.A, March 2002.
Poster presentation: "New Nozzle Designs: Bringing a Second Youth to Gas Electron Diffraction"

Exploring Modern Computational Chemistry,
University of Nottingham, U.K., August 2002.
Poster presentation: "Why theoreticians Need Experimentalists"

10th European Symposium on Molecular Structure,
St. Petersburg, Russia, July 2003.

Poster presentation: "New Approaches to Low Vapour Pressure Compounds: How Low Can We Go?"

University of Scotland Inorganic Conference,
University of Strathclyde, U.K., September 2003.
Poster presentation: as above.

20th Austin Symposium on Molecular Structures,
Austin, U.S.A, March 2004.
Poster presentation: "Targeting Low Vapour Pressure Compounds"

Appendix B

Publications

Molecular structures of 2,5-dichlorothiophene and 3,4-dichloro-1,2,5-thiadiazole, by the combined analysis of gas-phase electron diffraction data and by *ab initio* calculations, Julien T. Schirlin, Simon F. Bone, Heather E. Roberston, David W. H. Rankin, *manuscript in preparation.*

Molecular structures of 2-chloro- and 2-bromo-thiophene, by the combined analysis of gas-phase electron diffraction data, rotational constants and *ab initio* calculations, Julien T. Schirlin, Simon F. Bone, Heather E. Roberston, David W. H. Rankin, *manuscript in preparation.*

The structure of tris(chloromethyl)amine, Sarah L. Hinchley, Julien T. Schirlin, Heather E. Roberston, Norbert W. Mitzel, David W. H. Rankin, *manuscript in preparation.*

Gas Phase Electron Diffraction Studies of 1-Ethynyl- and 1-Trimethylsilylethynyl-*para*-carboranes. Influence of substituents on the *para*-C_2B_{10} cage skeleton. A. S. Batsanov, A. M. Cameron, M. A. Fox, A. E. Geota, P. J. Low, M. A. J. Paterson, D. W. H. Rankin, H. E. Robertson, J. T. Schirlin, *manuscript in preparation.*

Appendix D

Manual

To use the reservoir, it is imperative to check that the o-rings used in the fittings are checked and that any abnormality observed is fixed. Once the compounds are placed at the bottom of the reservoir, the Ultra-Torr Vacuum fitting must be only finger-tight to the reservoir on the bench. No force should be applied while holding the bulky part of the reservoir, thus avoiding the addition of too much stress on the thin walls of the glass/metal seal. Now the reservoir can be connected to the nozzle to be hand tight, and also the union fitting can be held while tightening the reservoir to the nozzle. The reservoir should be held in place, releasing some stress from the metal/glass seal at the bottom using a ring clamp covered with superwool. The hot air outlet of the reservoir should pass through the middle of the ring. The superwool can now be applied around the reservoir as well as on top with the preset pieces. The heating type can be placed around the Ultra-Torr fitting to ensure no air gap while the thermocouples are in contact with the fitting. The inline heater can be then placed carefully with the help of the flexible bearing inside the reservoir. At this point the shield must be placed and locked in place. The reservoir is evacuated by opening the nozzle valve. The pressure gauge has to be switched off before this, due to the massive volume of air passing into the apparatus that can not be withstood by the diffusion pump alone in such a quick time. If no leaks are observed, then the thermocouple can be introduced into the hot outlet of the reservoir while making sure it can not be blown away. Before switching on the inline heater system, it is imperative to switch on the air compressor, supplying the air flow for the flameless torch. Once a good flow of air flow is obtained out of the reservoir, the heating device can be switched on and the desired temperature can be set up. At the back of the thermometer box there is a knob allowing the user to change the power to the inline heater; for low temperature it is important to reduce the voltage to avoid drastic variations in temperature. The incoming air flow should be regulated. When the experiment is started the entire flow of air should get to the reservoir, so the reservoir will attain the desired temperature within a couple of minutes. Once the experimental temperature is reached the flow of air should be reduced, avoiding abrupt variation in temperature in the reservoir. To cool and monitor the temperature of the reservoir membrane the digital thermometer just needs to be set up to room temperature. Room

temperature will then be attained within 20 minutes, having started at temperature exceeding 170 °C. The maximum temperatures allowed are set by the o-ring used in the Ultra-Torr fitting which has an upper limit of 210 °C.